5-2021

Development and Characterization of Nanofiber-Based Thermoelectric and Piezoelectric Composites

Julio Enrique Trevino
The University of Texas Rio Grande Valley

DEVELOPMENT AND CHARACTERIZATION OF NANOFIBER-BASED THERMOELECTRIC AND PIEZOELECTRIC COMPOSITES

A Thesis

by

JULIO ENRIQUE TREVINO

Submitted to the Graduate College of
The University of Texas Rio Grande Valley
In Partial fulfillment of the requirements for the degree of

MASTER OF SCIENCE

May 2021

Major Subject: Mechanical Engineering

DEVELOPMENT AND CHARACTERIZATION OF NANOFIBER-BASED THERMOELECTRIC AND PIEZOELECTRIC COMPOSITES

A Thesis
by
JULIO ENRIQUE TREVINO

COMMITTEE MEMBERS

Dr. Karen Lozano
Chair of Committee

Dr. Rogelio Benitez
Committee Member

Dr. Arturo Fuentes
Committee Member

Dr. Horacio Vasquez
Committee Member

May 2021

ABSTRACT

Enrique Trevino, Julio, Development and Characterization of Nanofiber-Based Thermoelectric and Piezoelectric Composites. Master of Science (MS), May 2021, 121 pp., 15 tables, 53 figures, 91 references, 91 titles.

This study focuses on the development and characterization of nanofiber-based composites with the goal of developing flexible, lightweight, and cost effective thermoelectric and piezoelectric devices. The following materials were used in the development of the composites: polyvinylidene fluoride (PVDF) with polyaniline (PANI), polypyrrole (PPY), polyindole (PIN), polyanthranilic acid (PANA), polycarbazole (PCZ), polyacrylonitrile (PAN), functionalized multi-walled carbon nanotubes (MWCNT-COOH), and camphorsulfonic acid (CSA). Blends and in-situ polymerization techniques were utilized to increase the desired thermoelectric/piezoelectric response. Nanofiber systems were produced utilizing the Forcespinning® technique. The morphology, structure, electrochemical, thermal stability, thermoelectric, and piezoelectric performance was analyzed. All of the nanofiber PVDF/CP systems displayed higher piezoelectric performance than the pure PVDF nanofiber systems. The PVDF/PPY nanofiber system showed the highest piezoelectric performance of 15.56 V. Thermoelectric devices consisting of 1-17 modules were created, connected electrically in series and thermally in parallel. The maximum voltage output of the 17 modules thermoelectric device was 8.8 mV. The maximum power output obtained from the thermoelectric device was 15 nW with a figure of merit ZT of 0.0002.

DEDICATION

The completion of my graduate studies would not have been possible without the love and support of God and my family. Thanks to God for always being by my side and for believing in me and for guiding me throughout the whole way. My mother, Nereida Trevino, my father, Javier Trevino, my grandmother, Emma Trevino, my brother, Javier Trevino Jr, and my girlfriend Ailani Cantu, inspired, motivated, and supported me throughout the whole journey. There are no words to describe how thankful I am to them and this was possible and became a reality because of each and every single one of them.

ACKNOWLEDGMENTS

I want to thankfully acknowledge the support received by the graduate college for awarding me the Presidential Graduate Research Assistantship (PGRA) to make my graduate experience a reality and success.

I want to thank my advisor Dr. Karen Lozano for her wisdom, constant support, and great mentorship that attributed to my work and myself. Dr. Lozano has filled my graduate research experience with many learning skills that will accompany me and guide me to becoming not only a better mechanical engineer, but person.

I would also like to acknowledge the members of my thesis committee, Dr. Horacio Vasquez, and Dr. Arturo Fuentes. Their guidance, constructive criticism and support assisted me in the main goal of the thesis project and other projects. I would also like to acknowledge the nano-lab administrator, Dr. Victoria Padilla, in which was there every day since day one for any situation that I was in and advice that I needed. I greatly appreciate her guidance, patience, and skills she instilled in me. I would also like to acknowledge Dr. Swati Mohan and Samantha Ramirez in opening and guiding me to the right path to my research experience. It would not have been possible without them.

Lastly, I would also like to acknowledge all the UTRGV Partnership for Research and Education in Materials (PREM) that helped and supported me through my journey for showing me from the basics of how different machinery was utilized to the analysis of data obtained.

TABLE OF CONTENTS

LIST OF TABLES

Page

LIST OF FIGURES

Page

CHAPTER I

INTRODUCTION

Renewable energy is being researched extensively given the limited supply of fossil fuels and their role in greenhouse gas emissions and overall environmental concerns. Renewable energy is produced from sources such as: wind, solar, geothermal, biomass, and hydropower which fully preserve fossil fuels. An attractive source that has been popular in the past two decades is the use of thermal energy transformed into other forms of energy through novel materials and systems that use the phenomena of thermoelectricity. Another attractive source is based on the use of mechanical energy transformed into other useful forms of energy through novel materials and systems that use the phenomena of piezoelectricity and/or triboelectricity.

Like many materials, polyvinylidene fluoride (PVDF) has been widely investigated in many energy-harvesting applications in regard to enhancing its characteristics and processability. Over the past several years, PVDF has been known for it being a polymorphic material and for its exceptional characteristics such as, great flexibility, low-cost, lightweight and biocompatibility for the creation of many energy-harvesting devices.

Traditional inorganic crystalline thermoelectrics such as bismuth telluride (Bi_2Te_3) have been utilized commercially for the last half century, but recent advancements in organic thermoelectrics show potential to use these as alternatives to Bi_2Te_3. PVDF is an attractive system for thermoelectric devices given its flexibility, low-cost and insulating properties.

PVDF's figure-of-merit (ZT) value can be enhanced depending on which process is selected such as making it into fibers, blending polymerization, in-situ polymerization, doping with conductive materials and importantly controlling fiber orientation.

PVDF is highly polymorphic and highly susceptible to be altered upon processing. PVDF can increase the piezoelectric effect by enhancing its beta phase which strongly depends on alignment of its molecules just as it occurs in the making of fine fibers where molecular orientation can be controlled as will be explained in detail in Chapter 2. In recent years, the making of fibers through electrospinning process has been widely explored though this method presents some intrinsic limitations, mostly related to power consumption and fiber yield.

Forcespinning® technology unlike electrospinning, creates fibers through the use of centrifugal forces. The PVDF fibers are stretched mechanically instead of electrically. This creates an increase in yield in orders of magnitude in comparison to electrospinning.

The overview of this research is to enhance the thermoelectric and piezoelectric responses of PVDF forcespun fibers by combining conducting polymers to create multifunctional, flexible, lightweight, and cost-efficient thermoelectric devices and nanogenerators to be used as alternative systems for energy harvesting applications.

CHAPTER II

REVIEW OF LITERATURE

2.1 What is Renewable Energy?

The term “renewable energy” is energy derived from a broad spectrum of resources, all of which are based of self-renewing energy sources such as wind, solar, geothermal, biomass, and hydropower. These resources can be used to produce electricity for all economic sectors such as, nanotechnology, electronics, energy-harvesting, and many other sources of power [1]. Cumulatively, energy consumption has been growing significantly over the years. The consumption of fossil fuels has been identified as a major global environmental threat due to its contribution to global warming. As a result, energy storage has recently attracted the attention of groups of people ranging from researchers to government entities to improve the performance of the energy supply chain.

The energy losses in most systems occur in the form of heat which is usually lost to the environment. Waste heat is an essential resource which if captured and stored, can serve as a useful energy resource for other processes. One major challenge facing most renewable energy resources is that these sources of energy occur intermittently. This can be achieved by storing the excess energy generated when the renewable resources are available and re-use the stored energy when needed or for other processes [2]. Thermoelectric applications are one way to apply this phenomenon and use this energy for many processes.

Another interesting way to harvest energy is by mechanical energy. The energy conversion methods that have been used for transforming mechanical (mostly vibration and kinetic) energy into electrical energy are the piezoelectric, electromagnetic, electrostatic and magnetoelectric composite-based conversion methods [3]. Piezoelectric energy harvesting remains the most widely research harvesting method due to its ease of application, high voltage output without requiring post-processing, high-power density and mature manufacturing methods that can be used for fabricating devices at different geometric scales [3].

Thermoelectric and piezoelectric applications have been increasingly popular in the last decades. Thermoelectric energy harvesting provides a wide range of applications such as micro-cooling, micro-heating, health-monitoring devices, and recovery of wasted thermal energy. Piezoelectric energy harvesting provides a wide range of applications such as power actuators, sensors and portable and wireless devices. Research and current technology demands for human contact, low-cost, ductile, light and flexible materials for more efficient and eco-friendly energy sources.

2.2. What is Thermoelectricity?

Thermoelectricity is the conversion of thermal energy into electrical energy and vice-versa. Thermoelectricity refers to a temperature difference between one side of a material and the other producing electricity, or the reverse; applying an electric current through a material creating a temperature difference between the two sides which can be used to heat or cool systems without combustion or moving parts.

2.2.1 History of Thermoelectricity

The first evidences of thermoelectricity date back to the end of the XVIII century. The Italian physician, physicist, biologist, and philosopher Luigi Aloisio Galvani was conducting experiments at the University of Bologna on the effect of electricity on animals [4]. In the late 1970s, Galvani accidentally observed muscle contractions in a dead frog when its crural nerve was touched by a conductive lancet and sparks were simultaneously emitted from a nearby electric machine [5]. Galvani's research triggered interest in the Italian physicist and chemist Alessandro Giuseppe Antonio Anastasio Volta who was conducting similar experiments at the University of Pavia. Alessandro Volta is known then for discovering, coning the term thermoelectricity, in 1794, after a series of experiments in which he concluded that the electro motive force originated from the temperature difference between the junctions of two dissimilar conducting materials. It was then rediscovered in 1821 when a German physicist by the name of Thomas Johann Seebeck, discovered that an electromotive potential (or electrical voltage) will produce in a circuit of two dissimilar metals when one of the junctions of the circuit was heated or at a higher temperature than the other junction [4]. This phenomenon is called the Seebeck effect.

The understanding of the Seebeck effect, accompanied by the evolving theories on electromagnetism, initiated a new field of research on the conversion between heat and electrical currents. In 1834, the reverse of the Seebeck effect was discovered by a French watchmaker and part-time physicist, Jean Charles Athanase Peltier, whereby heat would be absorbed and liberated at opposite ends in the same circuit of dissimilar metals when current (or a voltage potential) was present. The direction of current in the circuit would determine the direction of heating or cooling [4]. This is called the Peltier effect.

2.2.2 Thermoelectric Governing Effects

Thermoelectric devices are capable of creating voltage when there is a temperature difference at a junction of two materials with dissimilar properties/characteristics known as the power generation mode or Seebeck effect. Thermoelectric devices are also capable of creating a temperature difference between both sides when there is an applied electric current through a material known as the refrigeration mode or Peltier effect. Thermoelectric devices have no moving parts which reduces their vulnerability to mechanical failure. This increases the operation of the thermoelectric devices. This allows for many applications including cooling operations, wearable electronic devices, smart phones, etc. In this study, the power generation mode will be concentrated on.

Thermoelectric devices are composed of two materials as shown in Figure 1 with dissimilar properties/characteristics: one p-type material and one n-type material. P-type materials are doped with electron acceptor atoms, for example Boron (B) which has three valence electrons, in which holes are the majority carriers and electrons are the minority carriers as shown in Figure 2. In a p-type semiconductor, current is largely carried by the holes, which outnumber the free electrons. The whole material remains electrically neutral. N-type materials are doped with electron donor atoms, for example Phosphorus (P) which has five valence electrons, in which the electrons are the majority carriers and holes being the minority carriers as shown in Figure 3. In an n-type semiconductor, current is largely carried by the electrons, which outnumber the holes. The whole material remains electrically neutral.

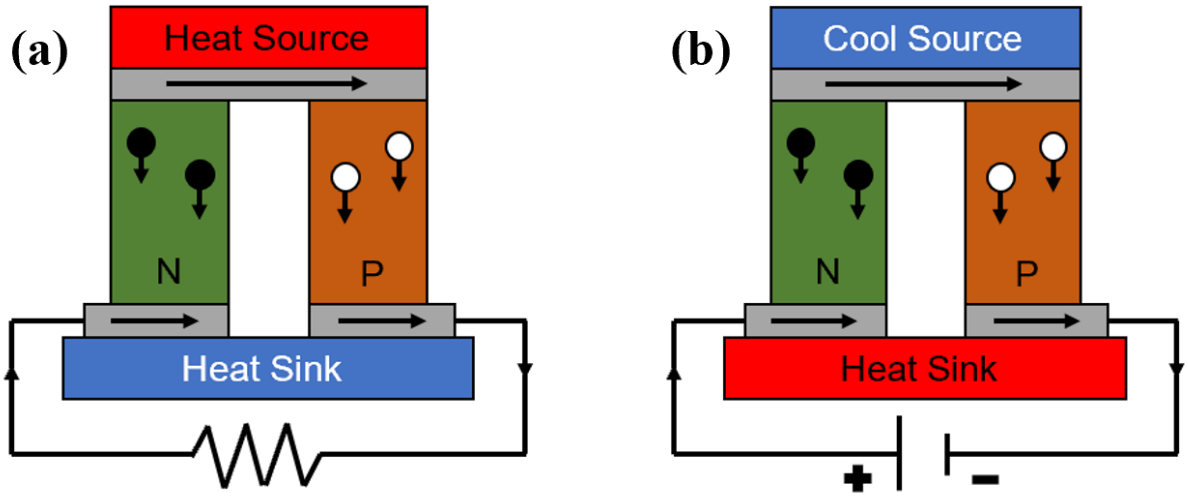

Figure 1: Thermoelectric device: (a) power generation mode (b) refrigeration mode

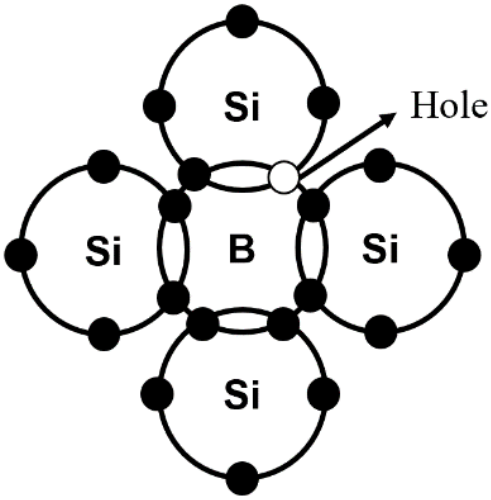

Figure 2: P-type semiconductor

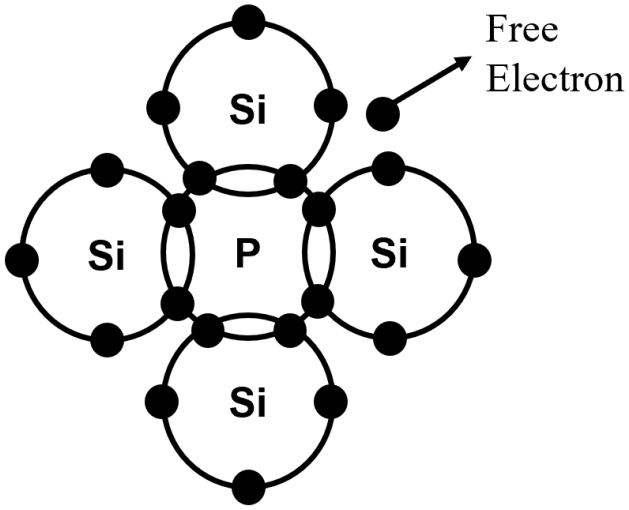

Figure 3: N-type semiconductor

Thermoelectric devices are governed by the Seebeck effect. The Seebeck effect governs the proportionality of the voltage difference to the temperature difference by the Seebeck coefficient. The Seebeck coefficient is a measure of the magnitude of an induced thermoelectric voltage in response to a temperature difference across a material [6]. The relationship between voltage and temperature difference across a thermoelectric device after reaching steady state is

$$V = -\alpha \Delta T \tag{1}$$

where V is the voltage across the junctions of the circuit, α is the Seebeck coefficient and ΔT is the temperature difference across the junctions of the circuit.

The thermoelectric material efficiency of a device is evaluated by a dimensionless figure of merit ZT and given as

$$ZT = \frac{\alpha^2 \sigma}{k} T \tag{2}$$

where α is the Seebeck coefficient, σ is the electrical conductivity, k is the thermal conductivity, and T is the absolute temperature of the thermoelectric device [7]. The higher the ZT figure of merit exhibits a better performance in power generation applications.

By observing equation (2) there are two ways to increase the ZT figure of merit. One way to increase the ZT figure of merit is to increase the power factor [8]. The power factor is

$$PF = \alpha^2\sigma \tag{4}$$

which is the numerator of the ZT figure of merit excluding the temperature difference of the thermoelectric device. However, it is difficult in most thermoelectric materials because the Seebeck coefficient and electrical conductivity are inversely proportional to each other. Increasing either parameter would cause the other to decrease, resulting in minor change to the power factor and ZT figure of merit.

The other way would be to decrease the thermal conductivity of the material [7]. The thermal conductivity of the material is

$$k = k_e + k_l \tag{5}$$

where k_e is the electronic thermal conductivity and k_l is the lattice thermal conductivity. However, the electronic thermal conductivity and electrical conductivity of a material are related via the Wiedemann-Franz Law,

$$k_e = LT\sigma \tag{6}$$

where $L = 2.44 * 10^{-8}\frac{W\Omega}{K^2}$ is the Lorenz number [7]. Increasing one parameter would increase the other parameter as well resulting in minor change to the ZT figure of merit. Therefore, the only parameter left to experiment with is the lattice thermal conductivity which can be reduced by manipulating the phonon scattering of the material achieved through the nanofabrication of thermoelectric materials [9]. The lattice thermal conductivity of a material is due to energy transport by phonons and is often estimated by,

$$k_l = \frac{1}{3}cvl \tag{7}$$

where c, l , and v are the heat capacity, the phonon mean free path, and the sound velocity, respectively [7].

Also, the Seebeck coefficient and electrical conductivity are typically interrelated as a function of carrier concentration. One way to optimize the thermoelectric performance of a material is to find the maximum power factor by varying the carrier concentration [7]. The interrelationship between Seebeck coefficient and carrier concentration of highly conducting semiconductors can be described using a model [13] that explains electron transport in metals

$$\alpha \sim \frac{8\pi^2 {k_B}^2}{3eh^2} m^* T \left(\frac{\pi}{3n}\right)^{\frac{2}{3}} \tag{8}$$

where k_B is the Boltzmann constant, e is the electron charge, h is the Planck constant, m^* is the effective mass of the carrier, and n is the carrier concentration. This model is used to estimate the Seebeck coefficient as a function of carrier concentration. Although a low carrier concentration results to a large Seebeck coefficient, the electrical conductivity will go down. This occurs because the electrical conductivity is proportional to the carrier concentration,

$$\sigma = ne\mu \tag{9}$$

where, μ is the carrier mobility [7]. To obtain a high ZT figure of merit is challenging from the relationship of the Seebeck Coefficient and the electrical conductivity. Increasing one parameter will unfortunately decrease the other and vice-versa.

Table 1. Summary of thermoelectric properties of insulators, semiconductors and metals [32]

Material	Insulators	Semiconductors	Metals
Seebeck Coefficient (α)	$\alpha \approx 1$ mV/K	$\alpha \approx 200$ μV/K	$\alpha \approx 5$ μV/K
Electrical Conductivity (σ)	$\sigma \approx 10^{-10}$ S/m	$\sigma \approx 10^{5}$ S/m	$\sigma \approx 10^{8}$ S/m
Thermal Conductivity (k)	$k \approx 0.1\text{-}1$ $Wm^{-1}K^{-1}$	$k \approx 1\text{-}100$ $Wm^{-1}K^{-1}$	$k \approx 10\text{-}1000$ $Wm^{-1}K^{-1}$
ZT Figure of Merit	$ZT \approx 10^{-14}$	$ZT \approx 0.1\text{-}1.0$	$ZT \approx 10^{-3}$

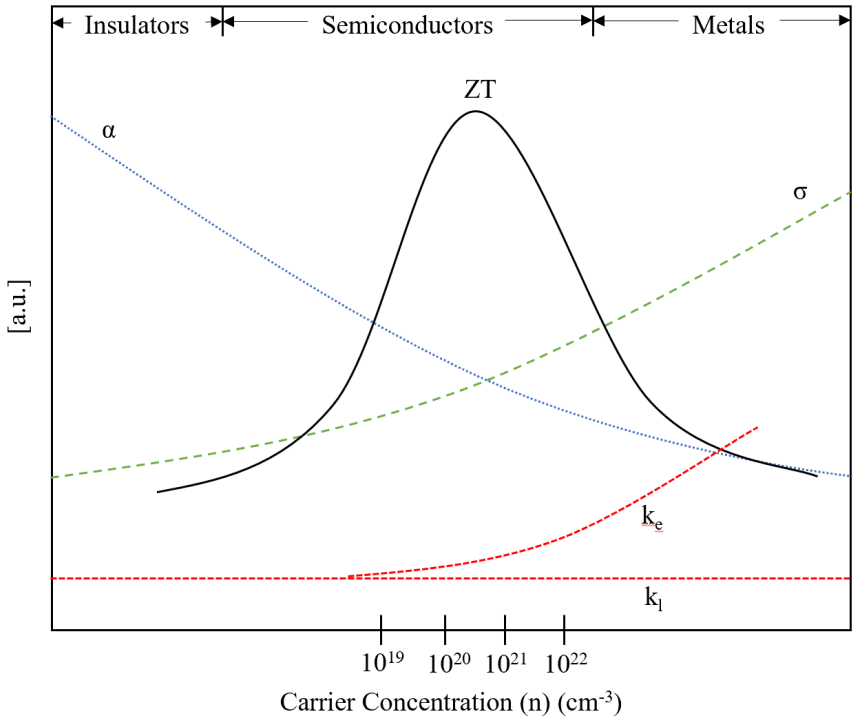

Figure 4: Seebeck coefficient (α), electrical conductivity (σ), and thermal conductivity (k_e and k_l) as a function of carrier concentration (n) [31]

The choice of what type of materials to choose for the creation of thermoelectric devices to maximize thermoelectric performance is based upon the precise identification of the thermoelectric properties of the materials [32]. Insulators have great Seebeck coefficient, but low thermal conductivity which decreases ZT figure of merit. Metals have great electrical conductivity, but high thermal conductivity which decrease ZT figure of merit. Semiconductors are the reason they are researched on to try and determine what combination of materials can maximize the ZT figure of merit by having a balance of Seebeck, coefficient, electrical conductivity and thermal conductivity as shown in Table 1 and Figure 4.

Increasing the *ZT* figure of merit of organic materials will be difficult, but if made a reality, the use of this technology will change the world in many ways by potentially harvesting

tons of wasted energy from heat and creating green energy conversion processes therefore conserving other valuable energy resources.

2.3 Thermoelectric Materials

Thermoelectric materials contain traditional semiconductor-based inorganic and recently developed polymer-based organic materials [6]. Significant progress has been achieved in the thermoelectric industry in recent decades involving inorganic materials. However, these inorganic materials typically are expensive, heavy, brittle and contain toxic elements such as Bismuth (Bi) and Antimony (Sb). Many researchers have turned to organic materials for high-performance thermoelectric materials because organic materials, especially polymers, are normally cheap, low-weight, flexible and non-toxic [10].

2.3.1 Inorganic Materials

There are many inorganic materials used for thermoelectric materials such as Tin Selenide (SnSe), Bismuth Telluride (Bi_2Te_3), Lead Telluride (PbTe) to name a few. Inorganic thermoelectric materials have been used ever since the Apollo missions in the 1950s. Since the mid-1990s, research in the thermoelectric industry has largely focused on enhancing the thermoelectric properties of inorganic materials [11]. Most research was focused on enhancing the Seebeck coefficient and increase scattering of phonons, which leads to reduction of the thermal conductivity. Furthermore, research of inorganic materials have exhibited higher thermoelectric efficiency than those of the organic thermoelectric materials. Although, most of the inorganic thermoelectric materials yield ZT values greater than 1, their applications are limited due to their heavy weight, high cost, processing difficulty, and toxicity [10].

2.3.2 Organic Materials

A major emerging trend is the development of organic flexible thermoelectric materials [11]. This is the cause of the need of wearable and autonomous devices. Personal electronics are common in our daily lives and often rely on batteries. Power is an issue for electronics since they rely on batteries however, batteries have limitations on lifetime and requirement for periodic charging [12]. In comparison to inorganic thermoelectric materials, organic thermoelectric materials contain unique merits such as low cost, light weight, convenient processing, mechanical flexibility, and low thermal conductivity. However, these organic thermoelectric materials are still not practically employed or applied owing to their low thermoelectric efficiency [6]. Great progress has been achieved and some recently developed organic thermoelectric materials have exhibited similar thermoelectric performance to those of traditional inorganic thermoelectric materials. In this regard, organic thermoelectric materials have the potential to bring significant improvement if their thermoelectric efficiency is comparable to, or less than, that of the state-of-the-art inorganic materials [10]. Organic materials used are non-conducting and conducting polymers used to prepare organic thermoelectric materials, but conducting polymers play the dominant role. Poly(3-hexylthiophene) (P3HT), poly(3-octylthiophene) (P3OT), and polyvinylidene fluoride (PVDF) are three commonly used non-conducting polymers. Conducting polymers that are commonly used are polyacetylene (PA), polyaniline (PANI) and polypyrrole (PPY) to name a few [6].

2.4 What is Piezoelectricity?

Piezoelectricity is based on the creation of electrical charges in response to an applied stress on a material. This stress can be in the form of bending, compression, tension, and shearing.

2.4.1 History of Piezoelectricity

Charles Augustin de Coulomb was the first to theorize on the production of electric charge by the mechanical manipulation of solid matter, for example, pressure [14,15]. These ideas by Coulomb motivated René-Just Haüy and Antoine-César Becquerel which led to inconclusive results. In 1817, Haüy observed that certain crystals when compressed showed electrical effects. In 1820, Becquerel also confirmed the same electrical effects [15].

The phenomenon of piezoelectricity was actually discovered by the Curie brothers, Pierre, and Jacques Curie, in 1880 [14]. The Curie brothers showed that crystals of tourmaline, quartz, topaz, cane sugar and Rochelle salt (sodium potassium tartrate tetrahydrate) generated electrical polarization under mechanical stress [16]. It was in 1881 that Hermann Hankel suggested using the term ‘piezoelectricity’ instead of ‘pyroelectricity’ to avoid confusion. In the same year, Gabriel Lippmann, on thermodynamic grounds, suggested that an inverse effect may exist, such that application of charge to opposite crystal surfaces induces deformation. In 1882, the Curie brothers confirmed experimentally that such a reverse effect does occur [15]. The discovery of piezoelectricity led the Curie brothers to build a calibrated generator of electrostatic charges. This device was built using a thin slice of quartz lamella, with both sides metallized, so that the charge generated when a force is applied to the lamella can be collected [17].

In 1893, William Thomson, designated as Lord Kelvin in the later years of his life, made a significant contribution to piezoelectricity by presenting analogy models and laying down some of the basic framework that led to the modern theory of piezoelectricity. Eduard Riecke and Woldemar Voigt greatly contributed to the development of the theory of piezoelectricity with the introduction of the ideas of Lord Kelvin as stated in their work. Finally, in 1894, Voigt developed tensor equations describing the linear behavior of piezoelectric crystals. Voigt was the first to use 'tensor' to describe mechanical stress [15].

During the early years of the 20th century, piezoelectricity continued to be developed theoretically, and it was not until the military demands of World War I that the first important applications were to appear. During the 1914-1918 period, Paul Langevin made use of quartz piezoelectric transducers to detect submarines underwater [15]. He then became the father of sonar and of the discipline of ultrasonics [14]. From 1920 to World War II, single-crystal Rochelle salt was the standard underwater transducer used by the US Navy.

2.5 Piezoelectric Materials

Over the past few decades, the use of wireless sensors and wearable electronics has grown interest exponentially. Electronics have relied on the use of electrochemical batteries for providing electrical energy to devices. The increase in power used by electronics has limited the functionality of the devices. Alternate energy harvesting power sources such as piezoelectric materials have been researched to be able to convert strain energy into usable electric energy. Piezoelectric materials have a wide range of materials, but most importantly they can be divided into piezoelectric ceramics (PZTs) and piezoelectric polymers. The type of piezoelectric material selected has a major influence on the harvester's functionality and performance [18].

2.5.1 Piezoelectric Ceramics

The most common piezoelectric ceramics used are perovskite structure ceramics. Piezoelectric ceramics with a perovskite structure generally exhibit a larger piezoelectric effect compared to other types of materials. In the perovskite structure, highly symmetrically distributed constitutional atoms allow the unit cell to easily deform, and this gives rise to various ferroelectrically-active non-cubic phases. Non-centrosymmetric modifications of the perovskite structure are required for a ceramic perovskite to exhibit piezoelectric behavior. Depending on the modifications, will determine the properties of the material [19]. Piezoelectric ceramics being used are lead zirconate titanate (PZT), sodium niobate ($NaNbO_3$), and silver niobate ($AgNbO_3$). Although, inorganic piezoelectric materials are being utilized in applications, there are some disadvantages that include high temperature processing, polar reorientation, toxicity of lead-containing materials, the need for high cost manufacturing capabilities and most importantly being brittle and prone to fracture [20].

2.5.2 Piezoelectric Polymers

Piezoelectric polymers have had an increasing interest due to the advantages that polymer materials obtain such as being mechanically flexible, lightweight, non-toxic, and less expensive in terms of material cost and manufacturing. The most important factor in why polymers have gotten such interest is the ability to absorb high strain for long periods of time compared to piezoelectric ceramics being brittle and prone to failure. There are many piezoelectric applications such as tactile sensors, energy harvesters, acoustic transducers and inertial sensors. There is a class of polymer materials that have a semi-crystalline structure such as polyvinylidene fluoride (PVDF), polyamides, liquid crystal polymers and Parylene-C [20]. To

get an effective piezoelectric response, a poling process must be done to reorient the molecular dipoles and keep them in the preferred orientation or mechanical stretching depending on the polymer. Although there are many piezoelectric polymers being used, PVDF is the most commonly used and cited piezopolymer due to it having the largest piezoelectric coefficient compared to other bulk polymers [20].

2.6 Structure and Properties of PVDF

Over the past several years, PVDF has garnered attention given the exceptional properties which have shown promising applications to power actuators, sensors, energy harvesters, and portable and wireless devices. The breakthrough came in 1969, when Dr. Heiji Kawai discovered the strong piezoelectric effect in PVDF [21]. PVDF's main focused behavior is its stronger piezoelectric effect than other polymers. PVDF also offers great flexibility, low-cost, lightweight and biocompatibility [22, 23].

2.6.1 Structure of PVDF

PVDF is a semi-crystalline polymer consisting of long chain molecules with the repeat unit CF_2-CH_2. PVDF has a strong electrical dipole moment due to the electronegativity of the fluorine atoms compared to that of the carbon and hydrogen atoms [24]. PVDF consists of about 50% lamellar crystals embedded in an amorphous phase which has supercooled properties liquid properties with a glass-transition temperature (T_g) of about -40°C [21]. In addition to its piezoelectric and chemical structure, PVDF is known for being a polymorphic material, it exists in five distinct crystalline phases: α, β, γ, δ, and ε-phases. The crystalline phases that are

commonly used for practical applications are: α, β, and γ-phases [25]. Depending on the processing of PVDF will determine the crystalline phase obtained or desired.

2.6.2 Properties of PVDF

The α-phase is non-polar due to the packing of molecules, the electrical dipole moments have random orientation and end up cancelling out therefore not contributing to the piezoelectric effect. Even though, the α-phase does not have good piezoelectric properties, it is highly thermodynamically stable compared to the other phases and can be found in commercially available films, polymer solution and melting form. The β and γ-phases are polar and the electrical dipole moments point in the same direction giving PVDF its attractive piezoelectric response [22]. Although both the β and γ-phases exhibit piezoelectric responses, the β-phase shows the highest polarity and as such higher piezoelectric response. To achieve the desired piezoelectric properties in PVDF β-phase, the PVDF α-phase is mechanically elongated or electrically stretched by electrostatic repulsions or electrical poling treatment. To achieve the desired piezoelectric properties in PVDF γ-phase, the PVDF α-phase is heated near the melting point (160°C) or poled under the influence of a high electric field [26]. Other than the piezoelectric properties of PVDF, PVDF has good chemical resistance, weather resistance and thermoelectric properties [27]. PVDF has become an alternative for thermoelectric devices because of its low thermal conductivity which favors a higher ZT value, however they obtain low ZT values due to its low electrical conductivity. To enhance the thermoelectric properties of PVDF, the addition of conductive polymers or fillers in PVDF can promote its electrical conductivity thus increasing the ZT value but, will also increase the thermal conductivity of PVDF which affects the ZT value. The main challenge to improve the ZT value in PVDF is to

simultaneously enhance its electrical conductivity and Seebeck coefficient while suppressing its thermal conductivity [28].

2.7 Structure and Properties of Conducting Polymers

Conducting polymers (CPs) have proved their potential in the field of supercapacitors, sensors, transistors, etc. for the past decades and can bring major breakthroughs in the field of thermoelectric devices [29]. The discovery of the conducting polymers started in the 1970s. A new class of polymers possessing high electrical conductivity by three collaborating scientists, Alan J. Heeger, Alan G. MacDiarmid and Hideki Shirakawa was found, and they received the Nobel Prize in Chemistry 2000 [30]. They found the conductivity of polyacetylene, after doping with electron withdrawing arsenic pentafluoride (AsF_5), increased electrical conductivity to an order of 10^3 S/cm. Soon after, a series of conducting polymers were reported, including polypyrrole (PPY), polyaniline (PANI), and polythiophene (PTH) from the end of the 1970s to the beginning of the 1980s [33]. Conducting polymers changed the way polymers were seen in the field of electrochemical research which led to numerous applications.

2.7.1 Structure of Conducting Polymers

Polymers are carbon-based compounds consisted of repeating units or monomers. Conjugated polymers consist of a large number of repeating units or monomers. Conjugated polymers are amorphous in nature due to its spaghetti-like structure consisted of many polymer chains [32]. Conjugated polymers become conducting polymers after doping. The unique characteristic of conducting polymers is the conjugated molecular structure of the polymer main chain where the π-electrons delocalize over the whole polymer chain [33]. Conducting polymers

constitute a special class of organic materials whose ability to conduct electrical charge originates from the π-conjugation [32].

2.7.2 Properties of Conducting Polymers

Electrical conductivity is the most important property of conducting polymers. In conducting polymers, the charge carriers are located in the local doping energy levels (limited length or conjugated polymer chain) or in a very narrow doping energy band in the case of ordered domains. The charge carriers can move easily on the conjugated polymer main chain, but the charges have to hop for the transportation between the conjugated polymer chains. Therefore, the conductivity of conducting polymers shows characteristics of hopping transportation [33]. The conductivity of common doped conducting polymers is in the range of 10^{-3}-10^{3} S/cm, whereas that of conjugated polymers without doping is in the range of 10^{-9}-10^{-6} S/cm. The highest conductivity reported in literature for conducting polymers is 10^{5} S/cm for drawing-extended ordering conducting polyacetylene film [33]. Other than its electrical conductivity, conducting polymers also exhibit important properties such as electrochemical, magnetic, wetting, mechanical and optoelectronic properties for applications in batteries, electrode materials, and polymer light-emitting diodes (PLEDs).

2.8 Processing of Thermoelectric/Piezoelectric Nanomaterials

There are several processes to create organic thermoelectric and piezoelectric materials which include films and fibers. The properties of the materials will be determined and can change depending on the processing and materials used for the application desired.

2.8.1 Films of Thermoelectric/Piezoelectric Nanomaterials

Films have been globally investigated in thermoelectric and piezoelectric applications due to their chemical stability and high piezoelectric properties. Films are not only being investigated in thermoelectric and piezoelectric areas, but in areas of research such as aerospace, medical, optical and biological areas due to its ability to combine electrical and mechanical properties, it being biocompatible, lightweight, low cost and have reasonable strength. There are various methods to create films that include spin coating, drop casting and etc. Kim et al [34] created poly(3,4-ethylenedioxythiophene):polystyrene sulfonate (PEDOT:PSS) films by two methods. The first method to create the films was by filtering PEDOT:PSS solution through a 5.0 μm nylon syringe filter , spin-coated twice at 1500 rpm for 60 s onto glass, and thermally annealed on a hot plate at 150 °C for 5 min in air resulting in a thickness of 190 nm. The second method to create the films was by preparing PEDOT:PSS films with a thickness of a few to several tens of micrometers, 50, 100 and 200 μL PEDOT:PSS solutions were drop-casted onto glass and annealed on a hot plate at 80 °C for 30 min in air. Lee et al [35] created PVDF-TrFE films by dissolving PVDF-TrFE granules in butanone-2 with a weight fraction of 70 mg/mL. The thickness of the films made from drop casting was ~ 30 μm. The films were then poled at fields of approximately 30 MV/m at 105 °C for 60 min.

2.8.2 Fibers

Compared to films, nanofiber systems have proven to overcome the brittleness of thin films. Electrospinning, also known as electrostatic spinning, is a process capable of producing polymer fibers with nanoscale diameter and has been widely used to develop nanofiber systems. Forcespinning® nanofibers are known for small diameters, long length to diameter ratio, large

surface area to volume ratio, and small pore size. High solvent uptake, versatility of design and superior mechanical performance are just some of the other characteristics that nanofiber systems provide, which make these systems attractive candidates for a wide array of applications such as composites, protective clothing, catalysis, electronics, biomedicine, filtration and agriculture [36].

2.8.2.1 Comparison Between Electrospinning and Forcespinning®

In electrospinning, a typical set-up consists of a high voltage power supply, a programmable syringe pump, syringe, needle, and a grounded collector screen. During the process, a polymer solution is injected from a small nozzle under the influence of a voltage as high as 30 kV. The buildup of electrostatic charges on the surface of a liquid droplet induces the formation of a jet. The jet is subsequently stretched to form a continuous fiber. The solvent evaporates before it reaches the collecting screen, and solid fibers are collected on a conducting surface, and form nonwoven mats [36]. Electrospinning has been most popular when it comes to creating fibers, but electrospinning has limitations due for its inefficient mass production rate and having to have an electric field.

Forcespinning® (FS) technology developed at UTRGV is used to overcome the low production rate observed in the electrospinning process. Lozano et al [37] created this alternative FS method which draws fibers through the use of centrifugal forces which allows for a significant increase in yield and ease of production. It is also capable to create nanofibers without the need of an electrical field which eliminates the restrictions of low dielectric constant materials. FS has the distinct advantage of being able to produce nanofibers of both polymeric solutions and melts. The fiber production rate at the lab scale is over 1 g/min which is

significantly higher than any electrospinning apparatus where systems operate typically at about 0.1 g/h [38]. FS shows an output of 600 times higher than electrospinning. The FS process begins by first loading the solution/melt into a special spinneret, and when producing nanofibers, the polymer solution is drawn from the orifice by rotating forces. The fibers will then be collected onto the collector and with a special fashion be collected from the collector. Important parameters that must be considered when the polymer is being drawn include humidity, spinneret angular velocity, orifice radius, viscoelasticity, surface tension, evaporation rate, temperature, and distance of spinneret orifice to collector. In the case of polymer solutions, it is important to determine the polymer-solvent compatibility to determine the optimum concentrations that will allow the production of nanofibers. In the case of melts, it is important to determine the optimum temperature that will provide a viscosity that will allow the melt to flow and produce nanofibers. To produce a polymer jet, the rotating forces must be high enough to overcome the surface tension of the solution or melt. If the forces exerted on the polymer jet are too high, the surface tension of the polymer solution is capable of causing the polymer jet to break up and produce beads. This can occur where the angular velocity of the spinneret is low and/or the viscosity is low. If the viscosity is high, the forces being used to draw the fiber may not be strong enough to create a polymer jet but, if the viscosity is low, the polymer jet may break up and produce beads instead of fibers. The viscoelasticity of the polymer gives rise to extrudate swelling among other phenomena, this increases the diameter of the polymer jet as it is pulled through the orifice. As the polymer jet is expelled from the orifice and toward the collector, the fiber experiences rapid solvent evaporation. If the fiber experiences a high rate of evaporation, the fiber will experience large diameter size due to the disturbance of the polymer jet. If the evaporation rate of the solvent is low, then the fibers may be converted into a thin film as the layers build up on the

collector. The diameter of the orifice also has an effect on nanofiber production which decreases fiber diameter size if the orifice diameter size is decreased as well and vice-versa. For the distance of collector, it depends how long it takes for the solvent to evaporate, the distance required to allow the fiber to begin to spiral outwards, and the type of collection method used. If the distance of the collector is short, the fiber will not be allowed to stretch, and a larger diameter will be obtained. Many parameters affect the performance and production of the nanofibers but, optimizing these parameters will result in a large-scale production in comparison to electrospinning.

2.9 Performance of Thermoelectric Materials/Devices

2.9.1 Films

Carroll *et al* (2012) [45] demonstrates individual composite films of multi-walled carbon nanotubes (MWCNT)/PVDF that are layered into multiple modules that resemble a felt fabric. Carroll *et al* (2011) [46] reported previously the fabrication of the single films comprised in the multilayered fabric. To form the multilayered film, individually prepared conducting and insulating layers are arranged as shown in Figure 5 and then bonded together by compressing the multilayer fabric at the melting point of the polymer in use. The films used in this study were PVDF with 95 or 20% carbon nanotubes (CNTs) by weight (wt %) for the conducting layers, and pure PVDF for the insulating layers. The resulting single film thicknesses were 25 – 40 μm, while the multilayer film thickness depends on the total number of layers. The Seebeck coefficients of the p-type and n-type films were 10.05 μVK^{-1} and -5.04 μVK^{-1}, respectively. A 72-layer fabric was used to obtain a seebeck coefficient of 550 μVK^{-1}. The electrical

conductivity of the p-type and n-type films were 500 S/m and 800 S/m, respectively. The maximum power generation on the 72-layer fabric obtained was 137 nW when the load resistance matched the internal fabric resistance of 1270 Ω. For a fabric composed of 300 layers, the theoretical power output could be as high as 5 μW. With optimization of the single film and layer count for a specific application, this device can offer an alternative to thermoelectrics for use in lightweight, flexible, and portable electronics.

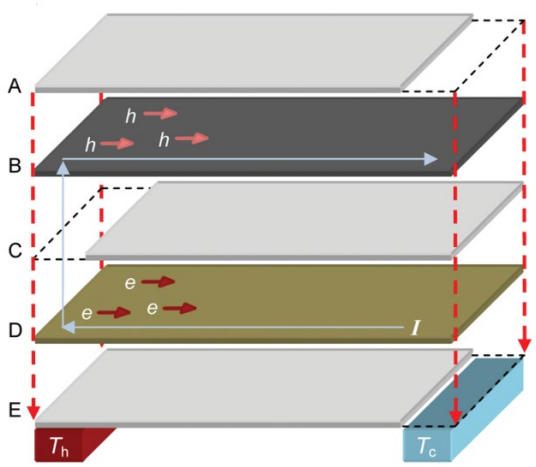

Figure 5: Layer arrangement for the multilayered fabric. PVDF/CNT conduction layer (B,D) are alternated between PVDF insulation layers (A,C,E) [45]

Yu et al (2015) [47] reported a promising method of simultaneously improving both properties of PANI composites filled by CNTs. An m-cresol solution containing 1 wt % PANI emeraldine base (PANIeb) was prepared with 0.5 g of PANIeb and 34 mL of m-cresol by using a pen-type sonicator. Another solution of 1.4 wt % PANI doped with camphorsulfonic acid (PANI-CSA) was prepared by mixing 0.5 g of PANIeb and 0.64 g of CSA in 35 mL of m-cresol with the sonicator for 30 min. CNT solutions were prepared by sonicating 20 mg S/DWCNTs or DWCNTs in 34 mL of m-cresol for 30 min. Subsequently, these solutions were homogenized by an additional 20 h sonication in a bath-type sonicator. The CNT solutions were mixed with the

PANIeb or PANI-CSA solutions with different rations to have 18 different variations of the solid contents in the composites for this study. The mixture was homogenized in the ultrasonic bath for an additional 20 h. The solution was dropped on glass substrates and dried at 40 °C on a hot plate until the solution was fully dried in an ambient condition. The film thickness was measured to be 3.5 – 19 μm with 1 mL of the solution on a 2 x 2 cm^2 glass substrate, depending on the solid contents in the solution. The dried films were then annealed at 100 °C for 2 h in a vacuum for densification. S/DWCNTs – only and DWCNT – only samples were also prepared by drop-casting solutions containing S/DWCNTs (0.1 wt %) and sodium dodecylbenzenesulfonate (SDBS) (0.5 wt %) in 1 – 1.5 mL of m-cresol. Prior to the drop casting process, the solution was homogenized by using the bath-type sonicator for 24 h. The obtained film was dried at 40 – 50 °C on a hot pate in an ambient condition until the solution was fully dried (typically for ~ 20 h). The dried films were then annealed at 100 °C for 2 h in vacuum to improve the electrical conductivity. The film thickness was measured to be ~ 1 μm with 1 mL of the solution on 2 x 2 cm^2 glass substrates. PANI-CSA composites experienced better electrical conductivity and Seebeck coefficients than PANIeb composites. The electrical conductivity of the PANI-CSA composites containing 30 wt % DWCNTs was measured to be ~ 610 S/cm with a Seebeck coefficient of ~ 61 μV/K at room temperature, resulting in more than 2 orders of magnitude higher power factor, ~ 220 $\mu W/(mK^2)$ compared to ~ 1.8 $\mu W/(mK^2)$ of PANI-CSA. The upper and lower bound thermal conductivity of the PANI-CSA composites containing 30 wt % DWCNTs was estimated to be 15 W/(mK) and 0.7 W/(mK). Therefore, the estimated highest value of ZT from the samples was ~ 0.1 at room temperature. This study identified a promising method of achieving high-performance fully organic thermoelectric composites with unique characteristics such as flexibility and low density.

Grunlan *et al* (2016) [48] created outstanding low temperature thermoelectric power factor from completely organic thin films comprised of PANI, graphene, and DWCNTs using a layer-by-layer (LBL) assembly technique. Aqueous suspensions of 0.1 wt% graphene and 0.03 wt% DWCNTs were individually prepared with DI water containing 2 wt% PEDOT:PSS. Both graphene and DWCNT suspensions were bath sonicated for 30 min, followed by 20 min of 15 W tip sonication to homogenize. The dispersed solutions were centrifuged at 4000 rpm for 20 min and the supernatant was decanted. A cationic PANI solution was prepared by dissolving 0.1 g of PANI in 30 g of N,N-dimethyl acetamide (DMAC) under continuous stirring overnight, followed by bath sonication for 2 h. For PANI/graphene-PEDOT:PSS and PANI/DWCNT-PEDOT:PSS multilayer films, the substrate was dipped into the aqueous solutions, alternating PANI and graphene (or DWCNT), with each cycle generating one bilayer (BL). The first dip into each solution was for 5 min, followed by rinsing in three DI water baths for 20 s each. After assembling the first BL, subsequent dips were for 1 min each. For the PANI/graphene-PEDOT:PSS/PANI/DWCNT-PEDOT:PSS quadlayer (QL) films, the substrate was alternately dipped into the PANI solution for 5 min, rinsed with DI water, and followed by an identical dipping and rinsing procedure as in the graphene solution. The substrate was then submerged in PANI and DWCNT solutions for 1 min with DI water rinsing steps in between, which results in one deposition sequence of a PANI/graphene-PEDOT:PSS/PANI/DWCNT-PEDOT:PSS QL. After this initial QL was deposited, the same procedure was followed with 1 min immersion steps until the desired number of QLs was deposited. PANI/graphene-PEDOT:PSS/PANI/DWCNT-PEDOT:PSS exhibits the highest electrical conductivity of 1885 S/cm at 80 QLs. The 80 QL film exhibited a Seebeck coefficient of 120 μV/K which resulted in the highest power factor value of 2710 $\mu W/mK^2$ ever reported for an organic material. Although

thermal conductivity could not be measured, ZT of the films is expected to fall between 0.03 and 2 which would give the highest ZT ever reported for fully organic materials.

2.9.2 Fibers

Chen *et al* (2012) [49] prepared PANI/CNT thermoelectric composite nanofibers by a combination of in situ polymerization and electro-spinning process. The PANI/CNT composite powder was synthesized by the in-situ polymerization of aniline with ammonium peroxydisulfate (APS) as the oxidant in the presence of multi-wall carbon nanotubes (MWCNTs). The aniline monomer and MWCNTs was mixed and then added into 1 M hydrochloric acid (HCl) to form the aniline/MWCNTs/HCl suspension. The APS/HCl solution was slowly dropped into the well-stirred aniline/MWCNT/HCl mixture. The polymerization was carried out at 0 °C by stirring for 6 h in an ice bath. The products were filtered and washed with DI water three times and then by ethanol three times. Then they were dried under vacuum. The obtained powder was put into 50 mL 0.1 M ammonia solution and was stirred for 24 h at room temperature. Next, the suspended solution was filtered and washed again with DI waster and ethanol three times each and then dried under vacuum. The obtained powders were the composites containing CNT and PANIeb. The PANI was further doped by mixing the obtained PANI/CNT powder with CSA at a mole ration of 1:0.5. Three types of nanofibers were fabricated by electrospinning using pure PANI, PANI/CNT and (Directly Mixed PANI/CNT) DM-PANI/CNT as the raw materials. Chloroform was used as the solvent and polyethylene oxide (PEO) was used as the spinning-aid agent. The mixed suspension was stirred for 5 h and then supplied for spinning. The electro-spinning was carried out under the conditions of a cathode voltage of 8 kV and mandrel collector rotating rate of 1000 rpm. The electrical conductivity and Seebeck coefficient of the PANI/CNT composite

fibers have been measured in the parallel and perpendicular directions to the fiber axis. For both the DM-PANI/CNT and PANI/CNT nanofiber nanocomposites, both of their electrical conductivity and Seebeck coefficient increase with increasing CNT content. When the CNT content is 40 wt %, the electrical conductivity and Seebeck coefficient obtained for the PANI/CNT was 17.1 S/cm and 10 μV/K, respectively. The power factor obtained was 0.18 x 10^{-6} W/(mK^2). When the CNT content is 40 wt %, the electrical conductivity and Seebeck coefficient obtained for the DM-PANI/CNT was 7.5 S/cm and 12 μV/K, respectively. The power factor obtained was 0.12 x 10^{-6} W/(mK^2). Although the thermoelectric properties of the obtained polymer are far away from inorganic thermoelectric materials, their low density, low cost, easy synthesis, facile processing, and the possibility of improving the thermoelectric properties of this family of materials, encourages high expectations for applications and research on organic polymer thermoelectric materials.

Pan *et al* (2020) [50] reported one-dimensional high-performance PEDOT:PSS thermoelectric fibers, which were continuously produced through a modified wet-spinning approach followed by post-treatment with concentrated sulfuric acid (H_2SO_4). The PEDOT:PSS dispersion with 5% dimethyl sulfoxide (DMSO) was concentrated under magnetic stirring at 60 °C for 1 h. Then, the PEDOT:PSS fibers were prepared at room temperature using a custom-made wet-spinning setup. 200 μL of the spinning formulation was loaded into a 5 mL syringe. The formulation was extruded through a microneedle into an isopropanol (IPA) coagulation bath, which was fixed on a rotation stage. The diameters of the microneedles were 16, 20, 23, 25, 27 and 30 G. The flow rate of the spinning formulation was maintained at 3 μLh^{-1} by a syringe pump. After extrusion, the as-spun fibers were collected at the bottom of the coagulation bath, and then immersed in H_2SO_4 for post-treatment. After treatment, the fibers were rinsed in a

washing bath consisting of ethanol/DI water for three times. Finally, the fibers were dried in air at room temperature while being hung vertically with a weight of 40 mg. When the H_2SO_4 concentration increases from 0 to 98%, the electrical conductivity increases from 501 to 4029.5 S/cm, and the Seebeck coefficient slightly decreases from 21.7 to 19.2 μV/K. The optimal power factor obtained was 147.8 $\mu W/mK^2$ for the PEDOT:PSS fiber treated with concentrated H_2SO_4 for 10 min. This power factor is the highest value reported for organic thermoelectric fibers. The room-temperature thermal conductivity of our PEDOT:PSS fibers is estimated to be in the range of 0.5-1 W/(mK) corresponding to a ZT of 0.05-0.09. The PEDOT:PSS thermoelectric fibers developed in this work hold a great promise for applications in advanced wearable energy harvesting systems.

Cho *et al* (2018) [51] prepared PEDOT:PSS/CNT composite fibers with the CNT content ranging from 10 to 50 wt% by a wet-spinning process using a common solvent/coagulation system for applications in organic fiber-based thermoelectric generators. PEDOT:PSS pellets, CNTs distilled water, and DI water were mixed using a ball mill at 25 Hz for 60 min. The total concentration of the pastes was 8 wt%. Thermoelectric composite fibers with the CNT content ranging from 10 to 50 wt% were prepared via direct spinning of the pastes. About 2.4 mL of the prepared paste was extruded into a coagulation solvent of methanol at a flow rate of 4 mL/min from a syringe with a tip of inner diameter of 2.1 mm. The thermoelectric PEDOT:PSS/CNT composite fibers collected at the bottom of the coagulation bath were dried at room temperature for 7 h. The as-spun fibers were immersed in a mixture of aqueous hydrazine solution and ethanol for 10 min. Then, the fibers were dried on a hot plate at 180 °C for 20 min. For the polyethyleneimine (PEI) infiltration, the 10 wt% hydrazine-treated fiber with a length of 2 cm was immersed in a 10 mL of a PEI/ethanol solution until the whole ethanol was evaporated on a

hot plate of 70 °C for 1 h. It was found that hydrazine treatment could be a suitable strategy to increase thermoelectric properties. As the hydrazine concentration was increased from 0.01 wt% to 1 wt%, the Seebeck coefficient increased from ~22 μV/K to ~42 μV/K. Interestingly, with the 10 wt % hydrazine solution treatment, the PEDOT:PSS/CNT composite fibers exhibited a n-type Seebeck coefficient of ~29.3 μV/K. As the hydrazine concentration was increased 0.01 wt% to 1 wt%, the electrical conductivity decreased from ~1400 S/cm to ~290 S/cm. As a result, the optimized p-type and n-type power factors of ~83.2 μW/(mK^2) and ~35.6 μW/(mK^2), respectively, were obtained at a hydrazine concentration of 0.1 wt%. The amine-rich PEI is a well-known n-type dopant of SWCNTs. For further n-type doping of the CNTs, a PEI/ethanol solution was infiltrated into the 10 wt% hydrazine-treated PEDOT:PSS/CNT composite fibers. After 0.01 wt% PEI infiltration, the Seebeck coefficient, electrical conductivity, and power factor of the composite fibers increased to ~47 μV/K, ~540 S/cm and ~113 μW/(mK^2). As the PEI concentration was increased to 0.1 and 1 wt%, the Seebeck coefficient, electrical conductivity and power factor of the composite fibers did not further increase. The electronic thermal conductivities of the thermoelectric fibers of the optimized p- and n- type were calculated using the Wiedemann-Franz relationship obtaining 0.71 and 0.39 W/(mK).

Table 2. Performance of thermoelectric literature					
Material	Process	Seebeck Coefficient (μV/K)	Electrical Conductivity (S/cm)	Thermal Conductivity (W/(mK))	Ref
PVDF/MWCNTs	Film	10.05 (p) -5.04 (n) 550 (72 L)	5 (p-type) 8 (n-type)	-	[45]
PANI-CSA/CNTs	Film	61	610	0.7 - 15	[47]
PANI/graphene-PEDOT:PSS/PANI/DWCNT-PEDOT:PSS	Film	120 (80 QL)	1885 (80 QL)	-	[48]
PANI/CNT / DM-PANI/CNT	Fiber	10 / 12	17.1 / 7.5	-	[49]
PEDOT:PSS	Fiber	19.2	4029.5	0.5-1	[50]
PEDOT:PSS/CNT	Fiber	29 (p-type) -47 (n-type)	970 (p-type) 540 (n-type)	$k_e \approx 0.71$ (p) $k_e \approx 0.39$ (n)	[51]

Table 3. Performance of thermoelectric literature (continued)				
Material	Process	Power Factor ($\mu W/(mK^2)$)	Figure of Merit ZT	Ref
PVDF/MWCNTs	Film	-	-	[45]
PANIeb/CNTs & PANI-CSA/CNTs	Film	220	0.1	[47]
PANI/graphene-PEDOT:PSS/PANI/DWCNT-PEDOT:PSS	Film	2710 (80 QL)	0.03-2	[48]
PANI/CNT & DM-PANI/CNT	Fiber	0.18×10^{-6} / 0.12×10^{-6}	-	[49]
PEDOT:PSS	Fiber	147.8	0.05-0.09	[50]
PEDOT:PSS/CNT	Fiber	83.2 (p-type) 113 (n-type)	-	[51]

2.10 Performance of Piezoelectric Materials/Devices

2.10.1 Films

Sharma *et al* (2011) [39] produced a thin PVDF-TrFE (polyvinyledenedifluoride-trifluoroethylene) semi-crystalline, copolymer film using standard lithography process for cost-

effectivity, film uniformity, and high resolution of polymer patterning for pressure sensing in catheter applications. PVDF-TrFE was spin-coated into thin films, 1 μm thick, at 2000 rpm for 30s. The PVDF-TrFE film was cured in vacuum oven at 130 °C for 5 h for strong adhesion and near β-phase formation due to the residual stress between the thin film and the substrate. The PVDF-TrFE based pressure sensor obtained a 0.8-1.0 V peak-to-peak voltage while finger tapping. The PVDF-TrFE based pressure sensor can operate over a range of 0-300 mmHg, with a fast recovery time of 0.17 s, acceptable in catheter applications.

Wang *et al* (2014) [40] successfully demonstrated a novel integrable nanogenerator design based on sponge-like mesoporous piezoelectric PVDF thin films. PVDF powder was dissolved in N,N-dimethylformamide (DMF) solvent at 65 °C and then mixed with Zinc Oxide (ZnO) nanoparticles (NPs). The mixture was treated in an ultrasonic bath for 30 min and yielded a uniformly mixed PVDF/ZnO nanoparticle suspension. The suspension was cast into a film shape in a petri dish and dried in atmosphere at 75 °C. The films were then immersed in a 37 wt% HCl solution for 3 h to completely remove the ZnO nanoparticle template. After acid etching, the films were washed by deionized (DI) water and mesoporous PVDF thin films were obtained. This type of nanogenerator can generate considerable electrical energy by harvesting mechanical energy from surface oscillations. An oscillator was located 6 cm away from the nanogenerator and generated surface oscillations with a controlled frequency of 40 Hz. The peak-to-peak voltage and peak-to-peak current output of the nanogenerator was 11.1 V and 9.7 μA, respectively. It provides a promising solution for developing practical self-powered personal electronic devices.

Maiti *et al* (2020) [41] prepared a nanohybrid of PVDF and lead zirconia titanate (PZT) through solution route. Initially PVDF was mixed with DMF in a beaker and was stirred at 60 °C until it gets dissolved completely. Meanwhile, PZT was mixed with DMF in a different beaker and

was stirred at 60 °C followed by ultrasonication. The sonicated PZT dispersion and viscous PVDF solution were mixed and kept for stirring at 60 °C till the solution becomes homogenous. Then the solution was transferred to a petri dish and kept overnight at 60 °C for drying. This dried film is compressed in a compression molding machine to get a homogenous film of the hybrid material. The nanohybrids were prepared using different concentrations of PZT in 0, 10, 20, 30, 40 wt%. The device shows high electrical output due to presence of PZT and maximum output is generated using 30 wt% of PZT. The peak-to-peak voltages were measured with different human movements such as finger tapping, feet tapping and bending. The device produces a peak-to-peak voltage of 55 V and output power density of 36 $\mu W/cm^{-2}$ by finger tapping which is high in comparison to other reported values and can be used to operate some low power consumption electronic devices.

2.10.2 Fibers

Compared to films, electrospinning and FS are processes that create PVDF nanofiber mats while simultaneously changing the α-phase to β-phase of PVDF. Abolhasani *et al* (2016) [42] prepared graphene reinforced PVDF composite nanofibers and their morphology, crystallinity, polymorphism and electrical outputs were investigated for the first time. PVDF and DMF solutions containing different graphene contents (0%, 0.1%, 1%, 3% and 5% weight (wt)) were sonicated for 20 min followed by stirring at 60 °C overnight. The electrospinning conditions were adjusted at spinning voltage, working distance, and feeding rate of 20 kV, 17 cm, and 1ml/h, respectively. Formation of the α-phase and β-phase was shown by FTIR analysis and addition of 0.1 wt% graphene increased the amount of β-phase from 77% to 83%. However, for the 5 wt% graphene decreased the amount of β-phase from 77% to 75%. The electrical voltage output was highest with 0.1 wt% at a value of 7.9 Volts when impacted by 0.2 MPa

pressure and frequency of 1 Hz. It was the first time that the role of graphene reinforced PVDF composite nanofibers was used to increase the electrical output. This investigation shows the potential application of graphene reinforced PVDF composite nanofibers for portable self-powering electronic devices.

Bai *et al* (2020) [43] investigated the production of Bismuth Chloride/PVDF ($BiCl_3$/PVDF) nanofibers-based nanogenerators. $BiCl_3$ was used because it promotes the β-phase of PVDF and increases the electrical conductivity. First, DMF and acetone solvents (volume ratio 6:4) were prepared by mechanical stirring doped with $BiCl_3$. After $BiCl_3$ completely dissolved, PVDF powder was dissolved in the mixtures at 60 °C for 3 h to obtain PVDF solutions. The doping content of $BiCl_3$ is 1, 2, 4, 7 and 10 wt%, respectively. The $BiCl_3$/PVDF nanofibers were prepared by electrospinning. The solution flow rates, the applied voltage and the distance between the needle and the receiver was 0.2 ml/h, 18 kV and 15 cm, respectively. The high β-phase content was achieved from the nanofibers of PVDF doped with $BiCl_3$, which enhanced the piezoelectric power output of the nanofibers. An output voltage of 1.1 V was created under vertical vibration of a vibrating table with a frequency of 5 Hz and an amplitude of 3 mm. The maximum peak current and power surface density are 2 μA and 0.2 μWcm^{-2}, respectively. When the $BiCl_3$/PVDF nanofiber composite was impacted by a 14 g falling ball from a 9 cm height, the output voltage was 38 V. If the impact strength was further enhanced, the piezoelectric output would be higher. This investigation shows that $BiCl_3$/PVDF nanofiber composite based piezoelectric nanogenerators are a promising mechanical energy harvester for portable electronic and wearable devices.

Wang *et al* (2020) [44] produced flexible high-performance nanogenerators that can convert mechanical energy into electrical energy for the development of self-powered wearable

electronic devices. PVDF (12%) solution to electrospin was prepared by mixing 1.2 g of PVDF in 7 mL of DMF using a magnetic stir on a hot plate for 6 h at a temperature of 70 °C. After, 3 mL of acetone was added into the mixture and was stirred for 4 h at room temperature and was named solution A. In addition, Iron (III) Chloride ($FeCl_3$) was added into another solution with the same previous steps and the mixture was left stirring for 12 h to fabricate the PPy coated nanofiber films (NFMs). To electrospray the cesium lead bromide ($CsPbBr_3$)@PVDF beads, a precursor solution had to be prepared by dissolving 0.0076 g of Lead (II) bromide ($PbBr_2$), 0.0044 g of cesium bromide (CsBr) and 0.6 g of PVDF pellets in the solvents of 5 mL DMF and 5 mL acetone under continuous stirring. To create the 3D multilayer NFMs, there was a sequence in which what order the components went in as follows: (1) 5 mL of solution B, (2) 2 mL of solution C, (3) 10 mL of solution A, (4) 2 mL of solution C and (5) 5 mL of solution B. Solutions A and B in which were electrospun had solution flow rates, the applied voltage and the distance between the needle and the receiver 1.2 ml/h, 13 kV and 15 cm, respectively. The parameters are the same for the electrospraying except for the needle size in which changed from 23-gauge to 20-gauge. When this process was all done, the prepared samples were put in a sealed chamber containing 10 μL of pyrrole monomer and kept for 30 min in a hot oven at 60 °C. The PPy electrodes were fabricated using vapor phase polymerization of Py monomer on the surface of the electrospun PVDF nanofibers with $FeCl_3$ being the oxidant. 3D multilayer NFMs were achieved. A new multilayer assembly was developed for piezoelectric generators that contains PVDF NFMs, PPy/PVDF NFMs based electrodes and a topographic structure of ($CsPbBr_3$)@PVDF beads. The maximum values of the piezoelectric output voltage and current density, with the applied stress of impact being 6 kPa with a constant frequency of 5 Hz, of the multilayer assembly were 10.3 V and 1.29 $\mu A/cm^2$, respectively. It could even detect a weak

pressure as low as 7.4 Pa. These high values of output voltage and current density may be for the integration of the $CsPbBr_3$)@PVDF beads into the NFMs. $CsPbBr_3$)@PVDF beads possess high fractions of β-phase content which help the piezoelectric response. The assembly in creating 3D NFMs may open up the possibility of fabricating high-output piezoelectric nanogenerators.

Table 4. Performance of piezoelectric literature

Material	Process	Testing	Results (V)	Reference
PVDF-TrFE	Film	Finger Tapping	0.8 – 1.0	[39]
PVDF/ZnO	Film	Oscillations with a frequency of 40 Hz	11.1	[40]
PVDF/PZT Nanohybrid	Film	Finger Tapping	55	[41]
PVDF/Graphene	Fiber	Impact Pressure of (0.2 MPa,1 Hz)	7.9	[42]
PVDF/$BiCl_3$	Fiber	Vibration Table (5 Hz, 3 mm) /14 g Falling Ball	1.1 / 38	[43]
PVDF NFMs, PVDF/PPy NFMs/($CsPbBr_3$)@PVDF	Multi-Layer Fiber System	Impact Pressure of (6 kPa, 5 Hz)	10.3	[44]

CHAPTER III

STATE OF THE ART EQUIPMENT

3.1 Forcespinning® (FS)

Fibers or nanofibers have typically been created with an experimental technique called electrospinning but, has a limitation for its inefficient mass production rate and having the need to use an electric field.

Forcespinning® (FS) is a recently developed technology produced to overcome low production rate observed in the electrospinning process. Lozano *et al* [37] created a new process, FS, in which draws fibers through the use of centrifugal forces which allows for a significant increase in yield and ease of production. It is also capable to create nanofibers without the need of an electrical field. The FS process begins by first loading the solution/melt into a special spinneret, and when producing nanofibers, the polymer solution is drawn from the orifice by centrifugal forces. The fibers will then be collected onto the collector and with a special fashion be collected from the collector to obtain an aligned fiber mat.

Important parameters that must be considered when the polymer is being drawn include humidity, spinneret angular velocity, orifice radius, viscoelasticity, surface tension, evaporation rate, temperature, and distance of spinneret orifice to collector. Many parameters affect the performance and production of the nanofibers but, optimizing these parameters will result in a large-scale production of nanofibers.

3.2 Characterization

There are various methods or processes to characterize a material. When characterizing a material, it refers to the analysis of the material's structure and properties. The characterization of a material's structure can be internally, for example the phase identification of the material, or externally, for example the surface topography of the material. There are different properties that a material can have or obtain such as, thermoelectric, electrical, thermal, and piezoelectric to name a few. The different characterization techniques that will be presented in this project include scanning electron microscope (SEM), x-ray powder diffraction (XRD), differential scanning calorimetry (DSC), thermogravimetric analysis (TGA), thermoelectric, electrical, thermal, electrochemical, and piezoelectric testing.

3.2.1 Scanning Electron Microscope (SEM)

The idea of the SEM goes back to the last century at which a first electron microscope was constructed by two physics scientists Ruska and Knoll in 1933. The most recent advanced technologies of the SEM is the process of generating images digitally followed by viewing them on a computer and the majority of are equipped with an energy-dispersive spectrometer (EDS) system for analysis. The EDS has advantages of evaluating the composition of various elements in the sample.

The SEM consists of many components to function properly. It consists of electron gun, electron beam, anode, magnetic lens, backscattered electron detector, secondary electron detector and stage. SEMs use electrons that are reflected or knocked off the sample to create an image. First, the entire SEM needs to be under vacuum. Vacuum is needed to protect the equipment from contamination, vibration and noise [55]. It also allows for a high-resolution image.

Electrons are generated at the top of the column by the electron beam. The electrons are accelerated and attracted by the positively-charge anode. In a similar fashion to optical microscopes, electromagnetic lenses are used to control the path of the electrons. They are electromagnetic instead of glass since electrons cannot pass through glass. The electromagnetic lenses are consisted of metal rods wrapped around coils and when current is passed through these coils, a magnetic field is generated controlling the path of the electrons. Two electromagnetic lenses used are the condenser lens and an objective lens. In many SEMs, apertures are combined with the electromagnetic lenses to control the size of the electron beam [55].

Two types of electrons used for imaging are backscattered (BSE) and secondary electrons (SE). BSEs are reflected back after elastic interactions between the electron beam and the sample. In comparison, SEs originate from the atoms of the sample and inelastic interactions between the electron beam and the sample. Also, to perform elemental analysis on the sample, the detection of the energies of x-rays from the sample are detected to identify the different elements the sample contains [55].

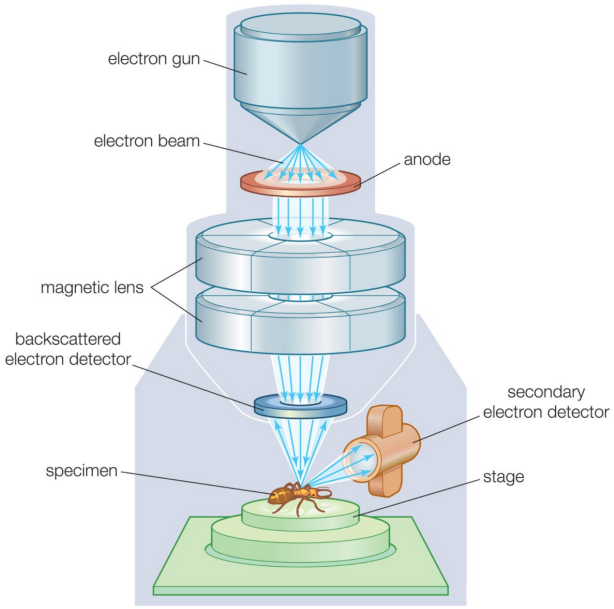

Figure 6. Scanning electron microscope (SEM) schematic [53]

3.2.2 X-Ray Diffraction (XRD)

Ever since 1912, research on XRD by crystals initiated by Laue, Friedrich, and Knipping opened new possibilities to crystalline materials and the development of powerful tools in the fields of materials science engineering [56]. The XRD method is based on the ability of crystals to diffract x-rays allowing a precise study of the structure of crystalline phases.

X-ray diffractometers consist of three basic elements: an x-ray tube, a sample holder, and an x-ray detector as shown in Figure 7. X-rays are generated in a cathode ray tube by heating a filament to produce electrons. The electrons will be accelerated toward the target material being studied by an applied voltage. When the electrons have sufficient energy to move the inner shell electrons of the target material, characteristic x-ray spectra is produced. These x-rays are directed onto the sample and the intensity of the reflected x-rays is recorded. When the geometry of the incident x-rays onto the sample satisfy the Bragg Equation, constructive interference occurs and a peak in intensity occurs [57]. The general relationship between the wavelength of the incident x-rays, angle of incident and spacing between the crystal lattice planes of atoms is known as Bragg's Law,

$$n\lambda = 2dsin\theta \tag{10}$$

where n is the order of reflection, λ is the wavelength of the incident x-rays, d is the interplanar spacing of the crystal and θ is the angle of incidence as shown in Figure 8. The x-ray detector records and processes this x-ray signal and converts the signal to a count rate which is shown on a computer monitor.

Characterization using XRD is widely used for the identification of unknown crystalline materials. Strengths for using the tool include it being a powerful and rapid technique for the

identification of unknown materials, minimal sample preparation is required, XRD machines are widely available and data interpretation is relatively straight forward.

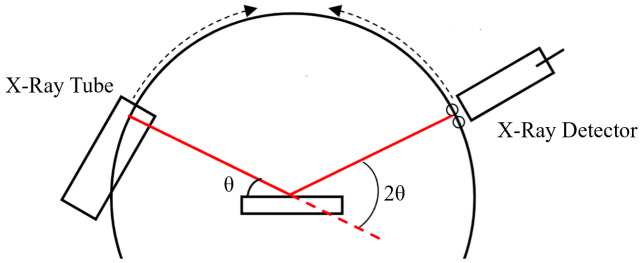

Figure 7. X-ray diffraction (XRD) schematic

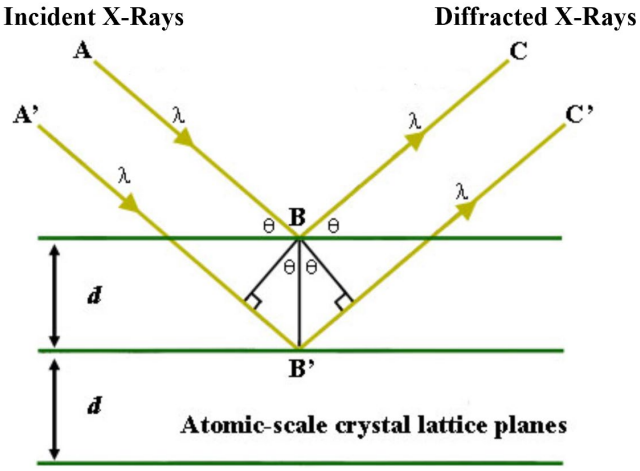

Figure 8. Bragg's Law schematic [58]

3.2.3 Fourier-Transform Infrared Spectroscopy (FTIR)

Fourier-Transform Infrared Spectroscopy (FTIR) is an analytical technique used to identify organic, polymeric, and, in some cases, inorganic materials. The FTIR analysis method uses infrared light to scan test samples and observe chemical properties. Different changes in the characteristic pattern of absorption bands clearly indicates a change in the composition of the material or the presence of contamination. FTIR analysis is utilized for identifying and

characterizing unknown materials such as films, solids, powders, or liquids. It is also utilized for identifying contamination on or in a material such as particles, fibers, powders, or liquids. It is also utilized for identify additives after extraction from a polymer matrix and identifying oxidation, decomposition, or uncured monomers in failure analysis investigations. [79]

The FTIR instrumentation system as shown in Figure 9 sends infrared radiation of about 10,000 to 100 cm^{-1} through a sample. This infrared radiation can either be absorbed or transmitted through depending on the sample being tested. The absorbed radiation is converted is converted into rotational and/or vibrational energy by the sample's molecules. The resulting signal at the detector presents as a spectrum, typically from 4000 cm^{-1} to 400 cm^{-1}. This represents the molecular fingerprint of the sample. Each molecule or chemical structure will produce a unique spectral fingerprint, making FTIR analysis a great tool for chemical identification and especially for phase intensities if the sample is capable of obtaining different phases which depends on the development of the sample. [79]

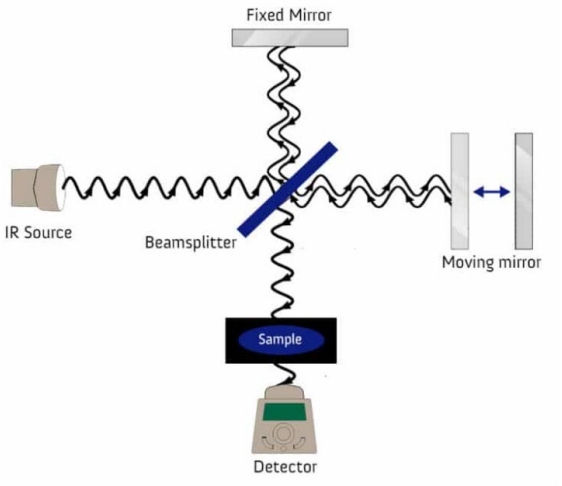

Figure 9. Fourier-transform infrared spectroscopy (FTIR) schematic [80]

3.2.4 Thermogravimetric Analysis (TGA)

Thermogravimetric analysis (TGA) is an essential tool use for material characterization. TGA is a technique in which the mass of a sample or material is measured as a function of temperature or time. The sample or material is subjected to a controlled temperature program in a controlled atmosphere. TGA is applicable in most industries consisted of environmental, food science, pharmaceutical and especially used in the research and development of various substances and engineering materials, solid or liquid, to obtain knowledge about the thermal stability and composition.

A TGA consists of a sample pan that is supported by a precision balance. The pan sits in a furnace and is heated and cooled during the experiment. The sample is put into the pan to measure its thermal degradation. Not only is the thermal degradation measured but, the TGA can quantify the loss of water, loss of solvent, loss of plasticizer, decarboxylation, pyrolysis, oxidation, decomposition, weight percent (%) of filler, and weight % of the sample. The mass of the sample is monitored during the experiment as a function of temperature or time. An inert or reactive gas controls the sample environment and exits through an exhaust. For example, in Figure 10, it shows the decomposition of calcium oxalate monohydrate, CaC_2O_4. The decomposition of CaC_2O_4 occurs in three mass-loss steps with the release of water (12.3%), carbon monoxide (19.2%), and carbon dioxide (30.1%) as shown from the black line [59]. The derivative of the black line or TGA curve (DTG) provides the decomposition rate and is helpful for evaluating the mass-loss steps accurately [59].

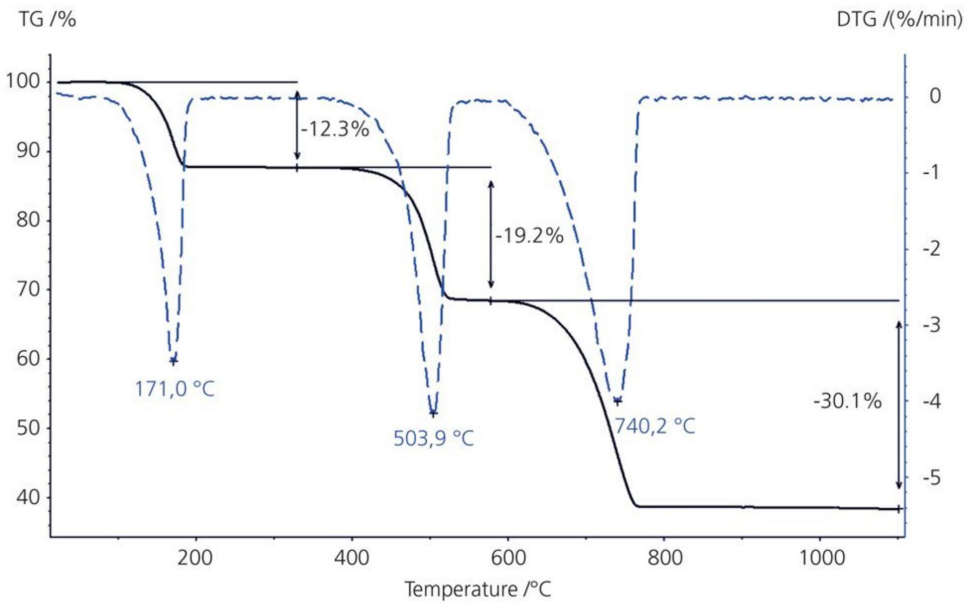

Figure 10. TGA example showing weight loss (%) vs. temperature (°C) [59]

3.2.5 Differential Scanning Calorimetry (DSC)

Differential scanning calorimetry (DSC) means the measurement of the change of the difference in the heat flow rate to the sample and to a reference sample while they are subjected to a controlled temperature program [60]. DSC can be used to investigate a variety of materials such as compact solids such as plastics, rubbers, organic materials, ceramics, glass, composites, metals, powders, fibers, textiles, pastes, gels and even liquids.

There are two types of DSC units: Heat Flux and Power Compensation. A heat flux DSC unit was used to characterize various materials as shown in Figure 11. A heat flux DSC unit is comprised of a heater, heat sink, heat resistor, thermocouples, amplifiers, temperature control program, sample, and reference holders. The heater applies heat to the reference and sample through the heat sink and heat resistor. The heat flow is proportional to the heat difference of the heat sink and holders. In case endothermic or exothermic phenomena occurs to the sample such as transition or reaction, the heat sink has enough heat capacity to compensate the phenomena.

This leads to the temperature difference between the sample and reference kept constant [61]. DSC enables the measurements of characteristic temperatures, melting, crystallization, thermal stability, thermal curing, heat history, specific heat capacity, and purity analysis [61]. Figure 12 shows an example of a DSC graph in which shows various parameters that can be obtained from the data. Endothermic reactions, energy absorbed, and exothermic reactions, energy released, are shown as peaks on the figure. If the peaks are shown as upright peaks, they are exothermic reactions such as crystallization or curing, but if they are upside down peaks, they are endothermic reactions such as melting or transitions. If a shift of the baseline (dashed line) occurs, it represents the T_g of the material. Typically, when operating the DSC unit, two cycles of heating and cooling are done. The two cycles are necessary to remove residual solvents and erase the

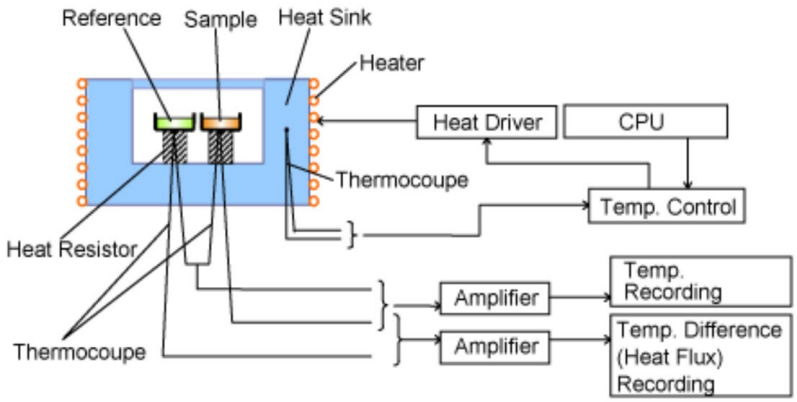

Figure 11. Differential scanning calorimetry (DSC) block diagram [61]

thermal history of the material on the first cycle. The second cycle is to observe the material's true characteristic temperatures and structure. Lastly, if the temperature goes too high on the temperature control program shown on the figure, the material can experience oxidation or decomposition depending on the material and temperature being used.

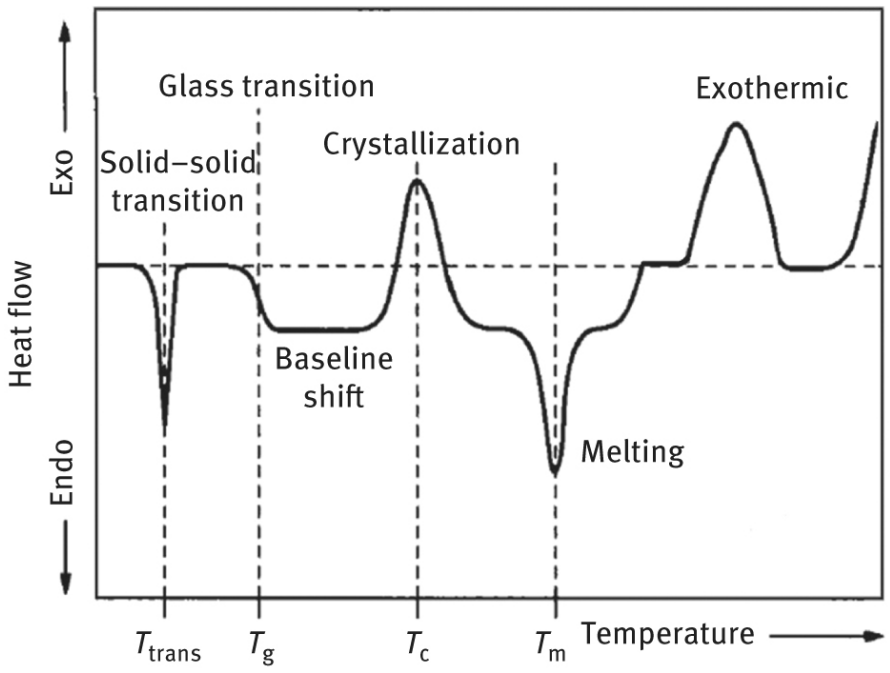

Figure 12. DSC example showing heat flow vs. temperature [62]

3.2.6 Electrochemical Characterization

Electrochemical characterization studies the electrochemical behavior of materials under certain electrochemical conditions [63]. An electrochemical analyzer is used to characterize the electrochemical properties of materials by, for example cyclic voltammetry (CV) and electrochemical impedance spectroscopy (EIS). This powerful technique is used for energy storage applications to understand the reaction mechanisms involved in charge transfer, mass transport, electrolyte transport, electron transport, etc. [63].

An electrochemical analyzer contains an electrochemical cell that consists of electrodes, whether it be a two-electrode system, three-electrode system, or four-electrode system [63]. A three-electrode system was used to characterize various materials. The electrochemical cell contains three basic electrodes, the working electrode, counter electrode, and the reference electrode. The working electrode typically works as a cathode and the counter electrode as the

anode or vice versa along with an electrolyte. The electrochemical cell can also have a reference electrode in which exhibits a depolarized behavior to restrict the change in its potential of current passing through it. The electrochemical cell provides the path of flow of current throughout the circuit when connected to and external source. The electrolyte provides the path for the flow of electrons or ions inside of the electrochemical cell. The chemical reactions inside of the electrochemical cell convert chemical energy to electrical energy. The voltage of the material is measured between the reference and the working electrode. The current flows through the counter and the working electrodes [63].

3.2.6.1 Cyclic Voltammetry (CV)

In voltammetry, a potential varying with respect with time, is applied to the electrochemical cell and current is measured as a function of that potential. Specifically, in cyclic voltammetry, the current is recorded by alternating the current from positive to negative and negative to positive between the chosen limits as shown in Figure 13. Cyclic voltammetry gives information about the reduction and oxidation peaks of the material, predicting the capacitive behavior of the electrode and the potential at which the material oxidizes and reduces [63].

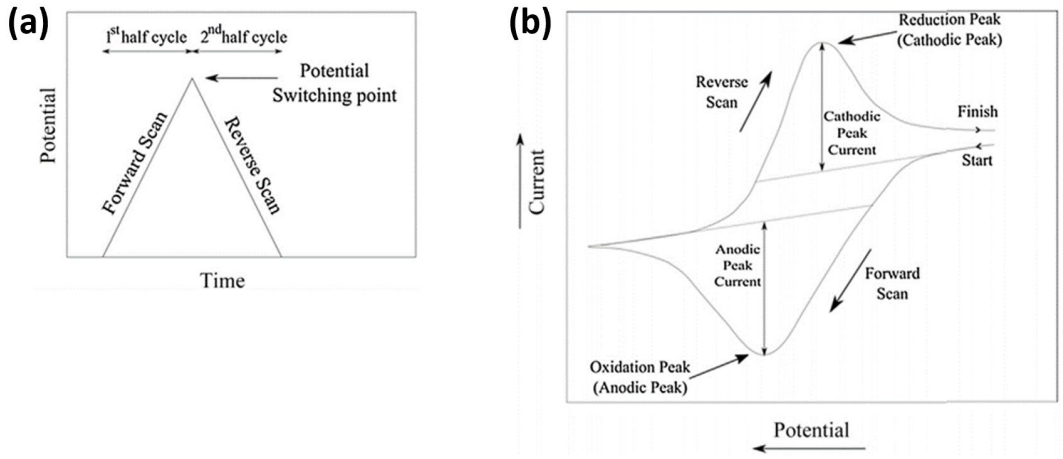

Figure 13. Cyclic voltammetry example (a) input (b) output [63]

3.2.6.2 Electrochemical Impedance Spectroscopy (EIS)

EIS is utilized to find the impedance of the electrochemical cell. A sinusoidal alternating current (AC) voltage is applied to the working electrode which results in generating the current whose amplitude and phase angle are measured with respect to the applied AC voltage [63]. The impedance is a function of frequency resulting in an impedance spectrum. The data obtained can be compared to a modified Randles circuit and the impedance spectra can be evaluated as shown in Figure 14. This can help describe the electrode processes when both kinetics and diffusion are important while also showing an estimation of the charge transfer resistance the material has being studied [63].

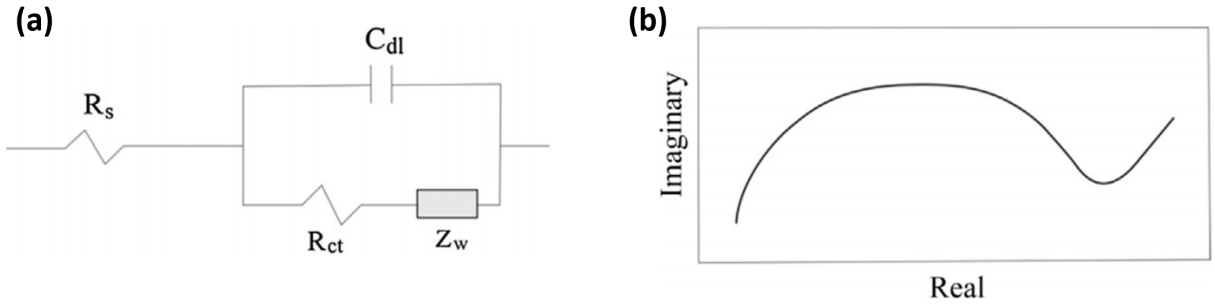

Figure 14. Example of EIS (a) modified randles circuit (b) impedance plot [63]

3.3 Testing Apparatus

3.3.1 Thermoelectric Seebeck Coefficient Testing

The thermoelectric Seebeck coefficient is the most crucial and important parameter to calculate the thermoelectric properties of materials. The thermoelectric Seebeck coefficient describes the measure of an induced thermoelectric voltage by a temperature difference from one junction to the other as shown in Figure 15a.

To be able to find the Seebeck coefficient, the Peltier method as shown in Figure 15b is utilized as in Alvarez *et al* (2018) [77]. Two electrodes of any kind of material are heated and cooled by Peltier cells to generate a temperature difference as shown in Figure 15c. The applied temperature difference will cause the majority carriers to diffuse from the hot to the cool surface creating a voltage difference.

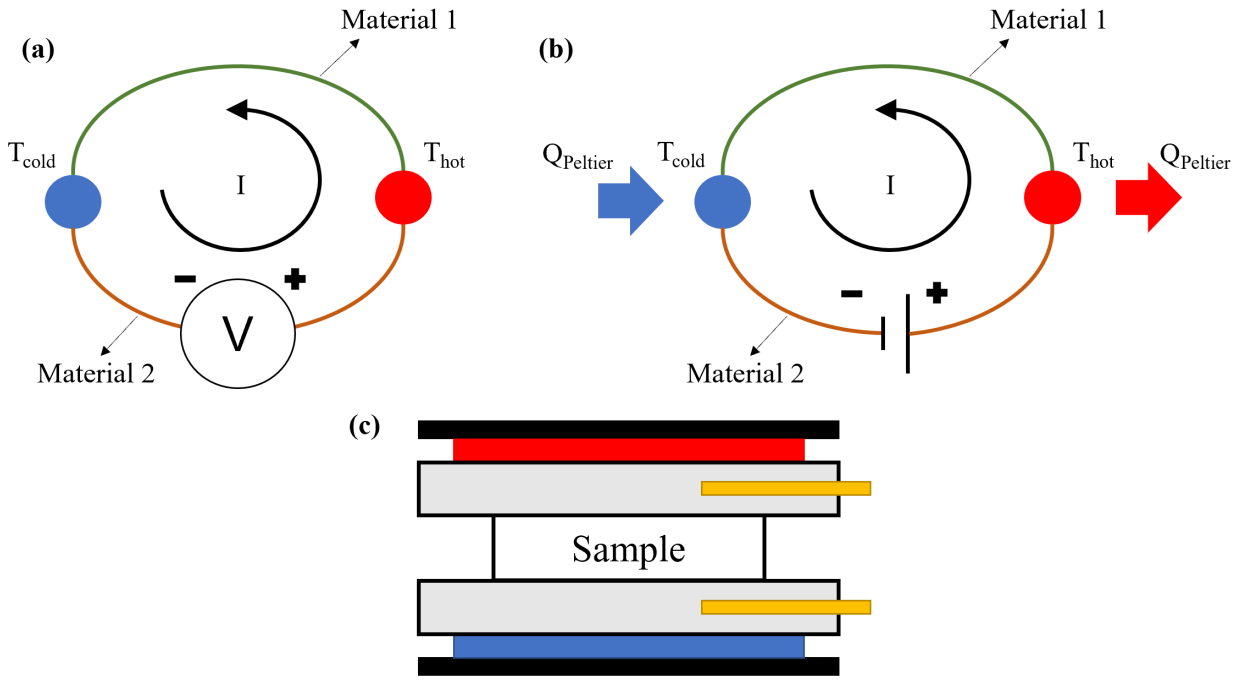

Figure 15. Thermoelectric effect (a) seebeck (b) peltier (c) peltier model

To be able to measure the volage difference across the material, a micrometer or multimeter has to be utilized. To be able to measure the temperature difference, temperature sensors or thermocouples have to be attached to the model. Afterward, the temperature difference and voltage difference can be utilized to find the Seebeck coefficient as shown in the relationship in Equation 1.

3.3.2 Electrical Conductivity Testing

The electrical conductivity in thermoelectrics is essential to calculate the thermoelectric properties of materials. Electrical conductivity describes the electron current produced when a force applied pushes the electrons [64]. Usually, the electrical conductivity is found by measuring the electrical resistivity, ρ, which is the inverse of electrical conductivity as shown below in Equation 10.

$$\sigma = \frac{1}{\rho} \tag{10}$$

where σ is the electrical conductivity and ρ is the electrical resistivity.

A four-point probe can be utilized to measure the sheet resistance of any material mostly semiconductors by pressing the material in between electrodes. A four-point probe functions by passing current through the outer two probes and measuring the induced voltage through the inner two probes [65]. This allows the measurement of the material's surface resistance by using Ohm's law as shown in Equation 11,

$$V = IR \tag{11}$$

where, V is the voltage, I is the current and R is the resistance [64,65]. With the surface resistance obtained from the four-point probe, the electrical resistivity can be calculated using the proportionality of resistance to length over area as shown in Equation 12,

$$R = \rho \frac{L}{A} \tag{12}$$

where, L is the distance between two electrodes specifically the two inner electrodes, and A is the cross-sectional area of the material specifically width and thickness of the material. Rearranging Equations 10 and 12, Equation 13 shows the calculation to determine the electrical

conductivity of the materials in the through plane [66]. An example of how the four-point probe functions is shown in Figure 16a.

$$\sigma = \frac{L}{RA} \tag{13}$$

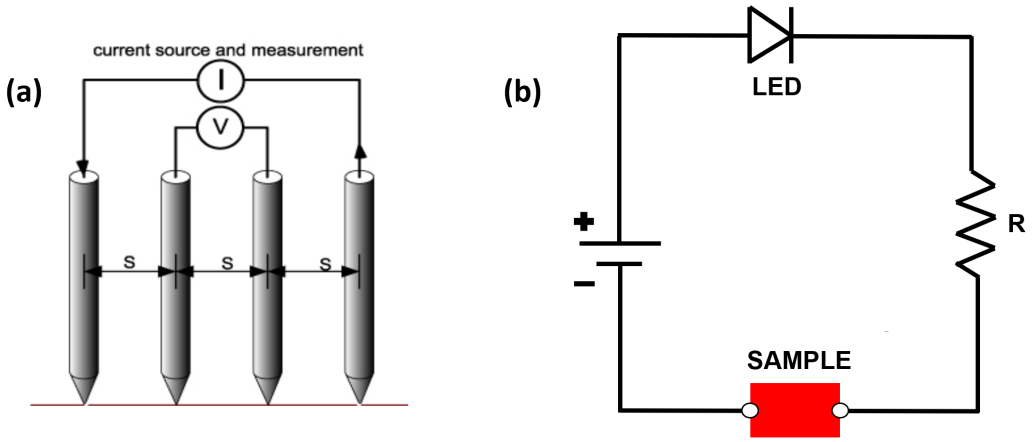

Figure 16. (a) Example of four point probe functionality [65] (b) example of circuit in series

Another method utilized to measure the electrical conductivity of a material is by creating a circuit in series as shown in Figure 16b. The sample would be located between the circuit and the voltage and current would be measured to find the resistance of the sample. The voltage will be measured with a multimeter where the sample is connected at and the current will be measured with a multimeter anywhere in the circuit since it is the same throughout the whole circuit. Obtaining both voltage and current, the resistance of the sample can be found by applying Equation 11. Equation 13 will then be applied to obtain the electrical conductivity of the sample.

3.3.3 Thermal Conductivity Testing

Like electrical conductivity, thermal conductivity is essential to calculate the thermoelectric properties of materials. Thermal conductivity in a material is the ability of a

material to transfer or conduct heat. There are various methods to evaluate the thermal conductivity of materials such as, the Raman-shift method, time-resolved optical pump-and-probe measurements, transient 3ω on-chip measurements and IR thermography [67].

The IR thermograph method for the measurement of the in-plane thermal conductivity was used. This method is utilized for thin films in which are difficult to measure in the other methods mentioned above due to complex calibration procedures, high temperature differences, and sample preparation [67]. A steady-state temperature gradient is generated via homogeneous heating by strongly absorbed visible light and a substrate serving as a heat sink as shown in Figure 17.

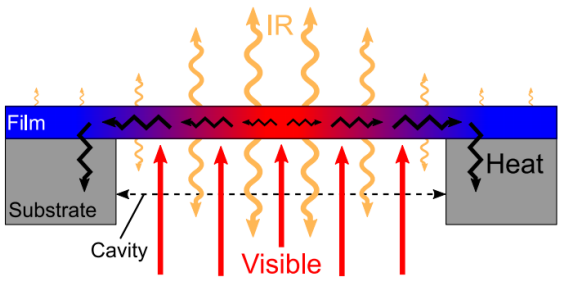

Figure 17. Schematic diagram of temperature gradient generation [67]

The material is illuminated from below with visible light in which a heat flux is generated. The substrate is opaque and serves as a shadow mask for the illumination and as a heat sink [67]. The temperature distribution of the exposed part of the material depends on the form of the cavity [67]. Using analytical or numerical models, the thermal conductivity can be obtained from the magnitude of the temperature increase considering the illumination power density, the absorption of the material and its thickness [67]. A cylindrical cavity was used and the steady state radial temperature distribution T(r) is shown in Equation 14,

$$T(r) = \frac{P_{abs}}{4k_{\parallel}d}(R^2 - r^2) + T_{substrate} \quad (14)$$

where, P_{abs} is the power density absorbed by the material from the heat source, $T_{substrate}$ is the substrate temperature, $\kappa_{\parallel}$ is the in-plane thermal conductivity, R, r, and d are the cylindrical cavity radius, radial distance from the cavity center, and the film thickness, respectively [68]. This IR thermograph method can be utilized for thin films of sufficient absorbance at the wavelength of the heating illumination [68].

3.3.4 Piezoelectric Response Testing

The piezoelectric properties of the material were also characterized for various applications. Piezoelectricity is the electric charge accumulation in response to mechanical stress. The piezoelectric voltage can be expressed as a function of mechanical stress as shown in Equation 15,

$$V = \frac{d_{ij}}{\varepsilon_{ij}} t\Delta\sigma \tag{15}$$

where, V is the output voltage of the material, d_{ij} and ε_{ij} are the piezoelectric coefficients, respectively, t is the thickness of the material and $\Delta\sigma$ is the mechanical stress applied to the material [69].

There are various methods to measuring the piezoelectric voltage response of materials. The full-wave bridge rectifier with smoothing capacitor method was used to characterize the piezoelectric voltage of the materials. Figure 18 shows the schematic of how the full-wave rectifier with smoothing capacitor is composed of and how the waveform transforms. The single-phase rectifier uses four individual rectifying diodes connected in a closed loop "bridge" configuration to produce the desired output [70]. The main advantage of the bridge circuit is not needing the use of a transformer. The four diodes labelled D_1 to D_4 are arranged in "series pairs" with only two diodes conducting current during each half cycle [70]. In the positive half cycle,

diodes D_1 to D_2 conduct in series while diodes D_3 to D_4 switch off and the current flows through the load. In the negative half cycle, diodes D_3 to D_4 conduct in series while diodes D_1 to D_2 switch off and the current flows through the load. The smoothing capacitor converts the waveform output into a smooth DC output voltage as shown in Figure 18.

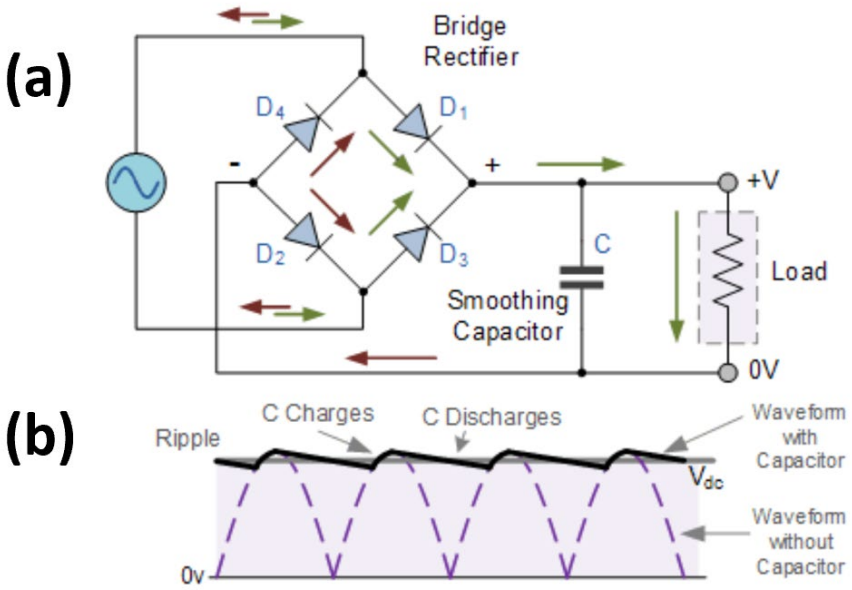

Figure 18. Example of (a) full-wave rectifier with smoothing capacitor (b) waveform with and without capacitor [70]

CHAPTER IV

METHODOLOGY

The development and characterization of nanofiber-based thermoelectric and piezoelectric composites are consisted of multiple steps such as, solution preparation, solution Forcespinning, chemical synthesis, in-situ polymerization, and doping. These steps were done to prepare the nanofiber-based composites shown in Table 6. The nanofiber-based composites were characterized and tested with various methods mentioned in the previous chapter.

4.1 Chemical Synthesis for Conducting Polymers

In the process of chemical synthesis, various materials are needed to be utilized to produce the conducting polymers as shown in Table 5. Aniline (C_6H_7N), indole (C_8H_7N), anthranilic acid ($C_7H_7NO_2$), carbazole ($C_{12}H_9N$) and dichloromethane (DCM, CH_2Cl_2) were all obtained from Sigma-Aldrich. Pyrrole (C_4H_5N) and ammonium peroxydisulfate (APS, $N_2H_8S_2O_8$) were obtained from Alfa Aesar. Sulfuric acid (H_2SO_4) and ethanol (C_2H_6O) were obtained from Fisher Scientific. Hydrochloric acid (HCl) was obtained from Acros Organics.

4.1.1 Polyaniline (PANI)

The chemical oxidative polymerization of aniline is modified and achieved by the experimental procedure in Singh *et al* (2008) [71] as shown in Figure 19. 1M HCl is prepared in an Erlenmeyer flask and 0.1M APS is calculated to drop into the 1M HCl solution in small

quantities. The Erlenmeyer flask is added a stir bar in which is left stirring on a hot plate at 300 RPM. The temperature of the hot plate is left at room temperature. The Erlenmeyer flask is then covered with aluminum foil and is left under a fume hood due to the process being highly exothermic. The polymerization process starts when the aniline monomer is placed drop wise into the Erlenmeyer flask solution. After the complete addition of the aniline monomer, the mixture is left stirring for 2 h and is left overnight. After the polymerization is finished, the dark green mixture is washed with distilled water, ethanol and 0.1M HCl and filtered using gravitational filtration. Finally, filtering out all the excess solution, the PANI is left in a furnace at 60°C overnight to obtain PANI powder.

4.1.2 Polypyrrole (PPY)

The chemical oxidative polymerization of pyrrole was modified and achieved by the same experimental procedure for PANI as shown in Figure 19. The only difference is instead of placing the aniline monomer, the pyrrole monomer is placed drop wise into the Erlenmeyer flask solution.

Figure 19. Chemical synthesis process of PANI and PPY

4.1.3 Polyindole (PIN)

The chemical oxidative polymerization of indole is modified and achieved by the experimental procedure in Mohan *et al* (2010) [72] as shown in Figure 20. An aqueous solution of 0.2M APS is calculated and placed into an Erlenmeyer flask. The Erlenmeyer flask is added a stir bar in which is left stirring on a stirring hot plate at 300 RPM. The temperature of the hot plate is left at room temperature. Then, another Erlenmeyer flask is prepared to start the polymerization process where a 0.1M indole monomer solution is created by calculating the amount of indole monomer and ethanol. The Erlenmeyer flask is covered with aluminum foil and is left under a fume hood due to the process being highly exothermic. The aqueous solution 0.2M APS is then poured into the Erlenmeyer flask with the 0.1M indole monomer solution drop wise. After the complete addition of the 0.2M APS into the 0.1M indole monomer solution, the mixture is left stirring for 2 h and is left overnight. After polymerization is finished, the black mixture is washed with distilled water and 0.2M H_2SO_4 and filtered using gravitational filtration. Finally, filtering out all the excess solution, the PIN is left in a furnace at 60°C overnight to obtain PIN powder.

4.1.4 Polyanthranilic acid (PANA)

The chemical oxidative polymerization of anthranilic acid is modified and achieved by the experimental procedure in Prakash *et al* (2010) [73] as shown in Figure 20. An aqueous solution of 0.2M APS is calculated and placed into an Erlenmeyer flask. The Erlenmeyer flask is added a stir bar in which is left stirring on a stirring hot plate at 300 RPM. The temperature of the hot plate is left at room temperature. Then, another Erlenmeyer flask is prepared to start the polymerization process where a 0.2M anthranilic acid monomer solution is created by

calculating the amount of anthranilic acid monomer and 0.5M H_2SO_4. The Erlenmeyer flask is covered with aluminum foil and is left under a fume hood due to the process being highly exothermic. The aqueous solution 0.2M APS is then poured into the Erlenmeyer flask with the 0.2M anthranilic acid monomer solution drop wise. After the complete addition of the 0.2M APS into the 0.2M anthranilic acid monomer solution, the mixture is left stirring for 2 h and is left overnight. After polymerization is finished, the dark red mixture is washed with distilled water and 0.5M H_2SO_4 and filtered using gravitational filtration. Finally, filtering out all the excess solution, the PANA is left in a furnace at 60°C overnight to obtain PANA powder.

4.1.5 Polycarbazole (PCZ)

The chemical oxidative polymerization of carbazole is modified and achieved by the experimental procedure in Prakash *et al* (2011) [74] as shown in Figure 20. A solution of 0.24M APS and 0.5M HCl is calculated and placed into an Erlenmeyer flask. The Erlenmeyer flask is added a stir bar in which is left stirring on a stirring hot plate at 300 RPM. The temperature of the hot plate is left at room temperature. Then, another Erlenmeyer flask is prepared to start the polymerization process where a 0.2M carbazole monomer solution is created by calculating the amount of carbazole monomer, dichloromethane and 0.5M HCl. The Erlenmeyer flask is covered with aluminum foil and is left under a fume hood due to the process being highly exothermic. The mixed solution 0.24M APS is then poured into the Erlenmeyer flask with the 0.2M carbazole monomer solution drop wise. After the complete addition of the 0.24M APS into the 0.2M carbazole monomer solution, the mixture is left stirring for 2 h and is left overnight. After polymerization was finished, the white mixture is washed with distilled water, dichloromethane

and 0.5M HCl and filtered using gravitational filtration. Finally, filtering out all the excess solution, the PCZ is left in a furnace at 60°C overnight to obtain PCZ powder.

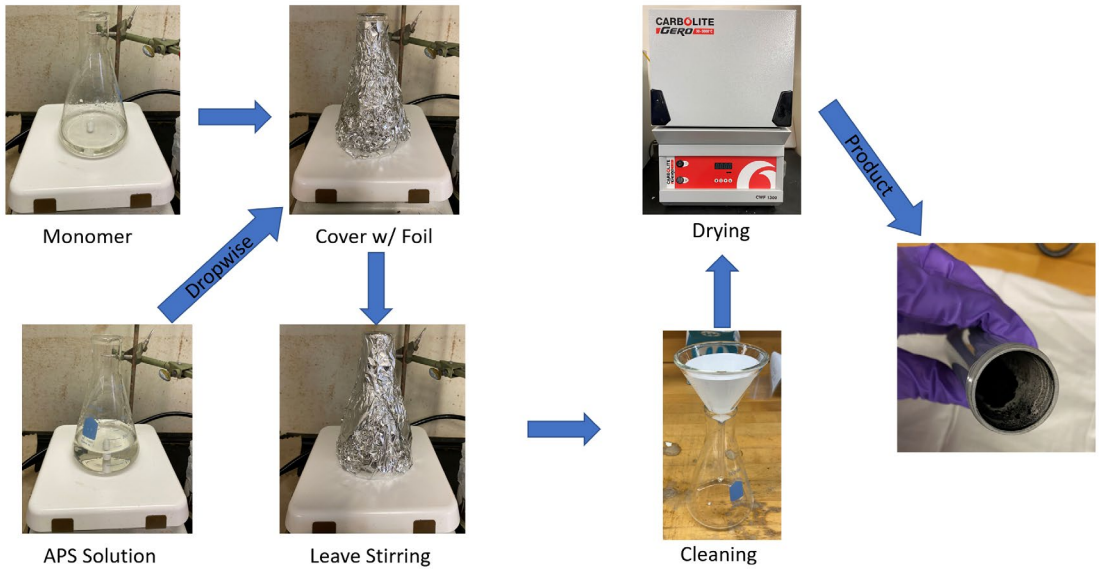

Figure 20. Chemical synthesis of PIN, PANA and PCZ

Table 5. Chemical synthesis of conducting polymers [78]

Monomer	Oxidizing Agent	Solvent	Wash	Polymer	References
Aniline	APS	HCl	HCl + Distilled Water + Ethanol	Polyaniline	[71]
Pyrrole	APS	HCl	HCl + Distilled Water + Ethanol	Polypyrrole	[71]
Indole	APS	Ethanol + Distilled Water	H_2SO_4 + Distilled Water	Polyindole	[72]
Anthranilic Acid	APS	H_2SO_4 + Distilled Water	H_2SO_4 + Distilled Water	Polyanthranilic Acid	[73]
Carbazole	APS	DCM + HCl	DCM + HCl + Distilled Water	Polycarbazole	[74]

4.2 Solution Preparation

In the solution preparation of polyvinylidene fluoride (PVDF) and polyacrylonitrile (PAN), various materials are needed to be utilized to produce the solutions for FS. KYNAR 741 PVDF powder was obtained from Arkema Inc. PAN (Molecular Weight: 150,000) powder and N,N-dimethylacetamide (DMA, C_4H_9NO) were obtained from Sigma-Aldrich. Acetone (C_3H_6O) and Acetonitrile (C_2H_3N) were obtained from Fisher Chemical. N,N-dimethylformamide (DMF, $HCON(CH_3)_2$ was obtained from Alfa Aesar. Functionalized MWCNT-COOH were obtained by Cheap Tubes.

4.2.1 Polyvinylidene Fluoride Control Solution

The development of PVDF is by solution process. The optimum concentration utilized to create fibers was 22 wt.% PVDF. The PVDF solution uses Acetone and DMA as the solvents. The PVDF solution will be the control of the experiment to observe the differences between processes as shown in Figure 21. To prepare an 8 g PVDF solution, a magnetic stir is placed inside a vial in where the PVDF solution will be placed in. 2.2 g of PVDF powder is weighed on the electronic scale and placed in the vial. 1.95 g of Acetone is weighed on the electronic scale as well and placed in a different vial. 2 mL of DMA is siphoned using a pipet controller into a different vial having a total of three vials. Both solvents are poured into the vial with the PVDF powder and magnetic stir. The vial is wrapped around the lid with wax paper. It is taken to the vortex machine to be properly mixed for 2 min. Finally, the PVDF solution is taken to a preheated silicon oil bath between 60-75°C for 1-2 h.

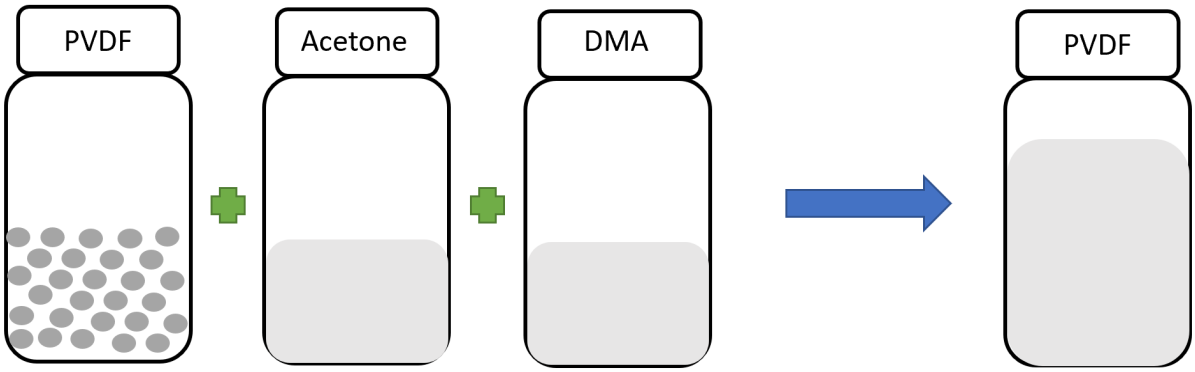

Figure 21. PVDF solution preparation

4.2.2 Polyacrylonitrile Control Solution

The development of PAN is by solution process. The optimum concentration utilized to create fibers was 12 wt.% PAN. The PAN solution uses DMF as the solvent. The PAN solution will be the control of the experiment to observe the differences between processes as shown in Figure 22. To prepare a 10 g PAN solution, a magnetic stir is placed inside a vial in where the PAN solution will be placed in. 1.2 g of PAN powder is weighed on the electronic scale and placed in the vial. 8.8 g of DMF is weighed on the electronic scale as well and placed in a different vial. The solvent is poured into the vial with the PAN powder and magnetic stir. The vial is wrapped around the lid with wax paper. It is taken to the vortex machine to be properly mixed for 2 min. Finally, the PAN solution is taken to a hot plate between 30-40°C for 12-24 h.

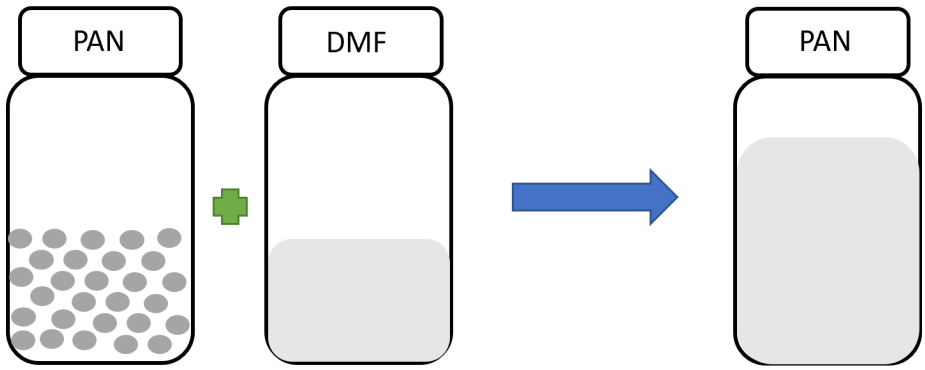

Figure 22. PAN solution preparation

4.2.3 Polyvinylidene Fluoride and Polyaniline Blend

The development of the PVDF and PANI solution is a blending process as shown in Figure 23. First, to create a 14 g solution blend, the PVDF solution has to be prepared as stated before in the PVDF control solution. While the PVDF solution is stirring, the PANI solution has to be prepared to mix it with the PVDF solution. 0.03 g of PANI is put into a different vial. 6 mL of Acetonitrile is poured into the vial with the PANI. The vial is transferred to an ultrasonic cleaner for 1 h. After the hour is up for both the PVDF solution in the silicon oil bath and the PANI solution in the ultrasonic cleaner, make sure to carefully take both the PVDF solution vial and PANI solution vial over to a safe area and drop the PANI solution into the PVDF solution. Take the combined solution over to the Vortex Mixer for 2 minutes. After the PVDF/PANI solution is mixed and the solution appears to be homogeneous, transport the solution to the silicon bath again for another hour.

4.2.4 Polyvinylidene Fluoride and Polypyrrole Blend

The development of the PVDF and PPY solution is a blending process as shown in Figure 23. First, to create a 14 g solution blend, the PVDF solution has to be prepared as stated before in the PVDF control solution. While the PVDF solution is stirring, the PPY solution has to be prepared to mix it with the PVDF solution. 0.1 g of PPY is put into a different vial. 6 mL of Acetonitrile is poured into the vial with the PPY. The vial is transferred to an ultrasonic cleaner for 1 h. After the hour is up for both the PVDF solution in the silicon oil bath and the PPY solution in the ultrasonic cleaner, make sure to carefully take both the PVDF solution vial and PPY solution vial over to a safe area and drop the PPY solution into the PVDF solution. Take the combined solution over to the Vortex Mixer for 2 minutes. After the PVDF/PPY solution is mixed and the solution appears to be homogeneous, transport the solution to the silicon bath again for another hour.

4.2.5 Polyvinylidene Fluoride and Polyindole Blend

The same blending process is used for PVDF/PIN as was used for PVDF/PPY as shown in Figure 23. The only difference is instead of using PPY, PIN is used.

4.2.6 Polyvinylidene Fluoride and Polyanthranilic acid Blend

The same blending process is used for PVDF/PANA as was used for PVDF/PANI as shown in Figure 23. The only difference is instead of using PANI, PANA is used.

4.2.7 Polyvinylidene Fluoride and Polycarbazole Blend

The same blending process is used for PVDF/PCZ as was used for PVDF/PPY as shown in Figure 23. The only difference is instead of using PPY, PCZ is used.

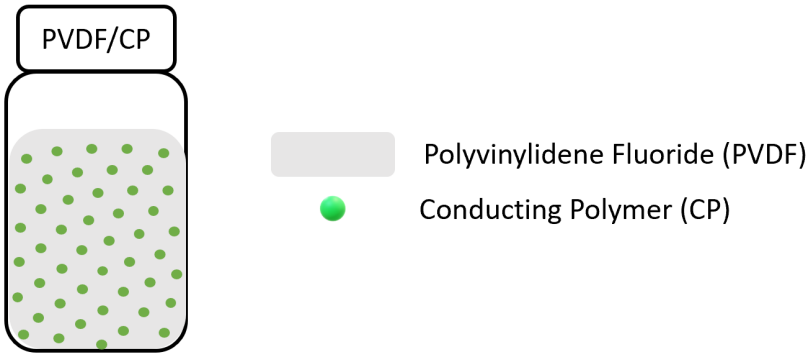

Figure 23. PVDF/conducting polymer blend solution preparation

4.2.8 Polyacrylonitrile and Multi-Walled Carbon Nanotubes (MWCNTs) Blend

The development of PAN/MWCNT is by solution process as shown in Figure 24. First to prepare a 10 g PAN/MWCNT solution, a magnetic stir is placed inside a vial in where the PAN solution will be placed in. 1.2 g of PAN powder is weighed on the electronic scale and placed in the vial. 8.8 g of DMF is weighed on the electronic scale as well and placed in a different vial. 4.4 mg of MWCNTs is weighted on the electronic scale as well and placed in a different vial. The solvent is poured into the vial with the MWCNTs. The MWCNTs with the solvent are put upon an ultrasonic pen in which will be used to disperse the MWCNTs for 6 min. The MWCNTs with the solvent is then poured into the vial with the PAN powder and magnetic stir. The vial is wrapped around the lid with wax paper. It is taken to the vortex machine to be properly mixed for 2 min. Finally, the PAN/MWCNT solution is taken to a hot plate between 30-40°C for 12-24 h.

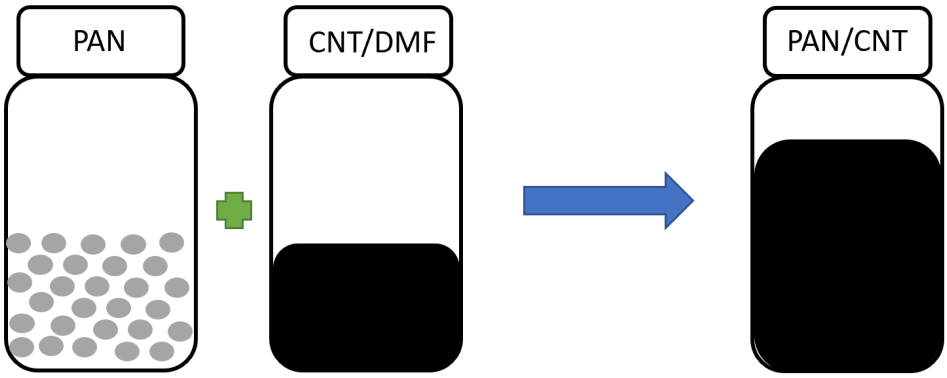

Figure 24. PAN/MWCNT polymer blend solution preparation

4.3 Solution Fiber Spinning using Forcespinning®

After the solution process, the solution will be ready to be spun using the FS method. Every 8-10 g of solution can yield approximately yield 0.4-0.6 g of fibers in a 10 x 10 cm^2 mat after spinning. The Forcespinning® method used was performed by the Cyclone L1000M from Fiberio Technology Corp as shown in Figure 25.

The materials needed for the spinning process are aluminum foil to cover the inside of the machine, a metal spinneret for spinning, a 10 x 10 cm^2 square shaped cardboard, a 3 mL syringe for the insertion of the solution, a 18G needle for the syringe, two 30G needles for the spinneret, a ring composed of metal stands for the collection of fibers and the solution prepared for spinning. 1.5 mL of the prepared solution is injected into the spinneret using the syringe.

The spinning parameters that were utilized on the cyclone differ from the PVDF control and PAN solutions in comparison to the PVDF/Conducting polymer blends. The PVDF control and PAN solutions used a speed of 8000 RPM while the PVDF/Conducting polymer blends used a speed of 4500-5000 RPM which is dependent primarily on the viscosity of the solution. The higher the viscosity of the solution, the higher the speed used for the solution and vice versa.

When spinning, the fibers will collect in the metal collector in which will be collected as shown in Figure 26. The distance between the collectors and the spinneret is 10 cm. There are eight evenly distributed vertical posts wrapped in aluminum foil in the metal collector. The fibers were collected using the square shaped cardboard wrapped in aluminum foil while maintaining the intrinsic alignment generated in between the vertical posts to create the fiber mats. The room temperature and relative humidity ranged from 20-23°C and 42-48 %, respectively. The PVDF and PVDF/Conducting polymer solutions are spun for 3-5 min per spin at the specified speed. The PAN and PAN/MWCNT solutions are spun for 0.5-1 min per spin at the specified speed.

Figure 25. FibeRio's cyclone L-1000 Forcespinning® machine [52]

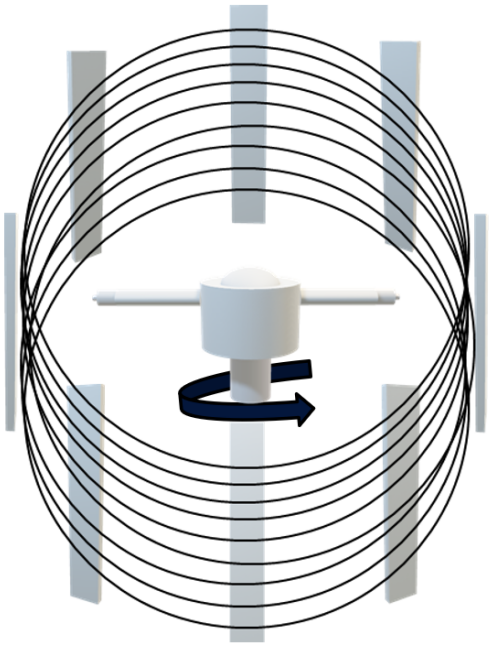

Figure 26. Fibers are created through the use of centrifugal force and subsequently deposited on metal collectors [78]

4.4 In-Situ Polymerization and MWCNT Doping

In the process of in-situ polymerization, various materials are needed to be utilized to produce the composites. Aniline (C_6H_7N), indole (C_8H_7N) and (1S)-(+)-10-Camphorsulfonic acid (CSA, $C_{10}H_{16}O_4S$) were obtained from Sigma-Aldrich. Pyrrole (C_4H_5N) and ammonium peroxydisulfate (APS, $N_2H_8S_2O_8$) were obtained from Alfa Aesar. Sulfuric acid (H_2SO_4) and ethanol (C_2H_6O) were purchased from Fisher Scientific. Hydrochloric acid (HCl) was obtained from Acros Organics. Functionalized MWCNT-COOH were obtained by Cheap Tubes.

4.4.1 Polyvinylidene Fluoride and Polyaniline In-Situ Polymerization

The in-situ polymerization of PVDF/PANI is modified and achieved by the experimental procedure in Singh *et al* (2008) [71] as shown in Figure 27. 1M HCl is prepared in a glass beaker

and 0.1M APS is calculated to drop into the 1M HCl solution in small quantities. The glass beaker is added a stir bar in which is left stirring on a hot plate at 300 RPM. The temperature of the hot plate is left at room temperature. The glass beaker is then left under a fume hood due to the process being highly exothermic. A 5 x 5 cm^2 mat of PVDF fibers is cut using clean scissors and put into another glass beaker and covered with aluminum foil. The aniline monomer is placed drop wise onto the PVDF fibers mat in the glass beaker covering the whole mat. After the complete addition of the aniline monomer, the 0.1M APS is added to the PVDF fibers in the glass beaker. The polymerization process starts when the mixture is then transported to a shaker and is left shaking for 3 h and is left overnight. After the polymerization is finished, the dark green fibers are washed with distilled water, ethanol and 0.1M HCl and filtered using gravitational filtration. Finally, filtering out all the excess solution, the PVDF/PANI fibers are left to dry overnight in room temperature to obtain the PVDF/PANI fibers.

4.4.2 Polyvinylidene Fluoride and Polypyrrole In-Situ Polymerization

The in-situ polymerization of PVDF/PPY was modified and achieved by the same experimental procedure for PANI as shown in Figure 27. The only difference is instead of placing the aniline monomer, the pyrrole monomer is placed drop wise into the PVDF fibers mat in the glass beaker covering the whole mat.

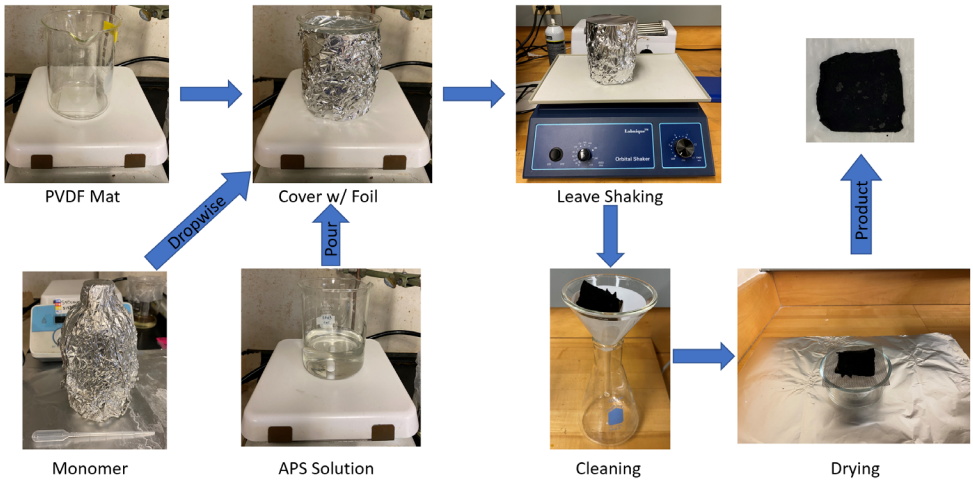

Figure 27. In-situ polymerization of PVDF/PANI and PVDF/PPY

4.4.3 Polyvinylidene Fluoride and Polyindole In-Situ Polymerization

The in-situ polymerization of PVDF/PIN is modified and achieved by the experimental procedure in Mohan *et al* (2010) [72] as shown in Figure 28. An aqueous solution of 0.2M APS is calculated and placed into a glass beaker. The glass beaker is added a stir bar in which is left stirring on a stirring hot plate at 300 RPM. The temperature of the hot plate is left at room temperature. Then, another glass beaker is prepared where a 0.1M indole monomer solution is created by calculating the amount of indole monomer and ethanol. Both glass beakers are left under a fume hood due to the process being highly exothermic. A 5 x 5 cm^2 mat of PVDF fibers is cut using clean scissors and put into another glass beaker and covered with aluminum foil. Then to start the polymerization process, 0.1M indole monomer is placed drop wise onto the PVDF fibers mat in the glass beaker covering the whole mat. The aqueous solution 0.2M APS is then poured into the glass beaker with the PVDF fibers and 0.1M indole monomer solution. After the complete addition of the 0.2M APS into the PVDF fibers and 0.1M indole monomer solution, the mixture is transported to a shaker and left shaking for 3 h and is left overnight. After

the polymerization is finished, the black fibers are washed with distilled water and 0.2M H_2SO_4 and filtered using gravitational filtration. Finally, filtering out all the excess solution, the PVDF/PIN fibers are left to dry overnight in room temperature to obtain the PVDF/PIN fibers.

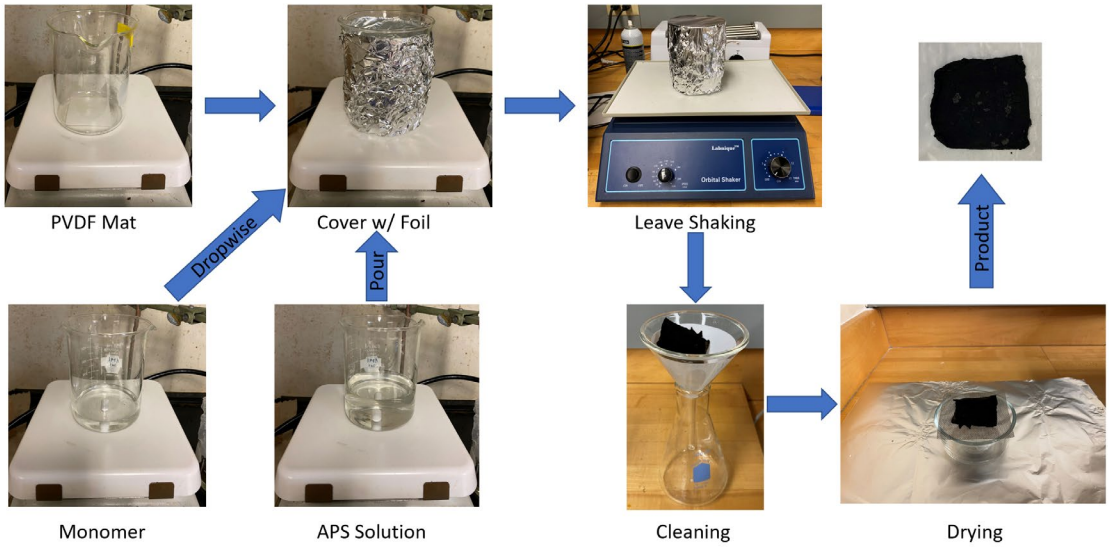

Figure 28. In-situ polymerization of PVDF/PIN

4.4.4 Polyvinylidene Fluoride and Polyaniline In-Situ Polymerization with MWCNT Doping

The in-situ polymerization of PVDF/PANI fibers is the same as in 4.4.1. After the drying overnight of the PVDF/PANI fibers, the fibers are doped in MWCNTs as shown in Figure 29. A 60 mL MWCNT solution is made by adding 30 mg of MWCNT in a 60 mL beaker of ethanol. The MWCNTs with the solvent are put upon an ultrasonic pen in which will be used to disperse the MWCNTs for 30 min. The PVDF/PANI fibers are put upon a glass beaker, covered with aluminum foil, and the dispersion of the MWCNTs are poured in the glass beaker. The glass beaker transported to a shaker and left shaking for 3 h and is left overnight. After the 24 h are finished, the black fibers are washed with distilled water and filtered using gravitational

filtration. Finally, filtering out all the excess solution, the PVDF/PANI/MWCNT fibers are left to dry overnight in room temperature to obtain the PVDF/PANI/MWCNT fibers.

4.4.5 Polyvinylidene Fluoride and Polypyrrole In-Situ Polymerization with MWCNT Doping

The in-situ polymerization of PVDF/PPY fibers is the same as in 4.4.2. The MWCNT doping is the same as 4.4.4 as shown in Figure 29.

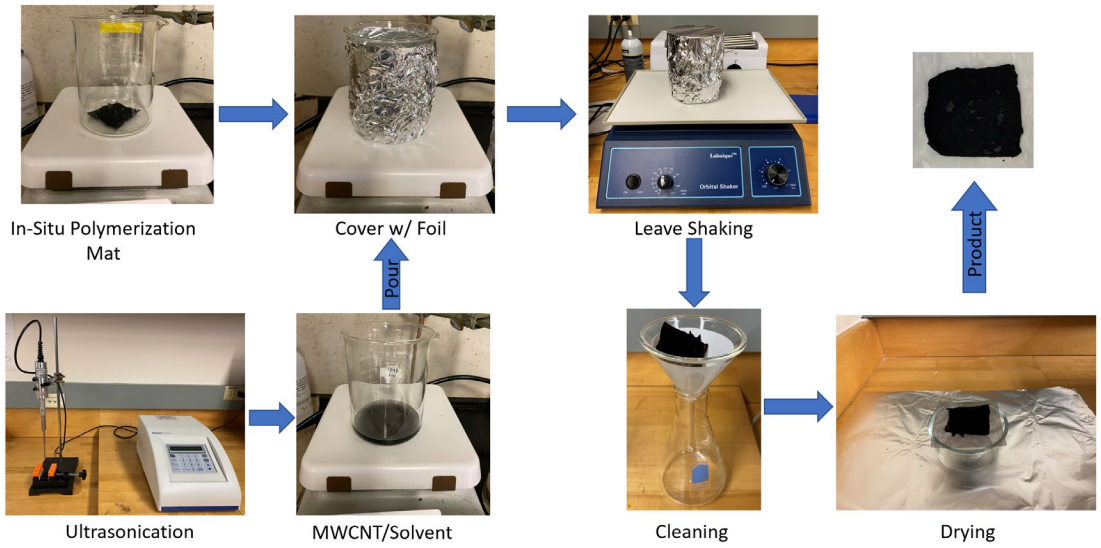

Figure 29. In-situ polymerization of PVDF/PANI and PVDF/PPY with MWCNTs doping

4.4.6 Polyvinylidene Fluoride and Polyaniline In-Situ Polymerization with CSA Doping

The in-situ polymerization of PVDF/PANI fibers is the same as in 4.4.1. After the drying overnight of the PVDF/PANI fibers, the fibers are doped in CSA as shown in the experimental procedure in Yu et al (2015) [47] as shown in Figure 30. A 60 mL CSA solution is made by adding 120 mg of CSA in a 60 mL beaker of ethanol. The CSA with the solvent are put upon an ultrasonic pen in which will be used to disperse the CSA for 12 min. The PVDF/PANI fibers are

put upon a glass beaker, covered with aluminum foil, and the dispersion of the CSA is poured in the glass beaker. The glass beaker transported to a shaker and left shaking for 3 h and is left overnight. After the 24 h are finished, the black fibers are washed with distilled water and filtered using gravitational filtration. Finally, filtering out all the excess solution, the PVDF/PANI/CSA fibers are left to dry overnight in room temperature to obtain the PVDF/PANI/CSA fibers.

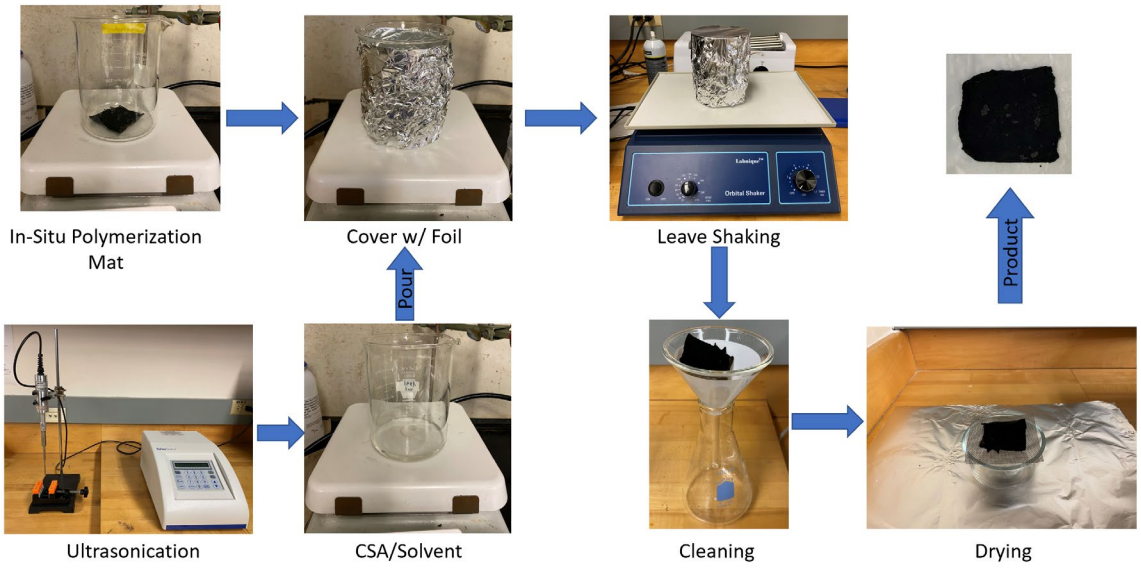

Figure 30. In-situ polymerization of PVDF/PANI with CSA doping

4.5 Heat Treatment Stabilization, Carbonization and Post-Treatment

4.5.1 PAN Carbonized Fibers at 650°C

The PAN fibers are created using the solution process as in 4.2.2. The fibers are then transferred to a furnace where the stabilization and carbonization will take place using the modification of the experimental procedure in Lozano *et al* (2018) [75] as shown in Figure 31. The PAN fibers are set into the furnace on a ceramic plate. The program of the furnace will be at

a heating rate of 3°C/min from 23°C to 280°C for stabilization in air for 6 h. Then the program of the furnace will be at a heating rate of 3°C/min from 280°C to 650°C for carbonization in argon for 3 h.

4.5.2 PAN Carbonized Fibers at 800°C

The stabilization and carbonization of the PAN fibers at 800°C is the same process as the stabilization and carbonization of the PAN fibers at 650°C in 4.5.1 as shown in Figure 31. The only parameter that changes is the carbonization from 280°C to 800°C in argon for 3 h.

4.5.3 PAN Carbonized Fibers at 950°C

The stabilization and carbonization of the PAN fibers at 950°C is the same process as the stabilization and carbonization of the PAN fibers at 650°C in 4.5.1 as shown in Figure 31. The only parameter that changes is the carbonization from 280°C to 950°C in argon for 3 h.

Figure 31. Stabilization and carbonization process for PAN fibers

4.5.4 PAN Carbonized Fibers at 650°C Nitrogen-Doped

The PAN fibers are created using the solution process as in 4.2.2. The PAN fibers are carbonized using the process as in 4.5.1. The PAN carbon fibers are then transferred to a furnace

where the post-treatment of nitrogen will take place using the modification of the experimental procedure in Wang *et al* (2015) [76] as shown in Figure 32. The PAN carbon fibers are set into the furnace on a ceramic plate. The program of the furnace will be at a heating rate of 3°C/min from 23°C to 280°C in nitrogen for 6 h. Then the program of the furnace will be at a heating rate of 3°C/min from 280°C to 650°C in argon for 3 h.

4.5.5 PAN Carbonized Fibers at 800°C Nitrogen-Doped

The post-treatment of nitrogen of the PAN carbon fibers at 800°C is the same process as the post-treatment of nitrogen of the PAN fibers at 650°C in 4.5.4 as shown in Figure 32. The only parameter that changes is the post-treatment from 280°C to 800°C in nitrogen for 3 h.

4.5.6 PAN Carbonized Fibers at 950°C Nitrogen-Doped

The post-treatment of nitrogen of the PAN carbon fibers at 950°C is the same process as the post-treatment of nitrogen of the PAN fibers at 650°C in 4.5.4 as shown in Figure 32. The only parameter that changes is the post-treatment from 280°C to 950°C in nitrogen for 3 h.

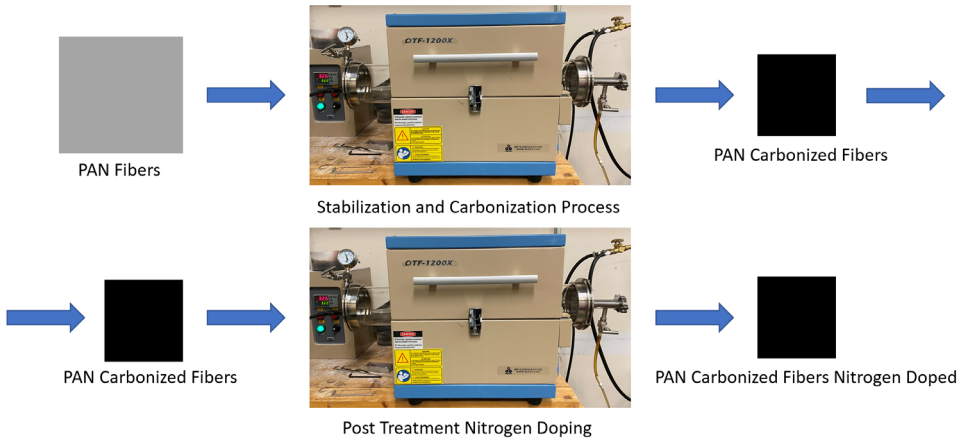

Figure 32. Stabilization and carbonization process and post treatment using nitrogen for PAN fibers

4.5.7 PAN/MWCNT Carbonized Fibers at 650°C

The PAN/MWCNT fibers are created using the solution process as in 4.2.8. The fibers are then transferred to a furnace where the stabilization and carbonization will take place using the modification of the experimental procedure in Lozano *et al* (2018) [75] as shown in Figure 33. The PAN fibers are set into the furnace on a ceramic plate. The program of the furnace will be at a heating rate of 3°C/min from 23°C to 280°C for stabilization in air for 6 h. Then the program of the furnace will be at a heating rate of 3°C/min from 280°C to 650°C for carbonization in argon for 3 h.

4.5.8 PAN/MWCNT Carbonized Fibers at 800°C

The stabilization and carbonization of the PAN/MWCNT fibers at 800°C is the same process as the stabilization and carbonization of the PAN/MWCNT fibers at 650°C in 4.5.7 as shown in Figure 33. The only parameter that changes is the carbonization from 280°C to 800°C in argon for 3 h.

4.5.9 PAN/MWCNT Carbonized Fibers at 950°C

The stabilization and carbonization of the PAN/MWCNT fibers at 950°C is the same process as the stabilization and carbonization of the PAN/MWCNT fibers at 650°C in 4.5.7 as shown in Figure 33. The only parameter that changes is the carbonization from 280°C to 950°C in argon for 3 h.

Figure 33. Stabilization and carbonization process for PAN/MWCNT fibers

Table 6. Nanofiber-based thermoelectric and piezoelectric materials	
Material	Process
PVDF (Control)	Solution
PVDF/PANI FIBERS	Chemical Synthesis/Solution Blend
PVDF/PPY FIBERS	Chemical Synthesis/Solution Blend
PVDF/PIN FIBERS	Chemical Synthesis/Solution Blend
PVDF/PANA FIBERS	Chemical Synthesis/Solution Blend
PVDF/PCZ FIBERS	Chemical Synthesis/Solution Blend
PVDF/PANI FIBERS	In-Situ Polymerization
PVDF/PPY FIBERS	In-Situ Polymerization
PVDF/PIN FIBERS	In-Situ Polymerization
PVDF/PANI/MWCNT FIBERS	In-Situ Polymerization/Doping
PVDF/PPY/MWCNT FIBERS	In-Situ Polymerization/Doping
PVDF/PANI/CSA FIBERS	In-Situ Polymerization/Doping
PAN CARBON FIBERS @ 650 °C	Solution/Heat Treatment
PAN CARBON FIBERS @ 800 °C	Solution/Heat Treatment
PAN CARBON FIBERS @ 950 °C	Solution/Heat Treatment
PAN CARBON FIBERS NITROGEN DOPED @ 650 °C	Solution/Heat Treatment/Doping
PAN CARBON FIBERS NITROGEN DOPED @ 800 °C	Solution/Heat Treatment/Doping
PAN CARBON FIBERS NITROGEN DOPED@ 950 °C	Solution/Heat Treatment/Doping
PAN/MWCNT CARBON FIBERS @ 650 °C	Solution Blend/Heat Treatment
PAN/MWCNT CARBON FIBERS @ 800 °C	Solution Blend/Heat Treatment
PAN/MWCNT CARBON FIBERS @ 950 °C	Solution Blend/Heat Treatment

4.6 Characterization

4.6.1 Scanning Electron Microscope (SEM)

Scanning electron microscope imaging was conducted using a Zeiss EVO LS10 Electron Microscope after sputter-coating the samples with gold. The SEM was operated at 1 kV. Image J software was used to estimate the average diameter of the spun nanofiber systems. Average fiber diameters were calculated from at least 250 measured fibers.

4.6.2 X-Ray Diffraction (XRD)

X-ray diffraction was conducted using a Rigaku Miniflex Benchtop XRD from $2\theta = 5°$-$60°$ at 1.2 s per step of 0.05°.

4.6.3 Fourier Transform Infrared Spectroscopy (FTIR)

Fourier Transform Infrared Spectroscopy was conducted using a Bruker® Vertex 70v FTIR spectrometer in absorbance mode from 1500 cm^{-1} to 400 cm^{-1}.

4.6.4 Thermogravimetric Analysis (TGA)

Thermogravimetric analysis was conducted using a NETZECH TG 209 F3 Taurus at a rate of 10°C/min from room temperature 25°C to 900°C for a 10 mg sample.

4.6.5 Differential Scanning Calorimetry (DSC)

Differential scanning calorimetry was conducted using a NETZECH DSC 214 Polyma. 10 mg of sample was utilized in each run. The temperature program needed to run the test

consisted of two heating and two cooling cycles with isothermal stages. Starting from -60°C, the temperature increased at a rate of 10°C/min to a final temperature of 220°C. Then an isothermal stage started for 2 min and cooled down at a rate of 10°C/min back to room temperature 25°C. Another isothermal stage started for 2 min and then the second cycle started and followed the same program as the first cycle.

4.6.6 Electrochemical Characterization

The electrochemical characterization was conducted using a Gamry 600 Electrochemical Analyzer running CV and EIS using the 600 Potentiostat/Galvanostat electrochemical workstation (Gamry Instruments,Inc.). Electrochemical characterization using cyclic voltammograms and impedance spectroscopy was performed using 0.5M H_2SO_4 as the electrolyte with a 20 mV/sec scan rate. Specifically, a three-electrode system was used to perform the cyclic voltammograms and impedance spectroscopy. A glassy carbon electrode was used as the working electrode, Ag/AgCl as the reference electrode and the platinum wire as the counter electrode, respectively.

4.7 Testing Apparatus

4.7.1 Thermoelectric Seebeck Coefficient Testing

The thermoelectric performance of the polymer fiber systems was measured using an experimental setup as shown in Figure 34. The material is positioned onto two Peltier elements to generate a temperature difference. The temperature of each side is measured with a type T thermocouple and the thermo generated voltage is measured with a microvoltmeter, using the copper of each thermocouple as an electrode. The electrode with the hottest temperature will

correspond to the negative electrode in the voltage measurement, so that the sign of the voltage corresponds to the type of majority carrier (positive for holes and negative for electrons). The measurement process consists of 2 cycles. The first cycle consists of heating and cooling the material for 5 min to create a positive and negative voltage. Then the material rests for 3 min. The second cycle repeats the first cycle.

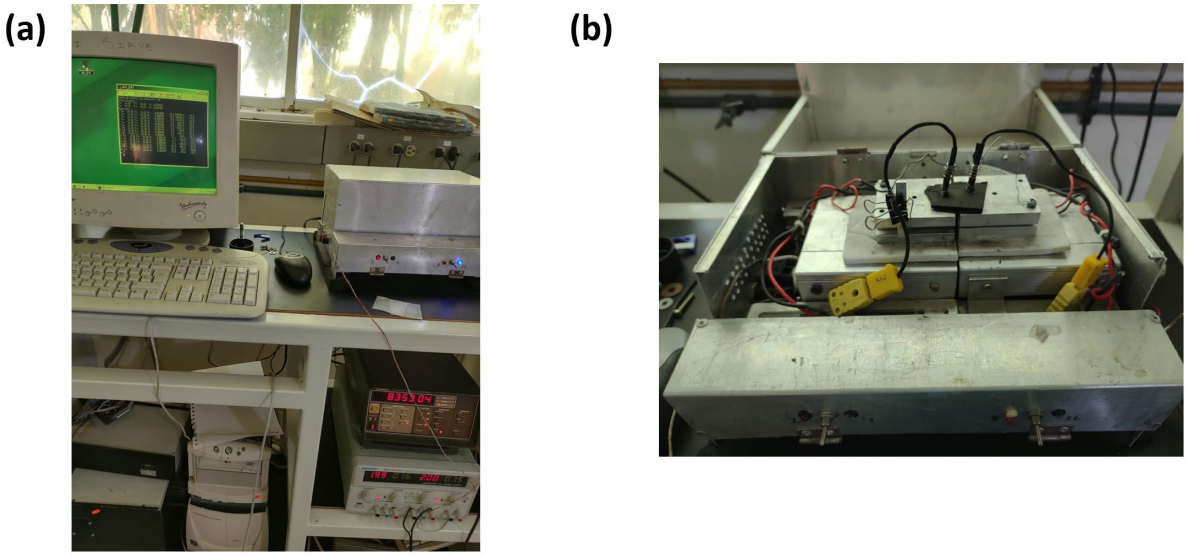

Figure 34. (a) Thermoelectric testing setup (b) peltier elements to position material

4.7.2 Electrical Conductivity Testing

The electrical conductivity performance of the polymer fibers was measured utilizing a R-CHEK RC2175 four-point probe surface resistivity meter (EDTM, Inc., Toledo, OH, USA) at room temperature as shown in Figure 35a. The four-point probe surface resistivity meter is utilized by pressing the sample in between the copper electrodes. The four-point probe surface resistivity will give the surface resistivity in units of (Ω/sq).

The electrical conductivity performance of the polymer fibers was also measured utilizing a 5V DC power supplied breadboard to create a circuit in series consisting of a LED light, a resistor and the sample as shown in Figure 35b. The sample is rolled into a cylinder and two copper strips are compressed on the sides of the sample to locate the circuit probes. The probes are held by two tweezers for stable measurements of the sample.

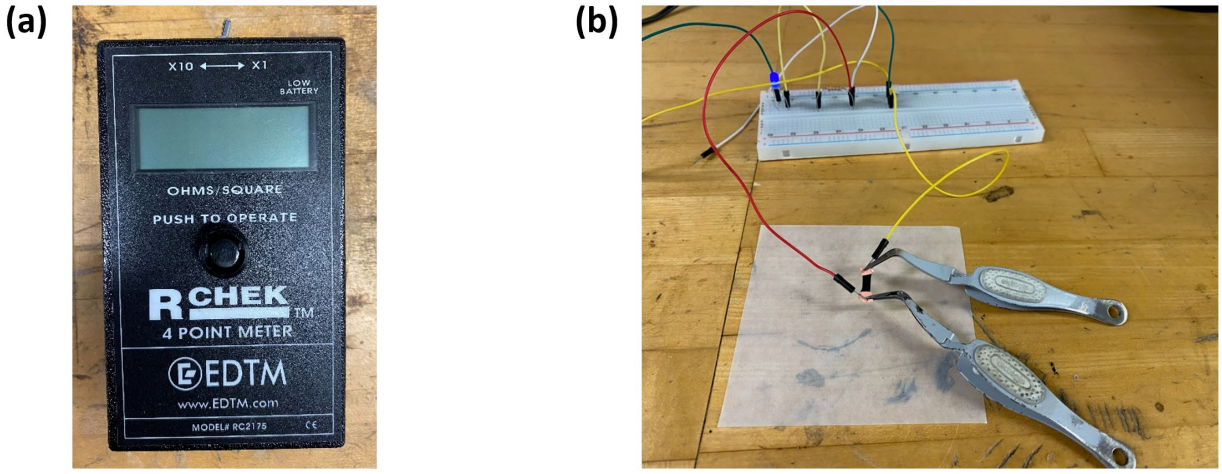

Figure 35. (a) R-CHECK RC2175 four-point probe surface resistivity meter (b) circuit in series with LED light, resistor and sample held in between tweezers

4.7.3 Thermal Conductivity Testing

The thermal conductivity performance of the polymer fibers was measured using an experimental setup utilized in Nava *et al* (2021) [68] as shown in Figure 36. A thermographic camera (FLIR x6540sc) with a spatial resolution of 640 x 512 pixels and an Indium Antimonide (InSb) detector were placed in front of the sample at 40 cm. The camera detection range is 1.5-5.5 μm in mid wave infrared band and can detect temperature differences at 20 mK. The heat sink utilized was an aluminum cylinder with a cavity of 1 cm diameter and the polymer fiber mats were placed on the aluminum cylinder. The size of the polymer fiber mats are

approximately 1.5 x 1.5 cm^2. A white lamp of 200 Watts (Newport Hg, Xe) illuminates the rear side of the freestanding polymer fiber mat for the induction of a thermal wave. The thermographic images were recorded at 10 frames per second for 6 min to detect the temperature increase until the temperature reached steady state. The measurements are done in ambient conditions with no vacuum needed, but a thermal isolating chamber is utilized to avoid air currents and decrease error.

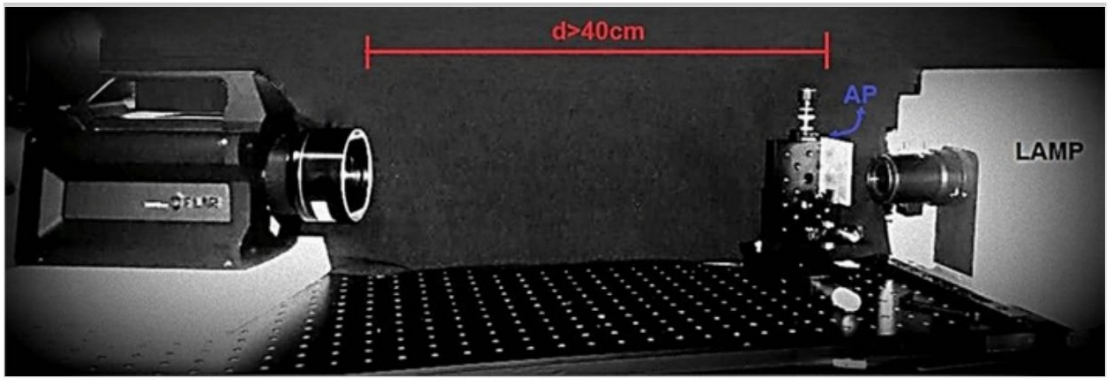

Figure 36. Experimental setup for the thermographic measurements [68]

4.7.4 Thermoelectric Response Testing

The thermoelectric performance of the constructed thermoelectric devices was measured using a powered breadboard, two thermocouple amplifiers, two thermocouples, three multimeters, and a hot plate as shown in Figure 37. The hot plate and one multimeter was utilized to measure the voltage produced by the difference of temperature from the hot plate as shown in Figure 37a. The powered breadboard was utilized to power the amplifiers to be able to measure the temperature using the thermocouples on multiple surfaces from the displays of the multimeters as shown in Figure 37b.

(a) 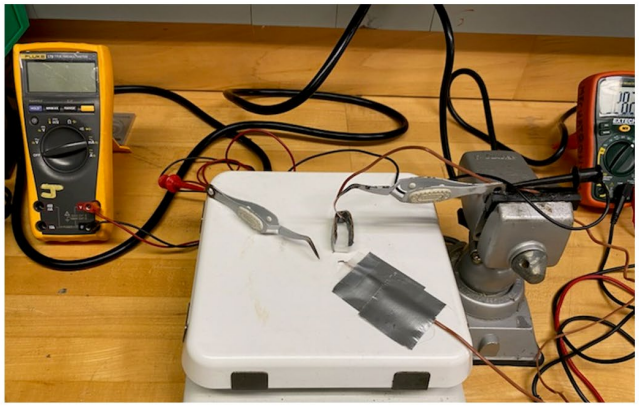 (b) 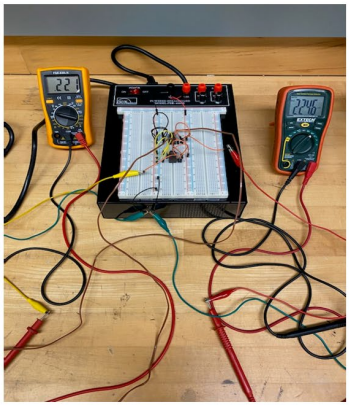

Figure 37. Experimental setup for the thermoelectric response (a) temperature difference and voltage measurement (b) thermocouples amplified for temperature measurements

4.7.5 Piezoelectric Response Testing

The piezoelectric performance of the polymer fiber systems was measured using the PVDR Pro as shown in Figure 38 in a 5 x 5 cm^2 mat between two copper electrodes connected to a Tektronix TDS 2012B oscilloscope. An air operated cylinder strikes the sample with a constant force between 130 - 200 kPa with a frequency of 1.6 Hz and the piezoelectric response is shown on the oscilloscope for data collection.

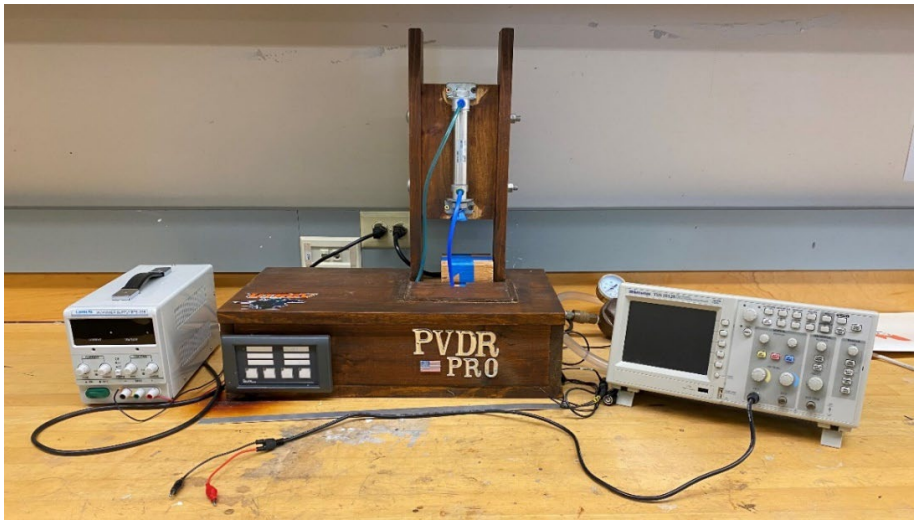

Figure 38. PVDR PRO and Tektronix TDS 2012B oscilloscope for piezoelectric response

CHAPTER V

RESULTS AND DISCUSSION

5.1 Thermoelectric Results and Discussion

5.1.1 SEM and Fiber Diameter Size Analysis

As the development of the fibers systems was completed, the samples were prepared by applying gold sputtering to increase the surface conductivity of the samples to be able to view clearly on the SEM.

Figure 39 shows the comparison between PVDF fibers and PVDF+PPY in-situ polymerization fibers. As shown in Figures 38a and 38b, it shows the PVDF fibers having an average fiber diameter of 830 nm with a standard deviation of 0.27. It can be seen from the PVDF fibers, that the surface is smooth with no beads in the fibers. Figures 38c and 38d show the PVDF+PPY in-situ polymerization fibers having an average fiber diameter of 1.15 μm with a standard deviation of 0.44. Figure 39e shows the dispersed PPY particles that will be polymerized onto the PVDF fibers as shown in Figure 39f. Figure 39f is a higher magnification of the PVDF+PPY in-situ polymerization fibers showing the PPY particles polymerize onto the PVDF fibers. It can be seen from the fibers that the surface is rough due to the PPY polymerization with no beads in the fibers.

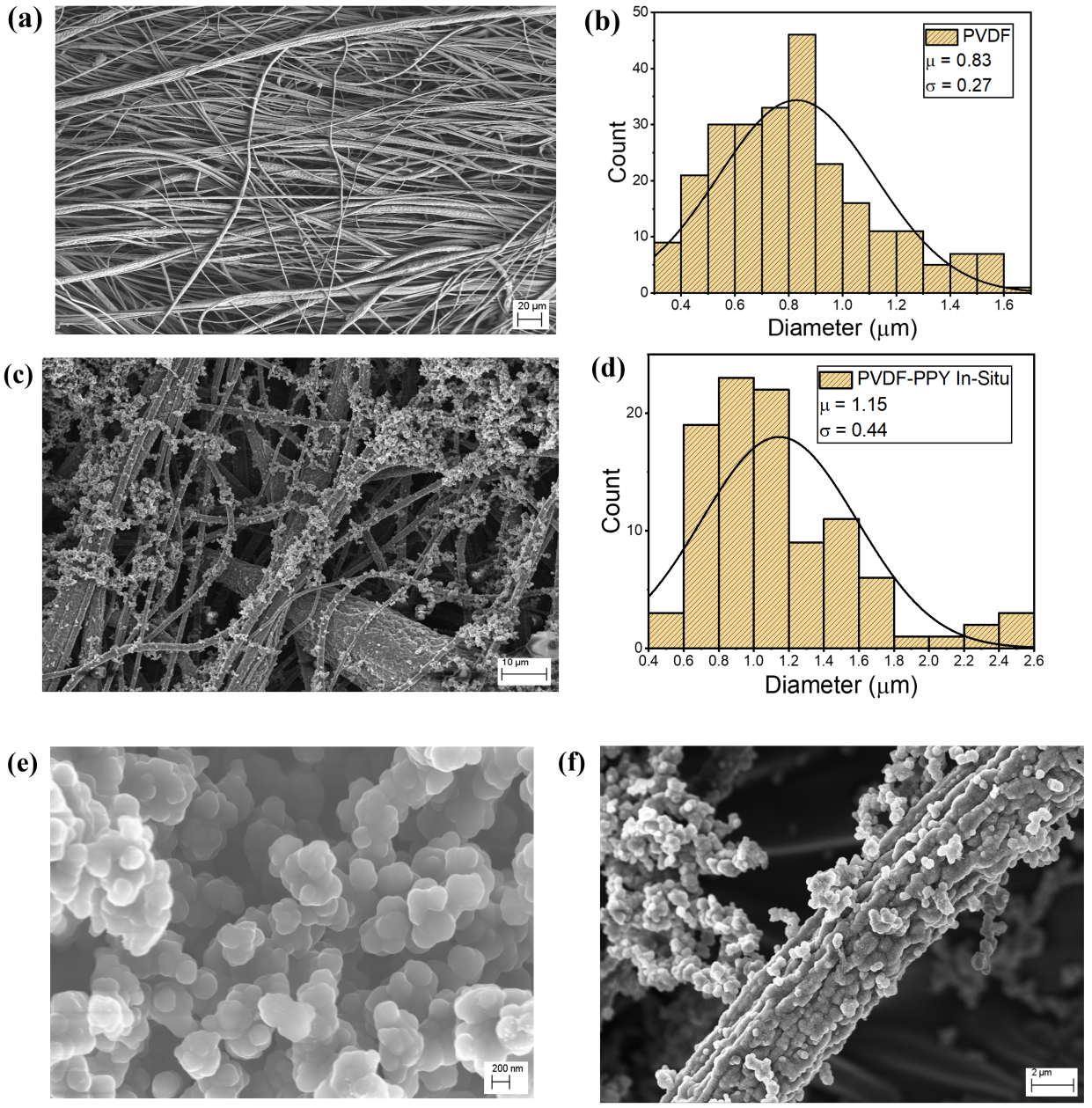

Figure 39. SEM images of (a) PVDF fibers (c) PVDF+PPY in-situ polymerization fibers (e) dispersed PPY (f) PVDF+PPY in-situ polymerization at a higher magnification and their respective histograms depicting distribution of fiber diameter b) PVDF fibers d) PVDF+PPY in-situ polymerization fibers

Figure 40 shows the comparison between PVDF fibers and PVDF+PANI in-situ polymerization fibers doped in MWCNT-COOH. As shown in Figures 39a and 39b, it shows the PVDF fibers having an average fiber diameter of 830 nm with a standard deviation of 0.27. It

can be seen from the PVDF fibers, that the surface is smooth with no beads in the fibers. Figures 39c and 39d show the PVDF+PANI in-situ polymerization fibers doped in MWCNT-COOH having an average fiber diameter of 1.19 μm with a standard deviation of 0.56. Figure 40e shows the dispersed PANI particles that will be polymerized onto the PVDF fibers as shown in Figure 40g. Figure 40f shows the MWCNT-COOH that the PVDF+PANI in-situ polymerization fibers will be doped in. Figure 40g is a higher magnification of the PVDF+PANI in-situ polymerization fibers showing the PANI particles polymerize onto the PVDF fibers and the MWCNT-COOH. It can be seen from the fibers that the surface is rough due to the PANI polymerization with the MWCNT-COOH having no beads in the fibers.

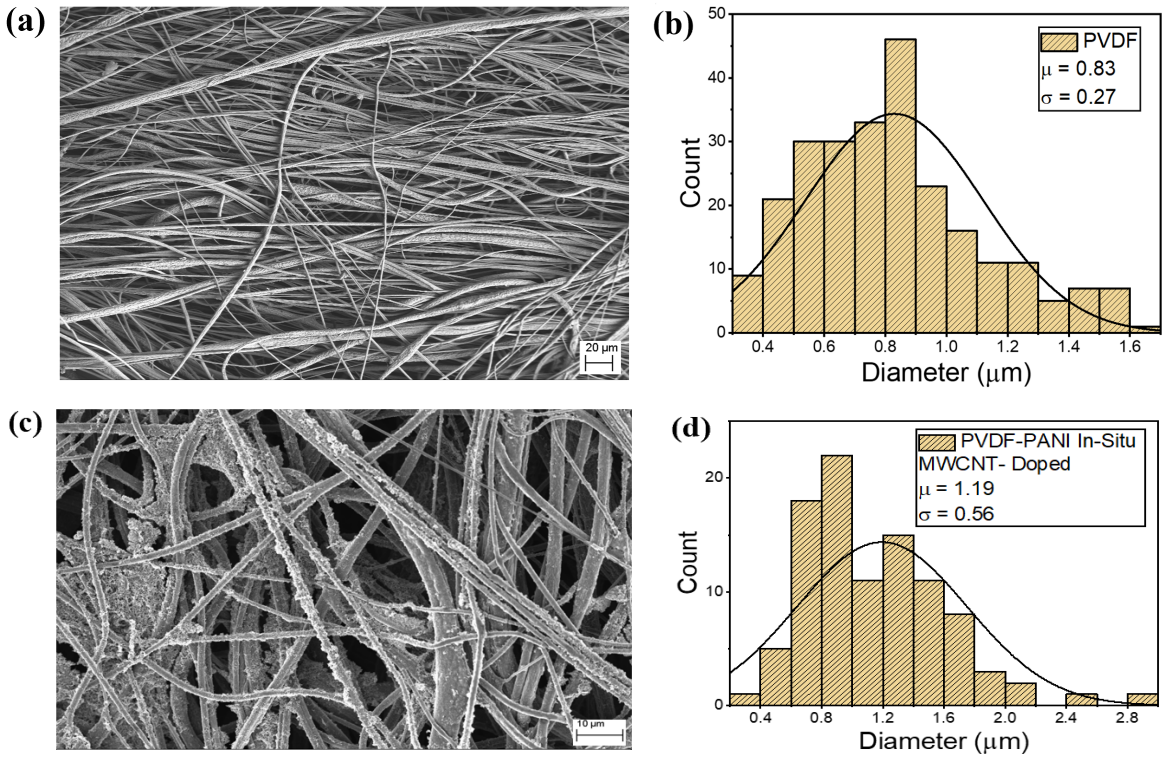

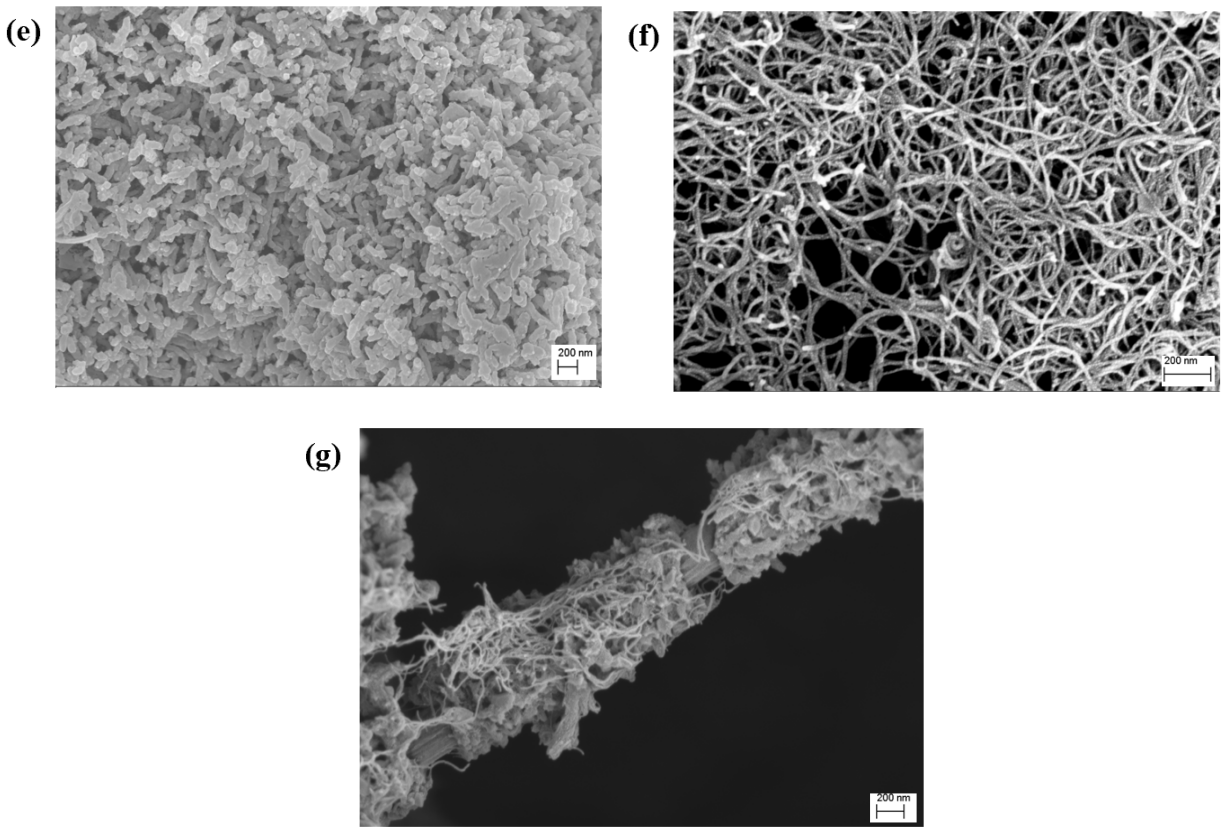

Figure 40. SEM images of (a) PVDF fibers (c) PVDF+PANI in-situ polymerization fibers doped in MWCNT-COOH (e) dispersed PANI (f) dispersed MWCNT-COOH (g) PVDF+PANI in-situ polymerization at a higher magnification and their respective histograms depicting distribution of fiber diameter b) PVDF fibers d) PVDF+PANI in-situ polymerization fibers doped in MWCNT-COOH

5.1.2 Energy-Dispersive X-ray Spectroscopy (EDS) Analysis

During the SEM analysis, the EDS analysis was utilized for the elemental analysis of the materials. Figures 41, 42 and 43 show the EDS analysis for PVDF fibers, PVDF+PPY in-situ polymerization fibers, and PVDF+PANI in-situ polymerization doped in MWCNT-COOH fibers, respectively. In all the EDS analyses, gold (Au) appears because of the gold sputtering that goes upon the samples for better visualization of the images. In Figure 41, the PVDF fibers contain carbon (C) and fluoride (F) with carbon taking most of the PVDF fibers as shown in

Table 7. In Figure 42, the PVDF+PPY in-situ polymerization fibers contain carbon (C), nitrogen (N), oxygen (O), fluoride (F) and sulfur (S) as shown in Table 8. The carbon and fluoride come from the PVDF and PPY, but specifically nitrogen comes from PPY. The increase in nitrogen shows the PPY introduced into the PVDF fibers. Oxygen gets introduced into the system from the washing with hydrochloric acid, ethanol, and the exposure to the environment. Sulfur can also occur from the exposure to the environment.

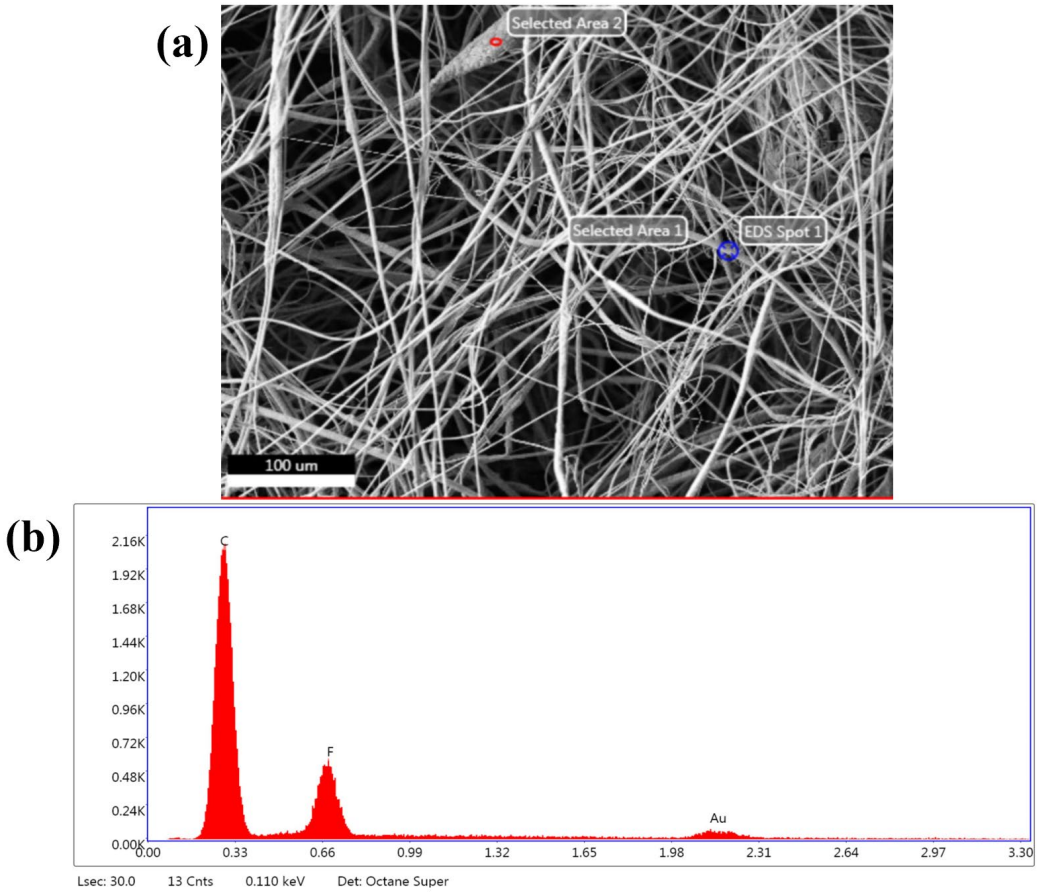

Figure 41. EDS spectroscopy (a) EDS image of PVDF fibers (b) EDS analysis of PVDF fibers

Table 7. PVDF fibers EDS analysis		
Element	Weight (%)	Atomic (%)
C K	69.72	85.03
F K	18.26	14.08
AuM	12.02	0.89

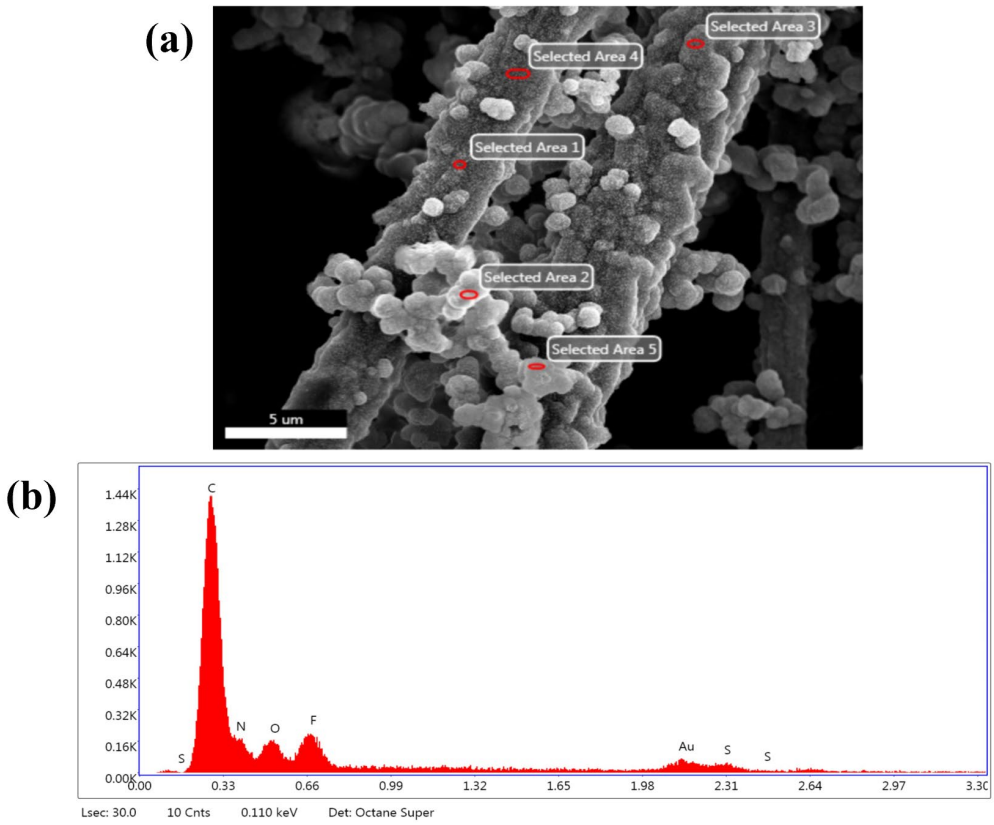

Figure 42. EDS spectroscopy (a) EDS image of PVDF+PPY in-situ polymerization fibers (b) EDS analysis of PVDF+PPY in-situ polymerization fibers

Table 8. PVDF+PPY in-situ polymerization fibers EDS analysis		
Element	Weight (%)	Atomic (%)
C K	69.72	85.03
N K	14.70	15.79
O K	4.45	4.19
F K	6.89	5.45
AuM	12.39	0.95
S K	4.49	2.11

In Figure 43, the PVDF+PANI in-situ polymerization doped in MWCNT-COOH fibers contain carbon (C), nitrogen (N), oxygen (O), fluoride (F) and sulfur (S) as shown in Table 9. The carbon and fluoride come from the PVDF, PANI, and MWCNT-COOH, but specifically nitrogen comes from PANI. The increase in nitrogen shows the PANI introduced into the PVDF

fibers. Oxygen gets introduced into the system from the washing with hydrochloric acid, ethanol, and the exposure to the environment. Chlorine gets introduced into the system from the washing with hydrochloric acid. The presence of the CPs in the in-situ polymerization fibers is confirmed with the presence specifically with the increase of nitrogen.

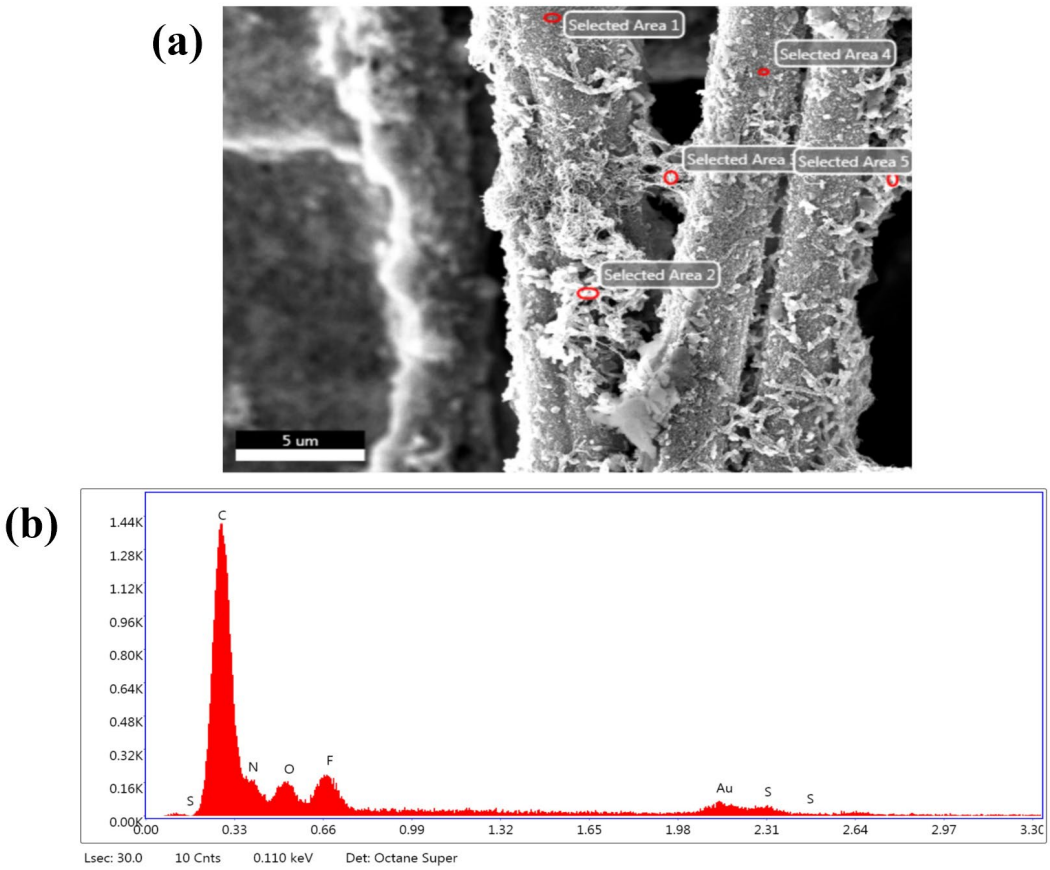

Figure 43. EDS spectroscopy (a) EDS image of PVDF+PANI in-situ polymerization doped in MWCNT-COOH fibers (b) EDS analysis of PVDF+PANI in-situ polymerization doped in MWCNT-COOH fibers

Table 9. PVDF+PANI in-situ polymerization doped in MWCNT-COOH fibers EDS analysis		
Element	Weight (%)	Atomic (%)
C K	62.18	78.43
N K	8.46	9.15
O K	2.41	2.28
F K	8.69	6.93
AuM	13.10	1.01
Cl K	5.16	2.20

5.1.3 Thermoelectric, Thermal and Electrical Properties of P-Type and N-Type Materials

Table 10. Thermal, electrical, and thermal properties of p-type and n-type materials

Sample	Seebeck Coefficient (μV/K)	Thermal Conductivity (W/mK)	Electrical Conductivity (S/m)
PVDF	13.7	4.07	-
PVDF/PANI Blend	12.9	4.5	-
PVDF/PPY Blend	16.2	4.5	-
PVDF/PIN Blend	17.8	0.32	-
PVDF/PANA Blend	14.1	1.51	-
PVDF/PCZ Blend	13.7	2.46	-
PVDF/PANI In-Situ Polymerization	-23	1.44	0.7
PVDF/PPY In-Situ Polymerization	-709	0.49	0.1
PVDF/PIN In-Situ Polymerization	19	0.20	4.3
PVDF/PANI/MWCNT-Doped In-Situ Polymerization	19.7	0.48	36.5
PVDF/PPY/MWCNT-Doped In-Situ Polymerization	-16	0.43	0.6
PVDF/PANI/CSA-Doped In-Situ Polymerization	-19.2	0.39	1.0
Carbonized PAN 650°C	-	0.22	-
Carbonized PAN 800°C	-8	0.76	3.6
Carbonized PAN 950°C	-21	0.58	12.7
Carbonized PAN 650°C Nitrogen-Doped	125.8	0.43	-
Carbonized PAN 800°C Nitrogen-Doped	-13.8	0.25	5.6
Carbonized PAN 950°C Nitrogen-Doped	-20	0.25	16.4
Carbonized PAN/MWCNT 650°C	15.6	0.21	-
Carbonized PAN/MWCNT 800°C	-10.3	0.28	2.3
Carbonized PAN/MWCNT 950°C	-19.4	0.47	20.5

To determine what material will be utilized for the thermoelectric device for the p-type and n-type materials in the next section, the thermoelectric, thermal conductivity and electrical conductivity properties must be measured for all the materials. A balance of high seebeck coefficient, high electrical conductivity and low thermal conductivity has to be chosen to obtain a high figure of merit ZT or thermoelectric device efficiency. In Table 10, the p-type and n-type

materials are distinguished by the positive and negative sign in the seebeck coefficient obtained, respectively. The highest seebeck coefficient for the p-type materials was the PAN 650°C nitrogen-doped fibers, but the PVDF+PANI in-situ polymerization doped in MWCNT-COOH fibers were chosen as the p-type material for the thermoelectric device. It was chosen rather than the PAN 650°C nitrogen-doped fibers because of its unknown electrical conductivity meaning the resistivity of the material was high since it couldn't be measured with the four-point probe. The PVDF+PANI in-situ polymerization doped in MWCNT-COOH fibers were the p-type material with a high seebeck coefficient, highest electrical conductivity, and moderate thermal conductivity. The highest seebeck coefficient for the n-type materials was the PVDF+PPY in-situ polymerization fibers and was chosen as the n-type material for the thermoelectric device. The PVDF+PPY in-situ polymerization fibers were the n-type material with the highest seebeck coefficient, low electrical conductivity, and moderate thermal conductivity. Even though, the electrical conductivity was low for the PVDF+PPY in-situ polymerization fibers, the seebeck coefficient is drastically different from the rest of the n-type materials and chosen since the seebeck coefficient is the most influential parameter to measure the figure of merit ZT.

5.1.4 Design of Thermoelectric Device

The design of the thermoelectric device was created following the design from Carroll *et al* (2012) [45]. Figure 44 shows the thermoelectric device that was constructed and utilized. Teflon was utilized as the insulator, PVDF+PANI in-situ polymerization doped in MWCNT-COOH fibers was utilized as the p-type material, and PVDF+PPY in-situ polymerization fibers was utilized as the n-type material. To be able to bond the p-type and n-type materials, graphite adhesive glue was utilized. Figure 45 shows the different images of the construction of the

thermoelectric devices. It shows four different thermoelectric devices showing one module, two modules, three modules and seventeen modules being the largest thermoelectric device that was created with the available material.

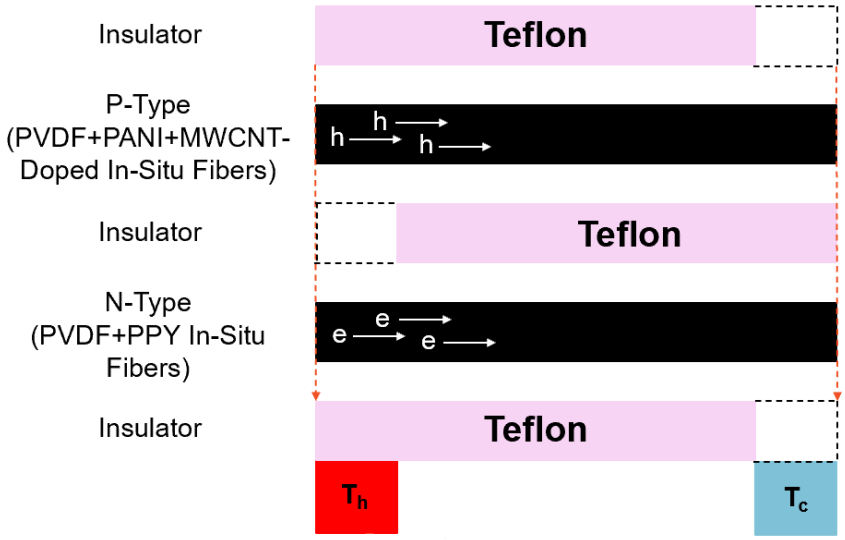

Figure 44. Design of thermoelectric device

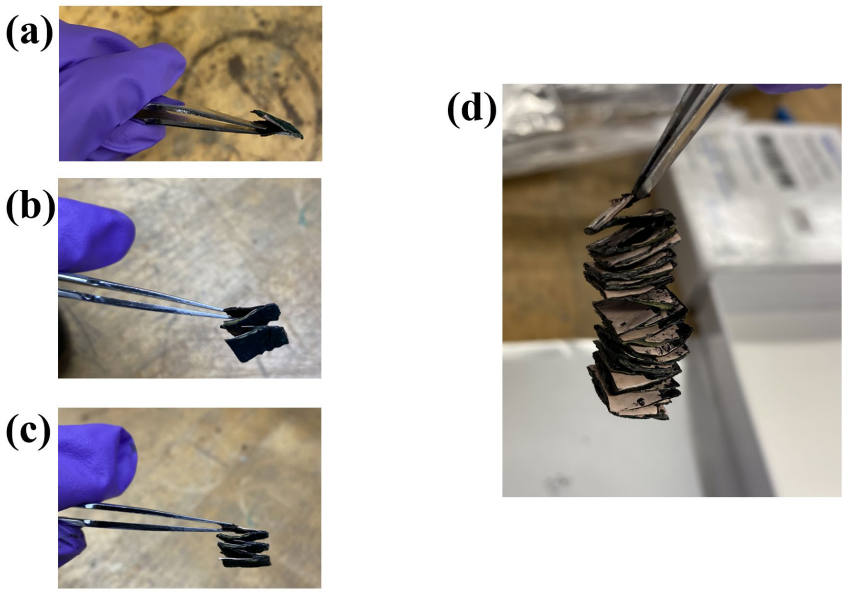

Figure 45. Thermoelectric device (a) one module (b) two modules (c) three modules (d) seventeen modules

5.1.5 Thermoelectric Response

After comparing various materials and constructing the thermoelectric device, the power output and figure of merit ZT were calculated for the thermoelectric device. The thermoelectric response of the thermoelectric device was evaluated using the thermoelectric apparatus shown in the experimental setup section. Figure 46a shows the voltage output of the thermoelectric device as the number of modules increased with a temperature difference of 100°C. Figure 46b shows the voltage output of the 17-module thermoelectric device as the difference of temperature increased. The voltage output increased as both the number of modules and difference of temperature increased. The voltage output of the thermoelectric device was 8.8 mV with a maximum number of modules being seventeen modules. The power output obtained from the thermoelectric device was 15 nW with a figure of merit ZT of 0.0002 as shown in Table 11.

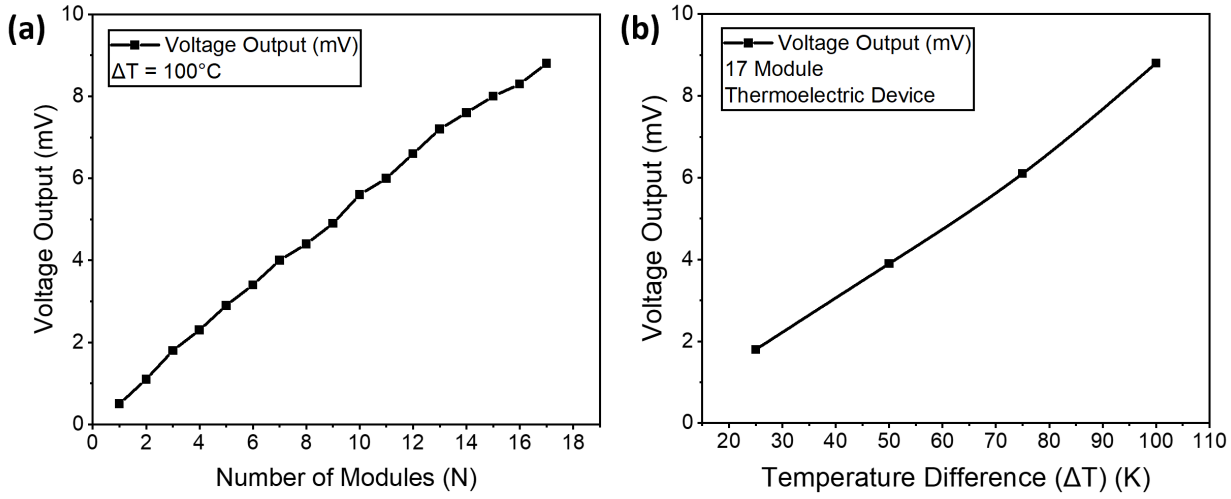

Figure 46. (a) Voltage output of thermoelectric device vs. number of modules (b) voltage output of thermoelectric device vs. temperature difference

Table 11. Thermoelectric properties of thermoelectric device

Seebeck Coefficient (μV/K)	Electrical Conductivity (S/m)	Thermal Conductivity (W/mK)	Figure of Merit ZT	Power (nW)
88	28.5	0.37	≈ 0.0002	≈ 15

5.2 Piezoelectric Results and Discussion

5.2.1 SEM Analysis

As the development of the fibers systems was completed, the samples were prepared by applying gold sputtering to increase the surface conductivity of the samples to be able to view clearly on the SEM.

Figure 47 shows scanning electron micrographs and distributions of fiber diameters of the developed nanofiber systems made of PVDF and PVDF/CPs. As observed from Figure 47 the PVDF fiber systems have larger diameters when compared to the PVDF/CP nanofiber systems. The PVDF/CP nanofiber systems showed to have negliglibe presence of beads while having an average fiber diameter of 829 nm with an average standard deviation of 267 nm. All PVDF/CP nanofiber systems depicted a rougher surface morphology with minimal presence of beads. The PVDF/PANI nanofiber systems exhibited an average fiber diameter of 354 nm with an average standard deviation of 107 nm. The PVDF/PPY nanofiber systems exhibited an average fiber diameter of 430 nm with an average standard deviation of 117 nm. The PVDF/PIN nanofiber systems exhibited an average fiber diameter of 503 nm with an average standard deviation of 248 nm. The PVDF/PANA nanofiber systems exhibited an average fiber diameter of 450 nm with an average standard deviation of 143 nm while the PVDF/PCZ nanofiber systems exhibited an average fiber diameter of 359 nm with an average standard deviation of 87 nm. Also, in Figs. 1c, 1g, and 1k, bead formation is evident. This is can be due to the centrifugal forces using FS method and viscosity of the solution. To produce a polymer jet, the rotating forces must be high enough to overcome the surface tension of the solution, but if the forces are too high, the surface

tension of the solution is capable of causing the jet to break up and produce beads [38]. Also, if the viscosity is too low, the polymer jet may break up and produce beads.

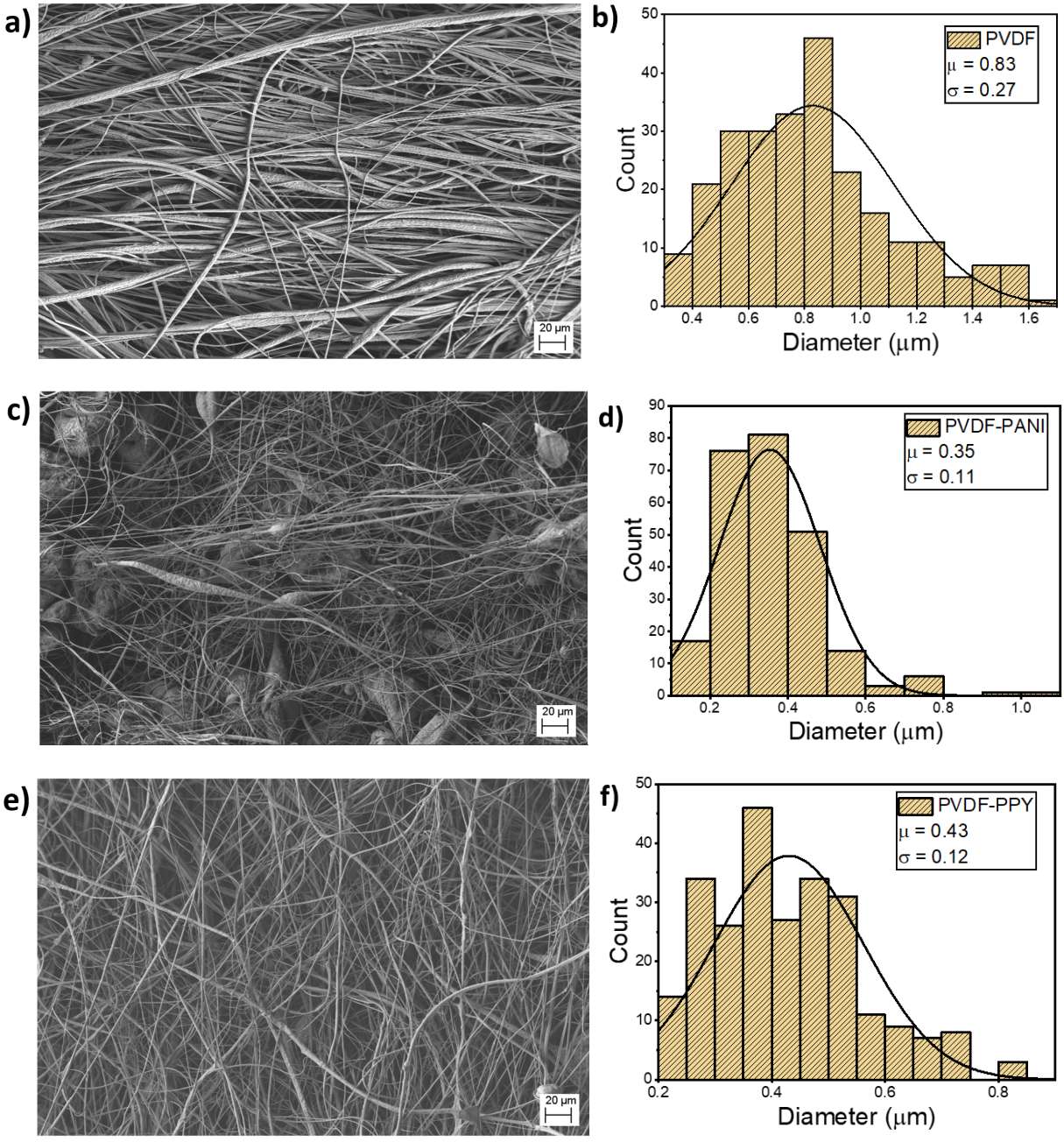

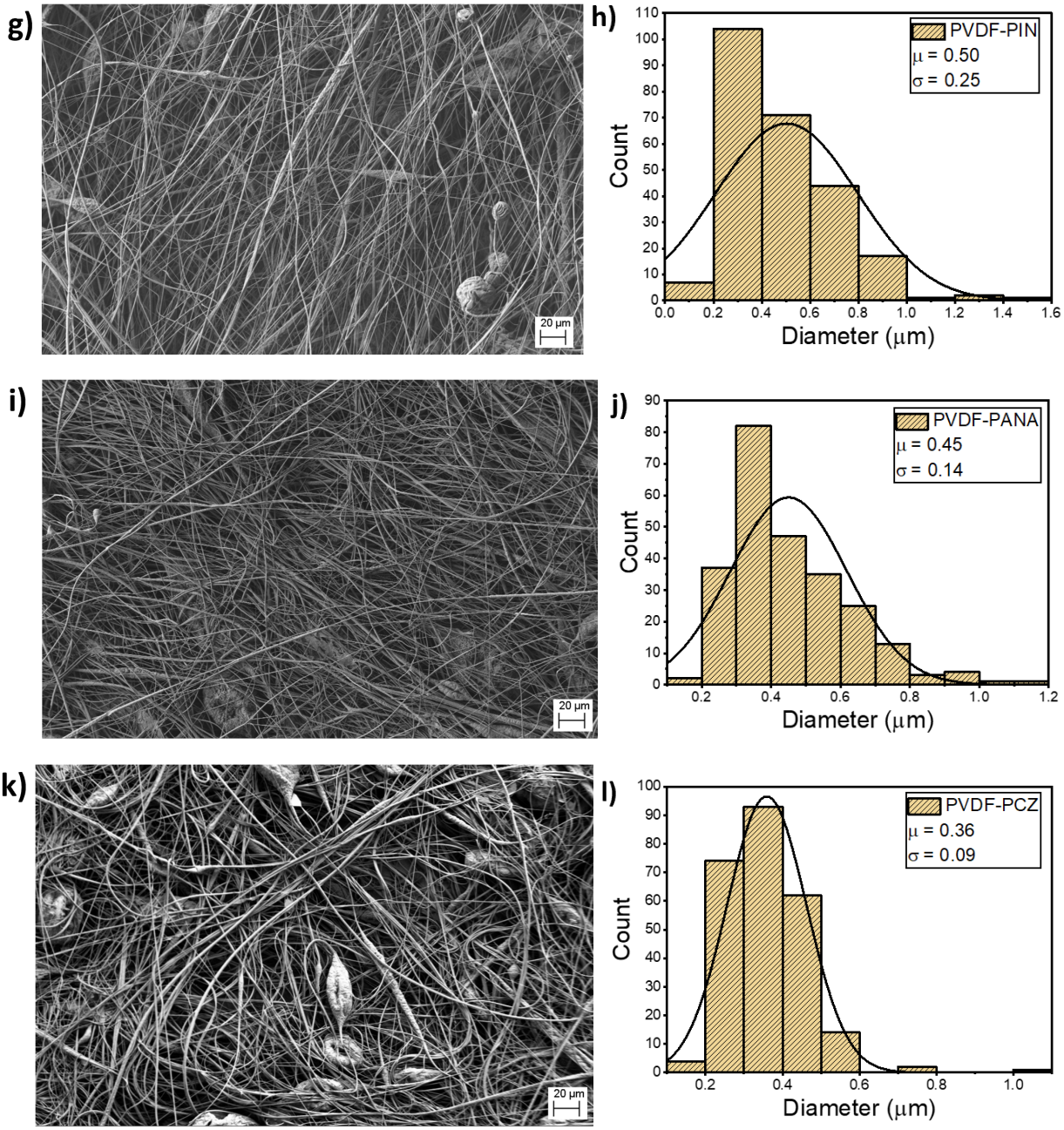

Figure 47. SEM images of a) PVDF fibers c) PVDF/PANI fibers (e) PVDF/PPY fibers g) PVDF/PIN fibers i) PVDF/PANA fibers k) PVDF/PCZ fibers and their respective histograms depicting distribution of fiber diameter b) PVDF fibers d) PVDF/PANI fibers f) PVDF/PPY fibers h) PVDF/PIN fibers j) PVDF/PANA fibers l) PVDF/PCZ fibers [78]

5.2.2 XRD Analysis

The results of the XRD analysis, shown in Figure 48, demonstrates the polymorphism of the developed PVDF/CP nanofiber systems and bulk PVDF. The bulk PVDF shows α-phase characteristic peaks corresponding to 020, 110 and 021 and are clearly observed at 17.7°, 18.3° and 26.8° [26,81]. The developed PVDF/CP nanofiber systems exhibited a higher amplitude intensity compared to the bulk PVDF. All the PVDF/CP nanofiber systems exhibited a hump in the range of 2θ = 20°- 45°. The PVDF/CP nanofiber systems show conversion to β-phase due to the elimination of the α-phase peaks shown from the bulk PVDF. The α-phase to β-phase transition occurred by the extensional elongation experienced through the centrifugal spinning process.

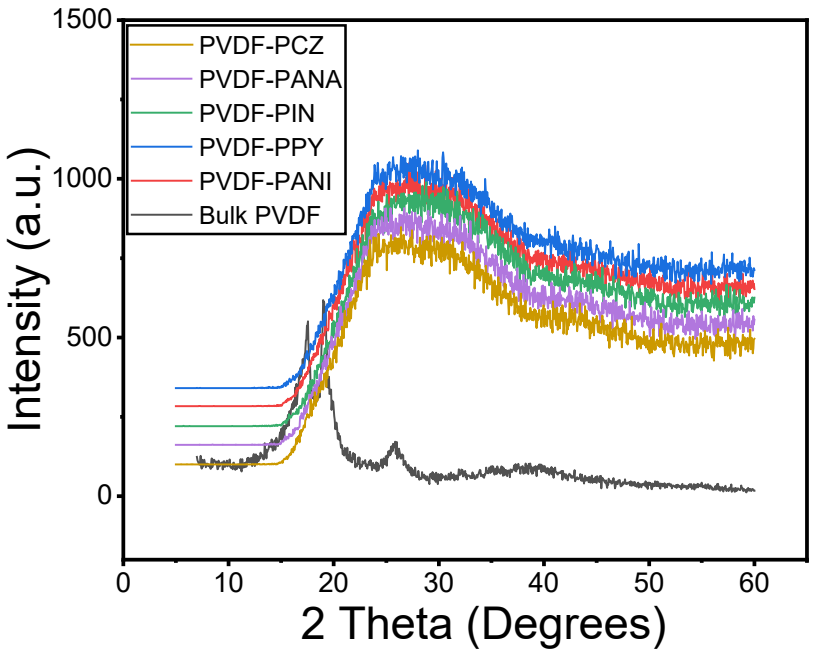

Figure 48. XRD comparison of bulk PVDF, and forcespun PVDF/CP fiber membranes [78]

5.2.3 FTIR Analysis

The conversion from α-phase to β-phase in PVDF is the primary piezoelectric effect as previously stated. The FTIR characterization was measured for the PVDF powder, PVDF and PVDF/CP nanofibers systems. Figure 49 shows the FTIR spectra for the PVDF powder, PVDF and PVDF/CP nanofiber systems. Every single α-peak and β-peak shown in Table 12 decreases and increases, respectively, in comparison from the PVDF powder to the PVDF and PVDF/CP nanofiber systems. For example, at $\lambda = 489\ cm^{-1}$, it can be observed that the peak in the powder form has a larger intensity in comparison to the PVDF and PVDF nanofiber systems. For example, at $\lambda = 840\ cm^{-1}$, it can be observed that the peak in the powder form has a smaller intensity in comparison to the PVDF and PVDF nanofiber systems. This is due to the decrease of α-phase and the increase of β-phase in the PVDF and PVDF nanofibers systems. Two of the most important β-phase peaks are at 510 cm^{-1} and 840 cm^{-1} and are caused by CF_2 bending and CH_2 and CF_2 rocking and stretching, respectively [82].

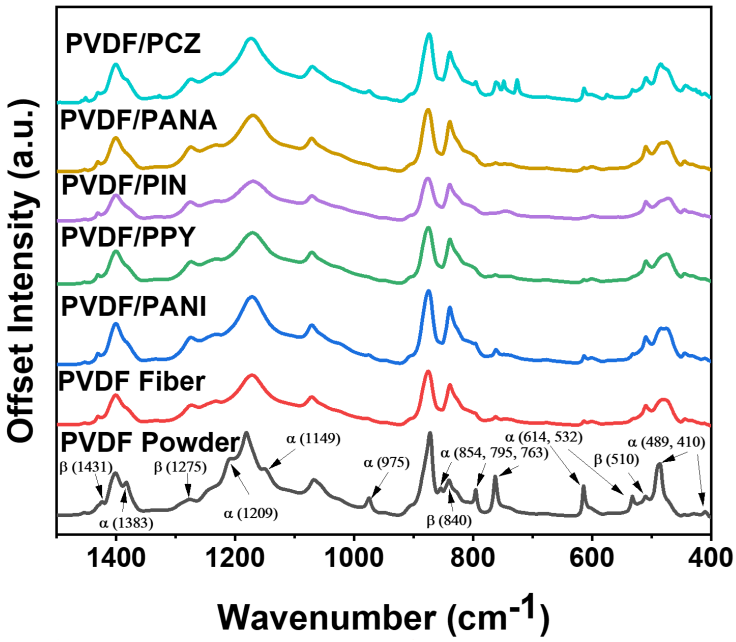

Figure 49. FTIR spectra for PVDF and PVDF/CP nanofiber systems

Table 12. FTIR spectra of α-phase and β-phase peaks [83]	
Phase	Peak
α	410, 489, 532, 614, 763, 795, 854, 975, 1149, 1209, 1383
β	510, 840, 1275, 1431

5.2.4 Thermal Analysis

The thermal analysis of the PVDF/CP nanofiber systems was conducted. The TGA results for the PVDF/CP nanofiber systems is shown in Figure 50 and it is observed that the PVDF/CP nanofiber systems show high thermal stability. It can be observed that the PVDF/CP nanofiber systems show a degradation temperature of approximately 425 °C with the exception of PVDF/PPY and PVDF/PIN at a degradation temperature of approximately 440 °C. The PVDF/PCZ nanofiber system shows a drop observed at approximately 115 °C showing high absorption of water in comparison to the other PVDF/CP nanofiber systems. The PVDF/CP nanofiber system showed a degradation weight % of approximately 26% with the exception of PVDF/PIN and PVDF/PANA showing a degradation weight % of approximately 33% and 28%, respectively.

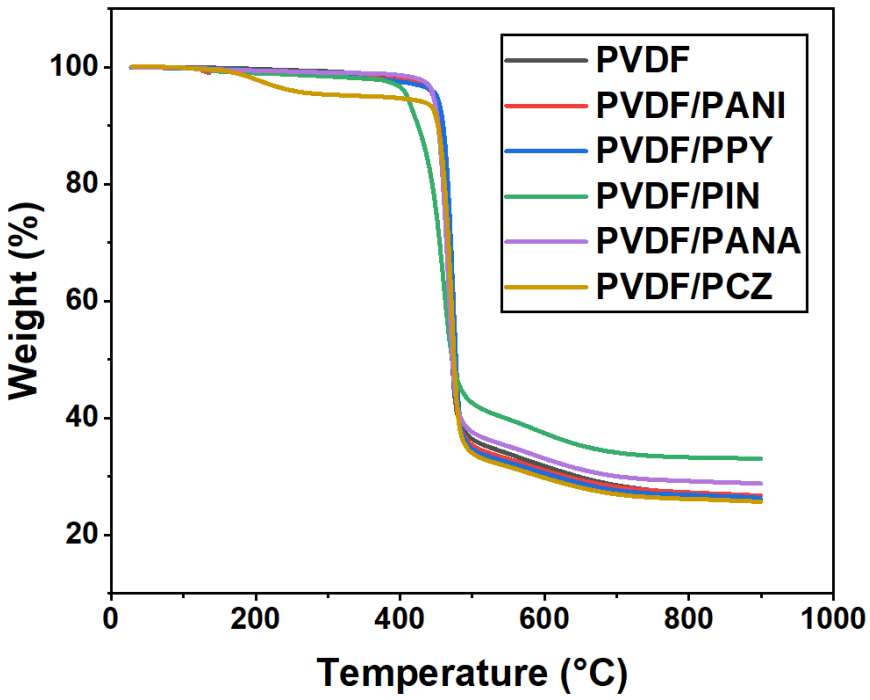

Figure 50. Thermogravimetric analysis of PVDF/CP nanofiber systems

The DSC results for the PVDF/CP nanofiber systems is shown in Figure 51. Figure 51a shows the endothermic reactions of the DSC analysis showing the melting peaks of the PVDF/CP nanofiber systems. The melting peak slightly moves to the left in comparison to the control PVDF nanofiber system however, when calculating the melting enthalpy as shown in Figure 51c, the melting enthalpy increases for all the PVDF/CP nanofiber systems. Figure 51b shows the exothermic reactions of the DSC analysis showing the crystallization peaks of the PVDF/CP nanofiber systems. It is observed in Figure 51d that the conducting polymer introduced into the PVDF either produces a nucleating effect or hinders the crystallization of the material. In most of the PVDF/CP nanofibers systems, the conducting polymer produces a nucleating effect with the exception of PVDF/PPY and PVDF/PIN producing a hindering effect. Another observed property of the PVDF/CP nanofiber systems is the similarity of the melting enthalpies to the degree of crystallinity. The melting enthalpies of the PVDF/CP nanofiber

systems are similar to the degree of crystallinity because of the theoretical heat of fusion of PVDF being approximately 105 J/g [81]. The degree of crystallinity was calculated by Equation 16,

$$\Delta X = \frac{\Delta H_f}{\Delta H_{100}} * 100 \tag{16}$$

where, ΔX is the degree of crystallinity, ΔH_f is the melting peak enthalpy and ΔH_{100} is the theoretical heat of fusion of PVDF.

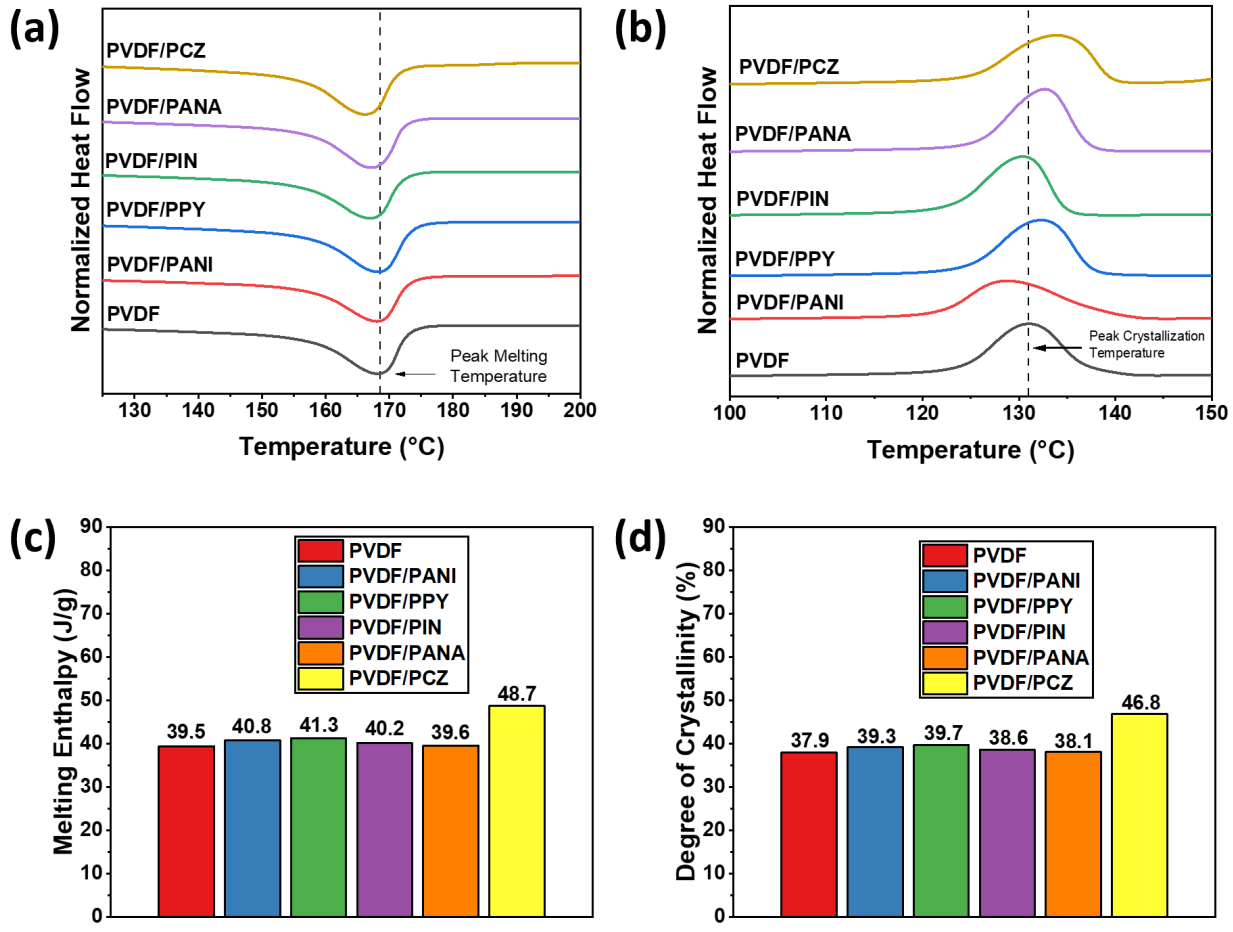

Figure 51. Differential scanning calorimetry of PVDF/CP nanofiber systems (a) endothermic reactions (b) exothermic reactions (c) melting enthalpies (d) degree of crystallinity (%)

5.2.5 Electrochemical Characterization Analysis

The electrochemical characterization was measured for the pure CPs and PVDF/CP nanofiber systems. Cyclic voltammogram and impedance spectra were evaluated to assess the charge storage and conductive properties of CPs and PVDF/CP nanofiber systems. Charge storage of our developed systems was calculated using equation 17 reported by Audichon et al. [84] below where v is the scan rate, m is the mass in milligrams of the catalyst deposited on the working electrode, s is the surface area of the working electrode, E_1 and E_2 are limits of potential of the integration curves, and $\int_{E_1}^{E_2} i(E)dE$ is the integration of the cyclic voltammogram curve. The voltammetric charge (q*) was obtained from the cyclic voltammogram [85,86].

$$q^* = \frac{1}{vms}\int_{E_1}^{E_2} i(E)dE \tag{17}$$

Figures 52a to 52e show the cyclic voltammograms for the PVDF/CP nanofiber systems (PVDF/PANI, PVDF/PANA, PVDF/PIN, PVDF/PPY and PVDF/PCZ, respectively) and were carried out using 0.5M H_2SO_4 as electrolyte at a scan rate of 20 mV/sec. The overall cyclic voltammogram for the PVDF/CP nanofiber system reflects higher q* values when compared to the pure CPs as tabulated in Table 13. The introduction of CPs untangles the PVDF fibers allowing the electrons to flow throughout the system [87]. In the case of the PVDF/PANI and PVDF/PANA nanofiber systems, q* is significantly higher than PANI and PANA alone. In the case of the PVDF/PPY, PVDF/PIN and PVDF/PCZ nanofiber systems, q* shows also to be larger than PPY, PIN and PCZ alone though, the difference was not significant. This can be explained given the overoxidation that CPs were exposed to during chemical synthesis. Electrochemical properties were further explained by analyzing the impedance spectra (EIS) at

0.35 V. Figure 52f shows Nyquist plots taken from the impedance spectra for PVDF and PVDF/CPs nanofiber systems.

Table 13. Total charge accumulation (q*) of CPs and PVDF/CPs [78]			
CP	q* (Coulomb))	PVDF/CP	q* (Coulomb))
Polyaniline	7.70E-05	PVDF/PANI	4.12E-01
Polypyrrole	1.66E-04	PVDF/PPY	2.2E-04
Polyindole	7.24E-05	PVDF/PIN	1.20E-04
Polyanthranilic Acid	2.29E-04	PVDF/PANA	7.67E-03
Polycarbazole	6.31E-03	PVDF/PCZ	9.59E-03

The charge transfer resistance (Rct) in the Nyquist plots gives a rough idea about the electrical properties of the PVDF and PVDF/CP nanofiber systems over the glassy carbon electrode surface. In the Nyquist plots, the semicircle corresponds to the charge transfer resistance (Rct) in the solution which is directly related to the electrical conductivity of the fiber systems [88]. In Figure 52f, the Rct for PVDF is higher than all the PVDF/CPs nanofiber systems. The Rct measured for the PVDF, PVDF/PANI, PVDF/PPY, PVDF/PIN, PVDF/PANA, and PVDF/PCZ nanofiber systems were 876 KΩ, 114 KΩ, 726 KΩ, 317 KΩ, 113 KΩ, and 628 KΩ, respectively.

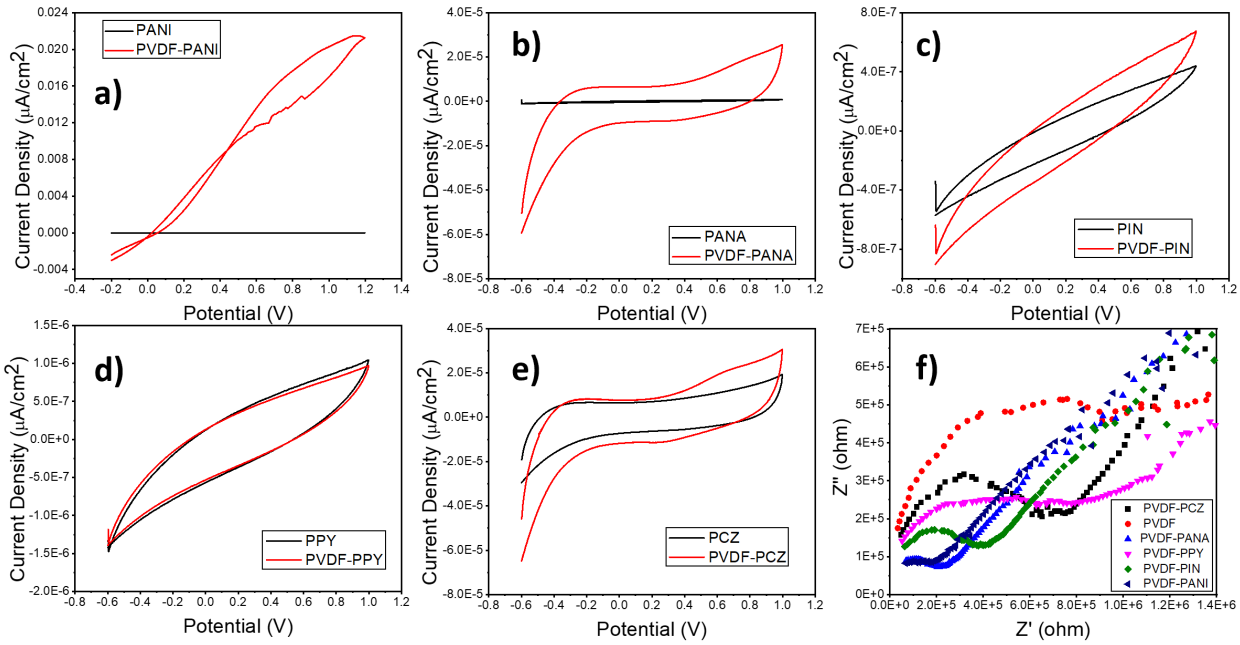

Figure 52. Cyclic voltammetry of a) PANI nanoparticles and PVDF/PANI nanofibers b) PANA nanoparticles and PVDF/PANA nanofibers c) PIN nanoparticles and PVDF/PIN nanofibers d) PPY nanoparticles and PVDF/PPY nanofibers e) PCZ nanoparticles and PVDF/PCZ nanofibers and f) Nyquist plot for PVDF nanofibers and PVDF/CP nanofibers [78]

The electrical properties of the PVDF/CP nanofiber systems analyzed from the CV and Nyquist plots show higher current density, q*, and lower Rct. All of the PVDF/CP nanofiber systems showed a significant difference in q* and Rct except for the PVDF/PPY nanofiber system. This could be due to the overoxidation of PPY. The improvement of the electrical properties of the PVDF/CP nanofiber systems is attributed to the charge transport showing strong dependence on the conducting polymer chain orientation along the fiber axis and the introduction of CPs untangling the PVDF fibers allowing the electrons to flow throughout the system [87, 89].

5.2.6 Piezoelectric Response

After comparing the electrochemical properties for the PVDF/CP nanofiber systems, the piezoelectric properties of the PVDF and PVDF/CP nanofiber systems were measured. The

piezoelectric response was evaluated using the PVDR PRO for the developed PVDF and PVDF/CP nanofibers systems and the results are shown in Figure 53. The PVDF fiber system obtained a mean peak-to-peak voltage of 4.41 V with a standard deviation of 0.64 V. By introducing the CPs into the PVDF fiber system, the piezoelectric response of the PVDF/CP nanofiber systems increased. The mean peak-to-peak voltages (μ) and standard deviations (σ) of the PVDF/CP nanofiber systems are shown in Figure 53. The PVDF/PPY nanofiber system obtained the highest peak-to-peak voltage of 15.56 V with a standard deviation of 1.15 V. Most of the PVDF/CP nanofiber systems had a larger peak towards the negative portion of the plot except for the PVDF/PPY nanofiber system because of the way the positive and negative clips of the oscilloscope were set upon the device. The high peak and low peak on either the positive or negative portion of each plot corresponds to the compression and recovery status of the nanofiber systems, respectively.

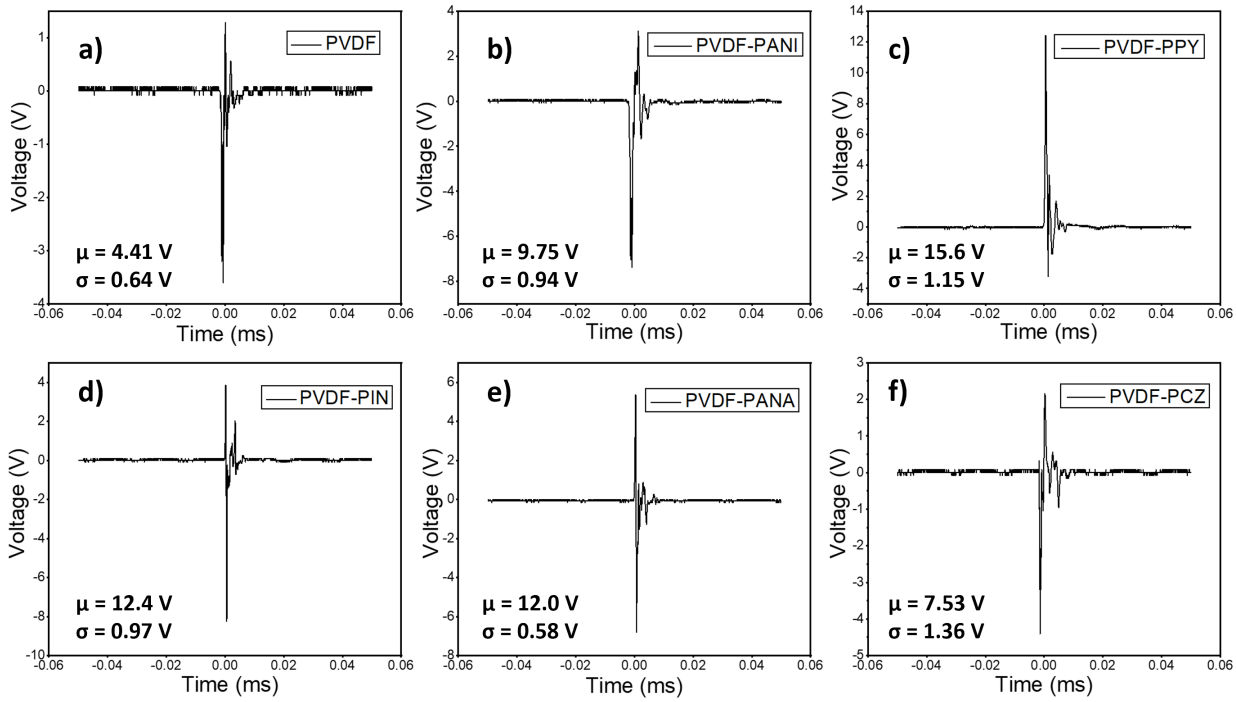

Figure 53. Piezoelectric response for a) PVDF nanofibers b) PVDF/PANI nanofibers c) PVDF/PPY nanofibers d) PVDF/PIN nanofibers e) PVDF/PANA nanofibers f) PVDF/PCZ nanofibers μ is the mean peak-to-peak voltage and σ is the standard deviation [78]

The improvement on the piezoelectric response of the PVDF/CP nanofiber systems in comparison to the PVDF fiber system is attributed to two mechanisms. The first mechanism can be explained as a network structure of the fibers within the PVDF/CP nanofiber system that are forced to touch each other under pressure, reducing the distance and increasing the contact between the fibers, which is beneficial to form new conducting pathways during compressive stress [90, 91]. The second mechanism is explained by the electrostatic forces between the PVDF fibers and the CPs. PVDF has a fluorine (F) atom, which is highly electronegative in nature, while all the CPs contain nitrogen (N) with a lone pair creating polar covalent bonds. These polar covalent bonds will create high electrostatic forces in the PVDF/CP nanofiber systems thus creating large dipole moments and strong electric polarizations increasing piezoelectric response.

CHAPTER VI

CONCLUSION

The production of the nanofiber systems for both the thermoelectric and piezoelectric applications was accomplished using the FS technique. Utilizing the FS technique prompted the construction of flexible, lightweight, compact, carbon-based composites with the increase β-phase of the nanofiber systems.

Different processes such as chemical synthesis, blends, in-situ polymerization, carbonization and doping of different materials were utilized. The chemical synthesis, in-situ polymerization and blends resulted in obtaining results in the thermoelectric and piezoelectric applications.

Different CPs were utilized with PVDF to increase the thermoelectric and piezoelectric performance in comparison to pure PVDF fine fiber membranes. MWCNTs-COOH, CSA and carbon fibers were also utilized to increase the thermoelectric and piezoelectric performance. The thermoelectric device was constructed by the highest p-type and n-type material while the piezoelectric performance was measured using the PVDF/CP nanofiber blends.

In comparison of the morphology of the p-type and n-type materials utilized in the thermoelectric device, the p-type and n-type materials had larger diameter size of fibers. In comparison of the morphology of the PVDF and PVDF/CP fine fiber systems utilized in the piezoelectric performance, the PVDF/CP nanofiber systems had smaller diameter size of fibers.

EDS characterization of the developed p-type and n-type materials utilized in the thermoelectric device showed a significant presence of the CP due to the coating around the PVDF fibers increasing the nitrogen content.

XRD and FTIR characterization of the developed PVDF/CP nanofiber systems showed a significant transformation from α-phase to β-phase increasing polarization and piezoelectric performance. The electrochemical characterization of the developed PVDF/CP nanofiber systems showed a significant increase in electrical conductivity. The TGA and DSC thermal analysis also showed high thermal stability of the PVDF/CP nanofiber systems.

The PVDF+PPY in-situ polymerization fibers and PVDF+PANI in-situ polymerization doped in MWCNT-COOH fibers were utilized for the construction of the 17-module thermoelectric device showing a maximum voltage output of 8.8 V and maximum power output of 15 nW. The addition of modules and increase of difference of temperature increased the voltage output of the thermoelectric device. Future studies will include the X-Ray Photoelectron Spectroscopy (XPS) on the p-type and n-type materials utilized in the thermoelectric device. To optimize the single layer ZT figure of merit of both the p-type and n-type materials and experiment on higher differences of temperature to produce higher power output. To experiment on creating hybrid composites using organic and inorganic materials.

The PVDF/CP nanofibers systems all obtained a higher piezoelectric response than the PVDF fine fiber system. The PVDF/PPY nanofiber system obtained the highest piezoelectric response of 15.56 V. Future studies will include mechanical properties of the developed PVDF/CP nanofiber systems.

REFERENCES

[1] Bull, S. R. (2001). Renewable energy today and tomorrow. *Proceedings of the IEEE, 89*(8), 1216-1226.

[2] Aneke, M., & Wang, M. (2016). Energy storage technologies and real life applications – A state of the art review. *Applied Energy, 179*, 350-377.

[3] Elvin, N., & Erturk, A. (2013). *Advances in Energy Harvesting Methods*. New York, NY: Springer.

[4] Beretta, D., Neophytou, N., Hodges, J. M., Kanatzidis, M. G., Narducci, D., Martin-Gonzalez, M., . . . Caironi, M. (2019). Thermoelectrics: From history, a window to the future. *Materials Science and Engineering: R: Reports, 138*, 100501.

[5] Galvani, L. (1791). De viribus electricitatis in motu musculari. Commentarius. *De Bonoiensi Scientiarum et Artium Intituo atque Academie Commentarii, 7*, 363-418.

[6] Zhang, Y., & Park, S.-J. (2019). Flexible Organic Thermoelectric Materials and Devices for Wearable Green Energy Harvesting. *Polymers, 11*(5), 909.

[7] Wang, H., & Yu, C. (2019). Organic Thermoelectrics: Materials Preparation, Performance Optimization, and Device Integration. *Joule, 3*(1), 53-80.

[8] Tritt, T. M. (2002). Thermoelectric Materials: Principles, Structure, Properties, and Applications. *Encyclopedia of Materials: Science and Technology*, 1-11.

[9] Alam, H. (2013). A review on the enhancement of figure of merit from bulk to nano-thermoelectric materials. *Nano Energy, 2*, 190–212.

[10] Wang, X., Wang, H., & Liu, B. (2018). Carbon Nanotube-Based Organic Thermoelectric Materials for Energy Harvesting. *Polymers, 10*(11), 1196.

[11] Du, Y., Xu, J., Paul, B., & Eklund, P. (2018). Flexible thermoelectric materials and devices. *Applied Materials Today, 12*, 366-388.

[12] Pu, X., Li, L., Liu, M., Jiang, C., Du, C., Zhao, Z., . . . Wang, Z. L. (2016). Wearable Self-Charging Power Textile Based on Flexible Yarn Supercapacitors and Fabric Nanogenerators. *Advanced Materials, 28*(1), 98-105.

[13] Cutler, M., Leavy, J. F., & Fitzpatrick, R. L. (1964). Electronic Transport in Semimetallic Cerium Sulfide. *Physical Review, 133*(4A), A1143-A1152.

[14] Ballato, A. (1996, 3-6 Nov. 1996). *Piezoelectricity: history and new thrusts.* Paper presented at the 1996 IEEE Ultrasonics Symposium. Proceedings.

[15] Trainer, M. (2003). Kelvin and piezoelectricity. *European Journal of Physics, 24*(5), 535-542.

[16] Mould, R. F. (2007). Pierre curie, 1859-1906. *Current oncology (Toronto, Ont.), 14*(2), 74-82.

[17] Molinié, P., & Boudia, S. (2009). Mastering picocoulombs in the 1890s: The Curies' quartz–electrometer instrumentation, and how it shaped early radioactivity history. *Journal of Electrostatics, 67*(2), 524-530.

[18] Anton, S. R., & Sodano, H. A. (2007). A review of power harvesting using piezoelectric materials (2003–2006). *Smart Materials and Structures, 16*(3), R1-R21.

[19] Hao, J., Li, W., Zhai, J., & Chen, H. (2019). Progress in high-strain perovskite piezoelectric ceramics. *Materials Science and Engineering: R: Reports, 135*, 1-57.

[20] Ramadan, K. S., Sameoto, D., & Evoy, S. (2014). A review of piezoelectric polymers as functional materials for electromechanical transducers. *Smart Materials and Structures, 23*(3), 033001.

[21] Sessler, G. M. (1981). Piezoelectricity in Polyvinylidene Fluoride. *Journal of The Acoustical Society of America - J ACOUST SOC AMER, 70*.

[22] Sorayani Bafqi, M. S., Bagherzadeh, R., & Latifi, M. (2015). Fabrication of composite PVDF-ZnO nanofiber mats by electrospinning for energy scavenging application with enhanced efficiency. *Journal of Polymer Research, 22*(7), 130.

[23] Kim, M., Kaliannagounder, V. K., Unnithan, A. R., Park, C. H., Kim, C. S., & Ramachandra Kurup Sasikala, A. (2020). Development of In-Situ Poled Nanofiber Based Flexible Piezoelectric Nanogenerators for Self-Powered Motion Monitoring. *Applied Sciences, 10*(10).

[24] Giannetti, E. (2001). Semi-crystalline fluorinated polymers. *Polymer International, 50*(1), 10-26.

[25] Salimi, A., & Yousefi, A. A. (2003). Analysis Method: FTIR studies of β-phase crystal formation in stretched PVDF films. *Polymer Testing, 22*(6), 699-704.

[26] Ruan, L., Yao, X., Chang, Y., Zhou, L., Qin, G., & Zhang, X. (2018). Properties and Applications of the β Phase Poly(vinylidene fluoride). *Polymers, 10*(3).

[27] Hu, S., Zeng, S., Li, X., Jiang, J., Yang, W., Chen, Y., . . . Zheng, J. (2020). Flexible and high performance of n-type thermoelectric PVDF composite film induced by nickel nanowires. *Materials & Design, 188*, 108496.

[28] Aghelinejad, M., & Leung, S. N. (2018). Fabrication of open-cell thermoelectric polymer nanocomposites by template-assisted multi-walled carbon nanotubes coating. *Composites Part B: Engineering, 145*, 100-107.

[29] Bharti, M., Singh, A., Samanta, S., & Aswal, D. K. (2018). Conductive polymers for thermoelectric power generation. *Progress in Materials Science, 93*, 270-310.

[30] Inzelt, G. (2011). Rise and rise of conducting polymers. *Journal of Solid State Electrochemistry, 15*(7-8), 1711.

[31] Dughaish, Z. H. (2002). Lead telluride as a thermoelectric material for thermoelectric power generation. *Physica B: Condensed Matter, 322*(1), 205-223.

[32] Bubnova, O. (2013). *Thermoelectric properties of conducting polymers.* (Doctoral thesis, comprehensive summary). Linköping University Electronic Press, Linköping.

[33] Li, Y. (2015). Conducting Polymers. In Y. Li (Ed.), *Organic Optoelectronic Materials* (pp. 23-50). Cham: Springer International Publishing.

[34] Lee, J. J., Yoo, D., Park, C., Choi, H. H., & Kim, J. H. (2016). All organic-based solar cell and thermoelectric generator hybrid device system using highly conductive PEDOT:PSS film as organic thermoelectric generator. *Solar Energy, 134*, 479-483.

[35] Bhavanasi, V., Kumar, V., Parida, K., Wang, J., & Lee, P. S. (2016). Enhanced Piezoelectric Energy Harvesting Performance of Flexible PVDF-TrFE Bilayer Films with Graphene Oxide. *ACS Applied Materials & Interfaces, 8*(1), 521-529.

[36] Sawicka, K. M., & Gouma, P. (2006). Electrospun composite nanofibers for functional applications. *Journal of Nanoparticle Research, 8*(6), 769-781.

[37] Sarkar, K., Gomez, C., Zambrano, S., Ramirez, M., de Hoyos, E., Vasquez, H., & Lozano, K. (2010). Electrospinning to Forcespinning™. *Materials Today, 13*(11), 12-14.

[38] Padron, S., Fuentes, A., Caruntu, D., & Lozano, K. (2013). Experimental study of nanofiber production through forcespinning. *Journal of Applied Physics, 113*(2), 024318.

[39] Je, S.-S., Sharma, T., Lee, Y., Gill, B., & Zhang, J. J. (2011). A thin-film piezoelectric PVDF-TrFE based implantable pressure sensor using lithographic patterning. *2011 IEEE 24th International Conference on Micro Electro Mechanical Systems*, 644-647.

[40] Mao, Y., Zhao, P., McConohy, G., Yang, H., Tong, Y., & Wang, X. (2014). Sponge-Like Piezoelectric Polymer Films for Scalable and Integratable Nanogenerators and Self-Powered Electronic Systems. *Advanced Energy Materials, 4*(7), 1301624.

[41] Wankhade, S. H., Tiwari, S., Gaur, A., & Maiti, P. (2020). PVDF–PZT nanohybrid based nanogenerator for energy harvesting applications. *Energy Reports, 6*, 358-364.

[42] Abolhasani, M. M., Shirvanimoghaddam, K., & Naebe, M. (2017). PVDF/graphene composite nanofibers with enhanced piezoelectric performance for development of robust nanogenerators. *Composites Science and Technology, 138*, 49-56.

[43] Chen, C., Bai, Z., Cao, Y., Dong, M., Jiang, K., Zhou, Y., . . . Xu, W. (2020). Enhanced piezoelectric performance of BiCl3/PVDF nanofibers-based nanogenerators. *Composites Science and Technology, 192*, 108100.

[44] Li, Y., Xu, M.-h., Xia, Y.-s., Wu, J.-m., Sun, X.-k., Wang, S., . . . Xiong, C.-x. (2020). Multilayer assembly of electrospun/electrosprayed PVDF-based nanofibers and beads with enhanced piezoelectricity and high sensitivity. *Chemical Engineering Journal, 388*, 124205.

[45] Hewitt, C. A., Kaiser, A. B., Roth, S., Craps, M., Czerw, R., & Carroll, D. L. (2012). Multilayered Carbon Nanotube/Polymer Composite Based Thermoelectric Fabrics. *Nano Letters, 12*(3), 1307-1310.

[46] Hewitt, C. A., Kaiser, A. B., Roth, S., Craps, M., Czerw, R., & Carroll, D. L. (2011). Varying the concentration of single walled carbon nanotubes in thin film polymer composites, and its effect on thermoelectric power. *Applied Physics Letters, 98*(18), 183110.

[47] Wang, H., Yi, S.-i., Pu, X., & Yu, C. (2015). Simultaneously Improving Electrical Conductivity and Thermopower of Polyaniline Composites by Utilizing Carbon Nanotubes as High Mobility Conduits. *ACS Applied Materials & Interfaces, 7*(18), 9589-9597.

[48] Cho, C., Wallace, K. L., Tzeng, P., Hsu, J.-H., Yu, C., & Grunlan, J. C. (2016). Outstanding Low Temperature Thermoelectric Power Factor from Completely Organic Thin Films Enabled by Multidimensional Conjugated Nanomaterials. *Advanced Energy Materials, 6*(7), 1502168.

[49] Wang, Q., Yao, Q., Chang, J., & Chen, L. (2012). Enhanced thermoelectric properties of CNT/PANI composite nanofibers by highly orienting the arrangement of polymer chains. *Journal of Materials Chemistry, 22*(34), 17612-17618.

[50] Wen, N., Fan, Z., Yang, S., Zhao, Y., Cong, T., Xu, S., . . . Pan, L. (2020). Highly conductive, ultra-flexible and continuously processable PEDOT:PSS fibers with high thermoelectric properties for wearable energy harvesting. *Nano Energy, 78*, 105361.

[51] Kim, J.-Y., Lee, W., Kang, Y. H., Cho, S. Y., & Jang, K.-S. (2018). Wet-spinning and post-treatment of CNT/PEDOT:PSS composites for use in organic fiber-based thermoelectric generators. *Carbon, 133*, 293-299.

[52] Peijs, T. (2017). Electrospun Polymer Nanofibers and Their Composites. 10.1016/B978-0-12-803581-8.10025-6.

[53] Bradbury, S., & Joy, D. C. (2019, October 30). Scanning electron microscope. Retrieved January 12, 2021, from https://www.britannica.com/technology/scanning-electron-microscope

[54] Abdullah, A., & Mohammed, A. (2019). *Scanning Electron Microscopy (SEM): A Review*.

[55] Nanakoudis, A. (2021, January 11). Scanning Electron Microscopy - SEM. Retrieved January 15, 2021, from https://www.thermofisher.com/blog/microscopy/what-is-sem-scanning-electron-microscopy-explained/

[56] Epp, J. (2016). 4 - X-ray diffraction (XRD) techniques for materials characterization. In G. Hübschen, I. Altpeter, R. Tschuncky, & H.-G. Herrmann (Eds.), *Materials Characterization Using Nondestructive Evaluation (NDE) Methods* (pp. 81-124): Woodhead Publishing.

[57] X-ray Powder Diffraction (XRD). (2020, February 14). Retrieved January 15, 2021, from https://serc.carleton.edu/research_education/geochemsheets/techniques/XRD.html

[58] BraggsLaw. (2016, November 10). Retrieved January 15, 2021, from https://serc.carleton.edu/research_education/geochemsheets/BraggsLaw.html

[59] Thermogravimetric Analysis. (n.d.). Retrieved January 18, 2021, from https://www.netzsch-thermal-academy.com/en/advanced-materials-testing/methods/thermogravimetric-analysis/

[60] Höhne, G., Hemminger, W., & Flammersheim, H. J. (1996). *Differential Scanning Calorimetry*.

[61] Principle of Differential Scanning Calorimetry (DSC). (n.d.). Retrieved January 20, 2021, from https://www.hitachi-hightech.com/global/products/science/tech/ana/thermal/descriptions/dsc.html

[62] Abd-Elghany, M., & Klapötke, T. M. (2018). A review on differential scanning calorimetry technique and its importance in the field of energetic materials. *Physical Sciences Reviews, 3*(4), 20170103.

[63] Choudhary, Y. S., Jothi, L., & Nageswaran, G. (2017). Chapter 2 - Electrochemical Characterization. In S. Thomas, R. Thomas, A. K. Zachariah, & R. K. Mishra (Eds.), *Spectroscopic Methods for Nanomaterials Characterization* (pp. 19-54): Elsevier.

[64] Thermoelectric properties of materials. (n.d.). Retrieved March 16, 2021, from http://thermoelectrics.matsci.northwestern.edu/thermoelectrics/index.html

[65] Smits, F., & Schroder, D. (n.d.). Four point probe Resistivity measurements. Retrieved March 16, 2021, from https://www.pveducation.org/pvcdrom/characterisation/four-point-probe-resistivity-measurements

[66] Webster, J. G. (1999). *The Measurement, Instrumentation, and Sensors: Handbook*: CRC Press.

[67] Greppmair, A., Stoib, B., Saxena, N., Gerstberger, C., Müller-Buschbaum, P., Stutzmann, M., & Brandt, M. S. (2017). Measurement of the in-plane thermal conductivity by steady-state infrared thermography. *Review of Scientific Instruments, 88*(4), 044903.

[68] Gómez, J., Estrada, A., Ortega, A., Arredondo, O., Nava, R., Barbosa, R., . . . Lozano, K. (2021). Thermal conductivity of hybrid multilayer graphene-fiber carbon membranes. *Journal of Thermal Analysis and Calorimetry*.

[69] Wan, C., & Bowen, C. R. (2017). Multiscale-structuring of polyvinylidene fluoride for energy harvesting: the impact of molecular-, micro- and macro-structure. *Journal of Materials Chemistry A, 5*(7), 3091-3128.

[70] Full wave rectifier and bridge Rectifier THEORY. (2020, April 14). Retrieved March 18, 2021, from https://www.electronics-tutorials.ws/diode/diode_6.html

[71] Singh, V., Mohan, S., Singh, G., Pandey, P. C., & Prakash, R. (2008). Synthesis and characterization of polyaniline–carboxylated PVC composites: Application in development of ammonia sensor. *Sensors and Actuators B: Chemical, 132*(1), 99-106.

[72] Mohan, S., Nigam, P., Kundu, S., & Prakash, R. (2010). A label-free genosensor for BRCA1 related sequence based on impedance spectroscopy. *The Analyst, 135*, 2887-2893.

[73] Mohan, S., & Prakash, R. (2010). Novel conducting polymer functionalized with metal–cyclam complex and its sensor application: Development of azidothymidine drug sensor. *Talanta, 81*(1), 449-454.

[74] Gupta, B., Joshi, L., & Prakash, R. (2011). Novel Synthesis of Polycarbazole–Gold Nanocomposite. *Macromolecular Chemistry and Physics, 212*(15), 1692-1699.

[75] Akia, M., Cremar, L., Seas, M., Villarreal, J., Valdez, A., Alcoutlabi, M., & Lozano, K. (2018). High-Throughput Production With Improved Functionality and Graphitization of Carbon Fine Fibers Developed from Sodium Chloride-Polyacrylonitrile Precursors. *Polymer Engineering & Science, 58*(11), 2047-2054

[76] Chunyan, W., Xiaoqiu, L., & Xiao, W. (2015, 2015/08). *Synthesis of nitrogen-doped carbon nanofibers and its application for the electrochemical detection of dopamine.* Paper presented at the 2015 International Conference on Advanced Engineering Materials and Technology.

[77] Cervantes, A. d. J. R., Gonzalez, E. R., & Alvarez, J. C. (2018, 26-29 Nov. 2018). *Development and Automation of a Thermoelectric Characterization System.* Paper presented at the 2018 International Conference on Mechatronics, Electronics and Automotive Engineering (ICMEAE).

[78] Trevino, J. E., Mohan, S., Salinas, A. E., Cueva, E., & Lozano, K. (2021). Piezoelectric properties of PVDF-conjugated polymer nanofibers. *Journal of Applied Polymer Science, 138*(28), 50665.

[79] FTIR analysis. (n.d.). Retrieved April 29, 2021, from https://rtilab.com/techniques/ftir-analysis/

[80] Mathias, J. (2020, July 17). How does Ftir work? Retrieved April 29, 2021, from https://www.innovatechlabs.com/newsroom/672/stuff-works-ftir-analysis/

[81] Vazquez, B., Vasquez, H, & Lozano, K. (2012). Preparation Vazquez, B., Vasquez, H., & Lozano, K. (2012). Preparation and characterization of polyvinylidene fluoride nanofibrous membranes by forcespinning™. *Polymer Engineering & Science, 52*(10), 2260-2265.

[82] Lanceros-Méndez, S., Mano, J. F., Costa, A. M., & Schmidt, V. H. (2001). FTIR AND DSC STUDIES OF MECHANICALLY DEFORMED β-PVDF FILMS. *Journal of Macromolecular Science, Part B, 40*(3-4), 517-527.

[83] Cai, X., Lei, T., Sun, D., & Lin, L. (2017). A critical analysis of the α, β and γ phases in poly(vinylidene fluoride) using FTIR. *RSC Advances, 7*(25), 15382-15389.

[84] Audichon, T., Mayousse, E., Morisset, S., Morais, C., Comminges, C., Napporn, T., & Kokoh, K. (2014). Electroactivity of RuO2–IrO2 mixed nanocatalysts toward the oxygen evolution reaction in a water electrolyzer supplied by a solar profile. *International Journal of Hydrogen Energy, 39*, 16785–16796.

[85] Mao, L., Mohan, S., & Mao, Y. (2019). Delafossite CuMnO2 as an Efficient Bifunctional Oxygen and Hydrogen Evolution Reaction Electrocatalyst for Water Splitting. *Journal of The Electrochemical Society, 166*(6), H233-H242.

[86] Mohan, S., & Mao, Y. (2020). Molten Salt Synthesized Submicron Perovskite La1–xSrxCoO3 Particles as Efficient Electrocatalyst for Water Electrolysis. *Frontiers in Materials, 7*(259).

[87] Kakade, M. V., Givens, S., Gardner, K., Lee, K. H., Chase, D. B., & Rabolt, J. F. (2007). Electric field induced orientation of polymer chains in macroscopically aligned electrospun polymer nanofibers. *Journal of the American Chemical Society*, *129*(10), 2777–2782.

[88] Gamry Instruments: Basics of Electrochemical Impedance Spectroscopy Manual

[89] Dias, J. C., Correia, D. M., Botelho, G., Lanceros-Méndez, S., & Sencadas, V. (2014). Electrical properties of intrinsically conductive core–shell polypyrrole/poly(vinylidene fluoride) electrospun fibers. *Synthetic Metals, 197*, 198-203.

[90] Merlini, C., Almeida, R. d. S., D'Ávila, M. A., Schreiner, W. H., & Barra, G. M. d. O. (2014). Development of a novel pressure sensing material based on polypyrrole-coated electrospun poly(vinylidene fluoride) fibers. *Materials Science and Engineering: B, 179*, 52-59.

[91] Merlini, C., Barra, G. M. O., Medeiros Araujo, T., & Pegoretti, A. (2014). Electrically pressure sensitive poly(vinylidene fluoride)/polypyrrole electrospun mats. *RSC Advances, 4*(30), 15749-15758.

APPENDIX A

APPENDIX A

Table A1. State-of-the-art equipment		
Equipment	**Purpose**	**Results Obtained**
Scanning Electron Microscope (SEM)/Energy-Dispersive X-Ray Spectroscopy (EDS)	To observe properties of nanofibers in nanoscale	PVDF nanofibers and PVDF with conducting polymer nanofibers were visualized and were measured diameter size
Cyclone Forcespinning System	To create nanofibers with indicated polymers	Nanofibers were used for piezoelectricity testing and electrical conductivity testing
PVDR	To measure peak-to-peak voltage of nanofibers	Peak-to-peak voltage was obtained and recorded for various nanofibers
Four-Point Probe	To measure resistivity of nanofibers	Resistivity was obtained and recorded, but numbers did not make sense due to the uncertainty of probes touching nanofibers
Electrical Impedance Spectroscopy (EIS)	To characterize the interface between a metal and a conductive solution	The electrical impedance of different nanofibers and different conducting polymers were obtained
X-Ray Diffraction Spectroscopy (XRD)	To provide information regarding the crystallographic structure, chemical composition, and physical properties of nanofibers	PVDF nanofibers and PVDF with conducting polymer nanofibers have been compared to analyze the differences
Thermogravimetric Analysis (TGA)	To provide information of thermal degradation, loss of water, loss of solvent, oxidation, weight %	PVDF nanofibers and PVDF with conducting polymer nanofibers have been compared to analyze the differences
Differential Scanning Calorimetry (DSC)	To provide information of characteristic temperatures, melting, crystallization, thermal stability, heat history, and purity analysis	PVDF nanofibers and PVDF with conducting polymer nanofibers have been compared to analyze the differences

Breadboard	To input a 5V DC into a circuit in series	Resistance was obtained and recorded by the relation of V=IR
Multimeter	To measure the voltage, current, resistance, and temperature of surfaces	Voltage, current, and temperature was obtained, and resistance was obtained and recorded by the relation of V=IR
Fourier-Transform Infrared Spectroscopy (FTIR)	To provide information of the infrared spectrum of absorption or emission of a solid, liquid or gas	PVDF nanofibers and PVDF with conducting polymer nanofibers have been compared to analyze the differences

Table A2. State-of-the-art software

Equipment	**Purpose**	**Results Obtained**
ImageJ	To measure the diameter size of nanofibers	PVDF nanofibers and PVDF with conducting polymer nanofibers images were used to measure diameter size
Gamry Framework	To obtain the electrical impedance of different materials	PVDF nanofibers, PVDF with conducting polymer nanofibers, and conducting polymers were analyzed to obtain the electrical impedance
Microsoft Word	To organize what has been experimented for Thesis/Literature Review	Each individual test result and experimental procedure was noted while also inputting it in my Thesis
Microsoft PowerPoint	To organize what has been experimented/To present what has been done	Each individual test result was shown to my advisors to discuss what is the progress in the experimental process
Microsoft Excel	To mathematically make new solutions/Literature Review	Different solutions were made by modifying concentrations of different components of the solutions while also listing all the articles read to input into my Thesis

EndNote	To properly organize references in Microsoft Word for publication	References were inputted in the end of publication for easy access and organization
OriginPro	Creating figures for plotting purposes for every result	SEM, EIS, XRD, TGA, DSC, FTIR, Thermoelectric Properties

BIOGRAPHICAL SKETCH

Julio Enrique Trevino was born in McAllen, Texas, in December of 1996. All of his life has been spent in La Joya, Texas. He started his studies in Tabasco Elementary. After his elementary, he went to Lorenzo De Zavala Middle School and afterward went to La Joya High School where he achieved his goal of becoming the Valedictorian in May of 2015. While pursuing his high school education, he fell in love with the Mechanical Engineering and pursued a career in it.

In August 2015, he entered the University of Texas Rio Grande Valley in Edinburg, Texas to pursue his bachelor's degree in mechanical engineering. He was a part of numerous organizations such as Tau Beta Pi, TexPrep, and ASME. He was a teacher assistant for various courses such as Materials, Mechanics of Solids, Thermodynamics, and System Dynamics. He also had the opportunity to obtain industry experience by going to a co-op in Emerson in Harlingen, Texas and two internships in Lockheed Martin in Grand Prairie, Texas. He graduated with his bachelor's degree in May of 2019 and decided to pursue his master's degree in mechanical engineering working in nanomaterials in the Partnerships for Research and Education in Materials organization. He started his master's degree in August of 2019 and his project was focused on thermoelectric and piezoelectric composites. After two years of researching on different materials for thermoelectric and piezoelectric applications, he earned his Master of Science in Mechanical Engineering at The University of Texas Rio Grande Valley on May 2021. If you wish to contact me, contact me at my personal email, jtrev1996@gmail.com.